INFORMATION TO USERS

This manuscript has been reproduced from the microfilm master. UMI films the text directly from the original or copy submitted. Thus, some thesis and dissertation copies are in typewriter face, while others may be from any type of computer printer.

The quality of this reproduction is dependent upon the quality of the copy submitted. Broken or indistinct print, colored or poor quality illustrations and photographs, print bleedthrough, substandard margins, and improper alignment can adversely affect reproduction.

In the unlikely event that the author did not send UMI a complete manuscript and there are missing pages, these will be noted. Also, if unauthorized copyright material had to be removed, a note will indicate the deletion.

Oversize materials (e.g., maps, drawings, charts) are reproduced by sectioning the original, beginning at the upper left-hand corner and continuing from left to right in equal sections with small overlaps.

Photographs included in the original manuscript have been reproduced xerographically in this copy. Higher quality 6" x 9" black and white photographic prints are available for any photographs or illustrations appearing in this copy for an additional charge. Contact UMI directly to order.

ProQuest Information and Learning
300 North Zeeb Road, Ann Arbor, MI 48106-1346 USA
800-521-0600

CORRELATION OF THE MICROSTRUCTURE AND PROCESSING CONDITIONS OF ULTRA-THIN OXYGEN IMPLANTED SILICON-ON-INSULATOR MATERIALS

by

Benedict Yorke Johnson

A Dissertation Submitted to the Faculty of the

DEPARTMENT OF MATERIALS SCIENCE AND ENGINEERING

In Partial Fulfillment of the Requirements
For the Degree of

DOCTOR OF PHILOSOPHY

In the Graduate College

THE UNIVERSITY OF ARIZONA

2001

THE UNIVERSITY OF ARIZONA ®
GRADUATE COLLEGE

As members of the Final Examination Committee, we certify that we have read the dissertation prepared by Benedict Johnson

entitled Correlation of the microstructure and processing conditions of ultra-thin oxygen implanted silicon-on-insulator materials

and recommend that it be accepted as fulfilling the dissertation requirement for the Degree of Doctor of Philosophy

Supapan Seraphin	5/10/01
Supapan Seraphin	Date
William G. Davenport	April 27/01
William G. Davenport	Date
Dunbar P. Birnie III	27 APR 01
Dunbar P. Birnie III	Date
Srini Raghavan	4/27/01
Srini Raghavan	Date
J. Brent Hiskey	4/27/01
J. Brent Hiskey	Date

Final approval and acceptance of this dissertation is contingent upon the candidate's submission of the final copy of the dissertation to the Graduate College.

I hereby certify that I have read this dissertation prepared under my direction and recommend that it be accepted as fulfilling the dissertation requirement.

Supapan Seraphin	5/10/01
Dissertation Director	Date

Supapan Seraphin

STATEMENT BY AUTHOR

This dissertation has been submitted in partial fulfillment of requirements for an advanced degree at The University of Arizona and is deposited in the University Library to be made available to borrowers under rules of the Library.

Brief quotations from this dissertation are allowable without special permission, provided that accurate acknowledgment of source is made. Requests for permission for extended quotation from or reproduction of this manuscript in whole or in part may be granted by the head of the major department or the Dean of the Graduate College when in his or her judgment the proposed use of the material is in the interests of scholarship. In all other instances, however, permission must be obtained from the author.

SIGNED: Benedict J. Johnson

AKNOWLEDGEMENTS

I would like to express my thanks to my advisor, Professor Supapan Seraphin for her guidance and encouragement and for allowing me much freedom in this work. She provided me with an opportunity to work on characterization of materials using various electron microscopy techniques. I am also greatly indebted to my supervisory committee members, Professor J. Brent Hiskey, Professor William G. Davenport, Professor Srini Raghavan, and Professor Dunbar P. Birnie, III.

I wish to express my appreciation to Dr. Maria Anc, at Ibis Technology Corporation for providing all the samples used in this study and for the fruitful discussions.

I extend my thanks to all my colleagues at the TEM facility, especially Philip Anderson, for their help in this work. I would like also to thank Gary Chandler for the AES measurements and Professor L. McIntyre, Physics Dept., University of Arizona for the RBS measurements.

Finally, I would like to thank my wife, Doris, for her moral support, patience, care, and absolute faith in me.

This dissertation is dedicated to

my wife, Doris Johnson

and children

TABLE OF CONTENTS

Page

TABLE OF CONTENTS-*Continued*

LIST OF TABLES

LIST OF TABLES-*Continued*

LIST OF FIGURES

LIST OF FIGURES-*Continued*

Figure Page

LIST OF FIGURES-*Continued*

Figure Page

LIST OF FIGURES-*Continued*

LIST OF FIGURES-*Continued*

LIST OF FIGURES-*Continued*

LIST OF FIGURES-*Continued*

Figure Page

ABSTRACT

The Effect of implantation dose and annealing conditions on the microstructure of ultra-thin SIMOX materials formed by 65 keV ion implantation were investigated using transmission electron microscopy (TEM), scanning electron microscopy (SEM), Auger electron spectroscopy (AES), Rutherford backscattering spectrometry (RBS), and optical microscopy. The implantation dose has a strong effect on the microstructure in both the as-implanted and annealed samples. The dominant defects observed in the as-implanted samples were multiply faulted defects (MFDs) near the upper interface and {113} defects beneath the buried oxide (BOX) layer. The BOX layer started to form continuously at the dose of $7.0x10^{17}/cm^2$ after implantation. The most noticeable microstructural feature observed in the as-implanted samples was the mixed structure of silicon and oxygen precipitates which formed around the oxygen projected range. The structure, observed in the samples with dose in the range of 3.5 to $5.0x10^{17}/cm^2$, was found to be the precursor for the formation of silicon islands in the samples after annealing. For the annealed samples, the dose range of $2.0x10^{17}/cm^2$ and $2.5x10^{17}/cm^2$ was established as the optimum for the BOX layer to form continuously without silicon islands. At doses above $2.5x10^{17}/cm^2$, the BOX layer formed continuously with silicon islands. The dose dependence of the defect densities in the top Si layers of the annealed samples was investigated. The dose of $3.5x10^{17}/cm^2$ was found to contain the lowest density of defects in the top Si layer. Above and below this dose, the defect density increased.

The effect of intermediate-temperature annealing on microstructural evolution was investigated. The MFDs and the {113} defects were completely eliminated at 1100°C and

1200°C, respectively. It was found also that the redistribution process for oxygen and silicon interstitials during annealing was initiated at 1100°C, which also recovered the crystallinity of the top Si layer and developed the formation of the BOX layer. Above 900°C, oxygen precipitates in the top Si layer grew in size while they decreased in number with increasing temperature, an indication of Ostwald ripening.

The effect of final annealing temperature and surface capping on the microstructure were also investigated. Annealing at 1300°C for 6 hours restored completely the crystal quality of the top Si layer and produced a continuous and uniform BOX layer. While the surface capping during annealing preserved the thickness of the top Si layer, it adversely affected the BOX layer formation especially at much lower doses. It led also to a slightly higher density of defects in the top Si layer by stabilizing defects which otherwise would have been eliminated during the high-temperature annealing. Additionally, the uncapped samples showed slightly lower density of Si islands in the BOX layer. Oxygen from the annealing ambient diffused in the uncapped samples through the thin top Si layer, which helped the BOX layer grow laterally and lowered the Si island density. The correlations between processing conditions and the microstructure of as-implanted and annealed material were established.

CHAPTER 1

INTRODUCTION

Silicon-on-insulator (SOI) substrates are becoming increasingly important as silicon devices are scaled down into the submicron region. SOI substrates have many advantages over bulk silicon substrates, including low power consumption, radiation tolerance for radiation hardened CMOS (Complementary Metal Oxide Semiconductor) devices, device isolation, process simplicity, and greater packing densities for ultra-large scale integrated (ULSI) circuit applications [1-5]. These advantages result from the dielectric isolation of active devices from the substrates. SIMOX (Separation by IMplanted of OXygen) [6] is presently one of the most mature, competitive and manufacturable means of producing SOI substrates. In this technique, oxygen ions are directly introduced into silicon to form a thin oxide layer underneath a thin top silicon layer. Two other SOI technologies which have reached a level of maturity and are commercially viable are the ELTRAN (Epitaxial Layer TRANsfer) and SMART-CUT [7]. The ELTRAN technology is based on wafer bonding while the SMART-CUT is based both on ion implantation and wafer bonding. The principal advantages of SIMOX over other SOI techniques are the excellent control of the uniformity and thickness of the top Si layer and the buried oxide (BOX) layer [8,9] and reproducibility of the process.

Three major processing steps are required in creating SIMOX substrates as depicted in Figure 1.1: (1) implantation of oxygen, (2) thermal ramping (gradually heating of the wafer), and (3) high-temperature annealing. A relatively high dose of

oxygen ions (from $2.0x10^{17}/cm^2$ to $2.0x10^{18}/cm^2$) are implanted at energies on the order of 50 to 200 keV into a <100> oriented silicon wafer that is kept at a temperature typically between 500°C and 700°C. After implantation, a high-temperature annealing treatment is required to transform the heavily damaged wafer into a device quality substrate. During thermal ramping, the as-implanted wafers are gradually heated up from 800°C to 1300°C ~1350°C for isothermal annealing. In the process, oxygen precipitates in the top Si layer combine into larger precipitates through growth, coarsening and coalescence. Subsequent high-temperature annealing over a period of time (4-6 hours) allows the precipitates to dissolve and incorporate into the BOX layer and most of the defects in the top Si layer are transformed and sometimes eliminated. The result is a uniform BOX layer below a layer of single-crystal silicon. The thickness of the BOX layer depends on the dose of oxygen ions implanted while the thickness of the top Si layer is a function of energy, since it depends on the average penetration depth of the oxygen ions at that energy.

The conventional SIMOX implants oxygen ions at a dose of $1.8x10^{18}/cm^2$ and at energy of 200 keV. This produces a top Si layer and a BOX layer of about 0.2 μm and 0.38 μm, respectively. Due to extensive research and characterization, the conventional SIMOX is well established producing well-defined structures. However, the process is associated with three problems. First, it is relatively expensive because high oxygen doses are used and long implantation time is required to form a continuous BOX layer. Second, the materials still contain a relatively high density of defects in the top Si layer. Third, the conventional material does not allow device designers a choice of layer

thickness especially in the submicron range. These drawbacks undermine the future prospects for SIMOX materials. Therefore, a new approach to SIMOX processing is required to overcoming these drawbacks and making SIMOX the SOI technology of choice for large-scale IC devices with submicron features.

To overcome the above problems several approaches have been developed [10-12] all based on low-dose implantation. So far the approach that promises to address almost all the problems outlined above involves implantation at low dose and low energy. It is the simplest and the least expensive. It also offers a direct way to producing ultra-thin SIMOX materials required for the emerging technology of semiconductor devices with overall dimensions below 0.18 μm for high-speed, low-power and low-voltage applications. Recently it has been demonstrated that by combining both low energy and low dose, ultra-thin SIMOX structures can be formed [13-16]. However, the process brings a new challenge to ion implantation. As the layers are so thin the uniformity and quality of the layers must be better than the conventional SIMOX materials. The presence of defects in these structures could compromise the quality of the materials and as a result undermines the performance and reliability of devices that are built into the ultra-thin structures. The defects include threading dislocations in the top Si layer, discontinuities and silicon islands in the BOX layer. Another concern is the interface roughness which now makes up a greater fraction of the total thickness. The challenge then is how to realize the advantages in the novel configuration without harmful consequences from defect formation. To meet the challenge, it is essential to understand how to achieve the minimum defect density in the structures by changing the various processing parameters.

However, unlike the high-dose SIMOX materials, the development of the microstructure of low-dose low-energy SIMOX materials has received little attention. As a result, there is lack of systematic correlations between microstructural features and processing conditions.

The objectives of this dissertation were to: (i) understand the effects of processing conditions on the microstructure, (ii) determine the density of defects in the top Si layer and BOX layer as a function of implantation dose, and (iii) understand the formation mechanisms of defects in low-dose low-energy SIMOX materials. To realize these objectives, the development of the microstructure from the implantation step through to the final annealing step was examined and the effects of various processing conditions on defects in both the top Si and the BOX layers were determined. The results will provide guidance for optimizing the processing conditions for the realization of the advantages of the novel approach without encountering the drawbacks.

In Chapter 2 of this dissertation, literature relevant to the study is reviewed. Chapter 3 covers experimental methods and characterization techniques used in the study. Chapter 4 presents the effects of variations in implantation dose on the microstructure of ultra-thin SIMOX materials. Chapter 5 reports on the effect of intermediate-temperature annealing on the evolution of the microstructure in ultra-thin SIMOX materials. Chapter 6 reports on the effect of high-temperature annealing parameters, including temperature and surface capping. In chapter 7, correlations between microstructural features and processing parameters are established. In Chapter 8, the work is summarized and concluded.

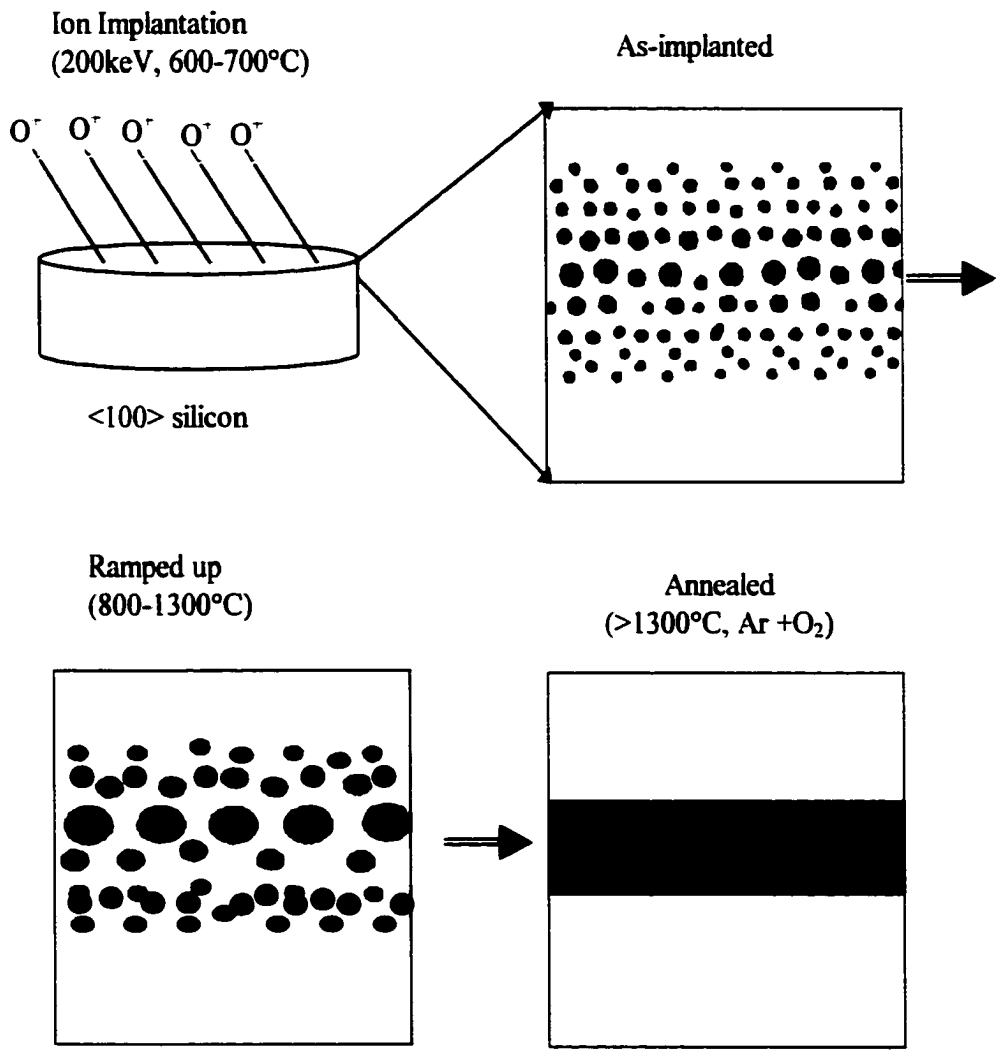

Figure 1.1 Schematic diagram illustrating typical SIMOX fabrication process

CHAPTER 2

BACKGROUND

2.1 Historical Overview

The idea of forming oxides by oxygen implantation into silicon was first proposed by Smith in 1956 [17]. But it was only in 1966 that Watanabe and Tooi [18] produced the first silicon dioxide by oxygen ion implantation into silicon. Unfortunately, their work was not immediately followed by additional studies because of the concern that the quality of oxide produced by implantation was not as good as that of thermal oxide. It was not until 1977 when Badawi and Anand [19] reported that the quality of buried oxide formed by implantation could be improved by using a post-implantation annealing treatment. In 1978, Izumi et al. [6] reported the successful fabrication of a complementary metal-oxide-semiconductor (CMOS) ring oscillator using buried oxide formed by oxygen ion ($^{16}O^{+}$) implantation into silicon. They named the new SOI technology "SIMOX" which stands for separation by implanted oxygen. From 1978 to 1985, many studies were performed in order to understand the formation mechanisms of SIMOX structures.

The turning point in the history of SIMOX development occurred in 1985 with the introduction of an industrial high current (100 mA) oxygen implanter [20] and high-temperature annealing [21]. The high-current density implanter (NV-200) significantly reduced the processing time and led to the commercial production of SIMOX wafers. The high-temperature annealing led to a drastic improvement in the quality of SIMOX materials. One remaining problem for commercial production of SIMOX wafers was how

to minimize defect density in the top Si layer. In the following years, many studies were devoted to finding the optimum processing conditions and methods for reducing the defect density in the material. Through these studies, particularly those conducted by Visitserngtrakul et al. [22-25], the dislocation density in the top Si layer, for example, dropped from $10^{10}/cm^2$ to$10^5/cm^2$. In 1995, Ibis Technology Corporation succeeded in building an ion implanter (Ibis1000) which independently controls beam current and wafer temperature [26]. This allows for implanting oxygen ions at low energies and doses, while maintaining the temperature of the wafer above 500°C.

2.2 Effects of Processing Parameters on the Microstructure of SIMOX

The final microstructure of a SIMOX material is strongly dependent on the sum of all the processing steps used to produce the material. The principal processing parameters are: the implantation dose, implantation energy, wafer temperature, annealing temperature, annealing time, and ambient conditions.

The implantation dose principally controls the thickness of the BOX layer. Increasing the dose thickens the oxide layer while the top Si layer gets thinner. In order to form a continuous BOX layer the concentration of oxygen must reach the stoichiometric level of $4.2x10^{22}/cm^3$ to form SiO_2. A critical oxygen dose exists for each implantation energy to form a continuous BOX layer. A calculation based on a Monte-Carlo simulation showed that a critical dose for forming a continuous BOX layer in as-implanted material is $1.4x10^{18}/cm^2$ at 200 keV [27]. If effects of annealing are considered, the critical dose becomes lower. After a continuous stoichiometric oxide is

formed, any incremental dose causes oxygen deposited in the BOX layer to preferentially diffuse to the top Si/BOX interface and thus, growth occurs predominantly towards the wafer surface [28]. Post-implantation annealing causes the BOX layer to grow further towards the wafer surface as oxygen precipitates in the top Si layer dissolve and the oxygen diffuses to the Si/BOX interface.

The implantation energy defines the thickness of the top Si layer since it affects the average depth of penetration defined as projected range (R_p) and the spread of implanted oxygen ions referred to as straggling of projected range (ΔR_p). Implantation at higher energy results in a longer projected range from the surface and a larger straggling. A higher dose is required to form a BOX layer at higher implantation energy. The BOX layer forms deeper in the wafer leaving a thicker Si layer on the top. Lower energies allow lower doses to be implanted hence, the implantation time is greatly reduced. Consequently, the implantation damage is minimized since the number of ions generating point defects is decreased.

The wafer temperature during implantation affects the crystallinity of the top Si layer and the type of defects formed. During implantation, large amounts of silicon atoms are displaced from their lattice sites due to atomic collision. This can cause the top Si layer to become amorphous unless the wafer temperature is sufficiently high to ensure dynamic annealing. Early SIMOX materials, prior to 1985, were made in low or medium current implanters operating at 150 to 200 keV, which resulted in low implantation temperatures of 350°C to 450°C. For the materials implanted in this temperature range, the implantation damage can cause silicon to become amorphous, which upon annealing

is transformed into polycrystalline material [29]. This problem was solved with the introduction of high-current (100 mA) implanters in 1985, which could raise the wafer temperature above 500°C through beam heating induced by the high-current density. Above 500°C, some damage can be annealed out and the crystallinity can be maintained through the mechanism known as solid phase epitaxy [30].

High-temperature annealing is required to transform the as-implanted material into a device quality substrate. Early SIMOX processing was limited to 1150-1200°C for two or three hours because of the limitation of the conventional furnace. Although at these annealing conditions the quality of the top Si layer improved significantly, the materials still contained a high density of oxygen precipitates and dislocations in the top Si layer. In 1985, Jaussaud et al. [31] employed annealing at 1300°C for 6 hours to achieve complete precipitate dissolution with the formation of abrupt Si/BOX interfaces. Annealing was carried out in a suitable annealing chamber filled by an atmosphere formed of argon or nitrogen gas. The effect of annealing ambient (nitrogen vs. argon) was systematically studied by Visitserngtrakul et al. [25]. The results indicated that there is a higher precipitate density in the top Si layers of samples annealed in nitrogen than in argon for identical temperature and time conditions. They attributed the effect of nitrogen to the resulting oxynitride complex which helped the stability of the precipitates and thus made them more difficult to dissolve. A small percentage of oxygen is usually added to the argon atmosphere to give a sufficient oxygen partial pressure to prevent formation of silicon monoxide (SiO) lumps and subsequent pits on the surface [32]. It is customary to cap the sample surface to prevent the formation of external oxide which consumes the

silicon surface. This is important especially for the ultra-thin SIMOX to preserve the thickness of the top Si layer. White et al. [32] reported that there is no significant difference between the microstructures of the capped and uncapped low-dose high-energy SIMOX samples. On the contrary, experiments performed in this dissertation using ultra-thin SIMOX samples show that surface capping affects the formation of the BOX layer and defect density in the top Si layer [16,33]. A qualitative mechanism is presented in this dissertation to explain the effects of surface capping on the microstructure of ultra-thin SIMOX materials.

2.3 Categories of SIMOX

SIMOX processing techniques can conveniently be placed in three categories as illustrated in Figure 2.1: (i) high-dose high-energy SIMOX, (ii) low-dose high-energy SIMOX, and (iii) low-dose low-energy SIMOX. The high-dose high-energy SIMOX typically implants oxygen ions at a dose of $1.8 \times 10^{18}/cm^2$ at an energy range of 150-200 keV. At present, the materials produced by this technique are the most widely used. There are two options available under the high-dose SIMOX process: (i) single-step implantation and (ii) the multiple-step implantation. In the single-step implantation, the total dose of $1.8 \times 10^{18}/cm^2$ is implanted followed by a one step high-temperature annealing. In the multiple-step implantation, two lower-dose implants ($0.9 \times 10^{18}/cm^2$) or three lower-dose implants ($0.6 \times 10^{18}/cm^2$) are performed with high-temperature annealing after each implantation step. The multiple-step implantation technique was adopted to reduce the high density of defects associated with the single-step implantation. High-dose

SIMOX materials are used for radiation-hard integrated circuits especially in the niche-market applications where their radiation-hardness benefit far outweighs their high cost [34].

The low-dose high-energy SIMOX implants oxygen ions at doses less than $1.0x10^{18}/cm^2$ but in the same energy range (150-200 keV) used in the high-dose process. The thickness of the top Si layer is comparable with that of the high-dose SIMOX but the BOX layer is much thinner (20-50%). The interest in low-dose high-energy SIMOX emerged to reduce the cost of producing SIMOX materials due to the shorter implantation time. However, it became clear that the integrity of the BOX layer is much inferior to that of the high-dose SIMOX. To improve the integrity of the BOX layer, two modifications were developed for the low-dose SIMOX process. The first modification involves a second high-temperature annealing in a highly oxidizing ambient following the conventional high-temperature annealing. This modification was first reported by Nakashima et al. [35], who suggested that oxygen penetration through the top Si layer during the second annealing step causes internal oxidation of the BOX layer formed after the first annealing treatment. The second modification reported by Holland et al. [11] is a two-step implantation process. The process includes a conventional implantation followed by a "touch" implantation at or close to room temperature to selectively amorphisize the region near the projected range, R_p (where the BOX forms during subsequent annealing). This was done to recrystallize the region during annealing into polycrystalline. Rapid diffusion of oxygen along grain boundaries within the layer was thought to promote the formation of a continuous oxide during annealing.

The low-dose low-energy technique produces SIMOX wafers at much lower implantation doses and much lower implantation energies (50-120 keV), and therefore makes SIMOX material much more economical to produce. Materials produced by this technique contain ultra-thin layers. The early concern for implanting ions at low dose low energy was that the wafer self-heating could not generate sufficiently high thermal energy to ensure dynamic annealing of damage in silicon during implantation. For high-dose implantation, the wafer temperature is readily raised above 500°C, a level necessary for dynamic annealing to occur [36]. The development of an ion implanter (Ibis 1000) in 1995 by Ibis Technology Corporation solved the self-heating problem and allowed for implanting oxygen ions at low energies and doses. The drive for the low-dose low-energy SIMOX process is two fold: First, the production cost of SIMOX wafer is proportional to both the implantation energy and dose. Secondly, direct fabrication of thin top Si layers is attractive for thin-film device applications. Figure 2.2 illustrates an application advantage of ultra-thin SIMOX structure in the design of metal-oxide semiconductor field effect transistors (MOSFETs), the basic building blocks of the vast majority of integrated circuits [37]. If the transistor is built into a relatively thick top Si layer (0.3μm) only a third of the layer is depleted and the rest is neutral. On the other hand, if the device is made in a thinner Si layer, the whole top Si layer is completely depleted. Devices that are built into fully depleted SOI layers tend to run faster, operate at lower voltages and consume less power. Though the low-dose low-energy SIMOX processing technique offers enormous economic as well as application advantages, the quality of both the top Si and BOX layers becomes more critical. Therefore, the technological challenge for the

low-dose low-energy implantation process is to tailor the SIMOX layers as thin as possible while maintaining defects in the layers at acceptable levels. This work has performed systematic investigation of ultra-thin SIMOX materials with the purpose of finding the optimum conditions for producing high-quality ultra-thin top Si and BOX layers.

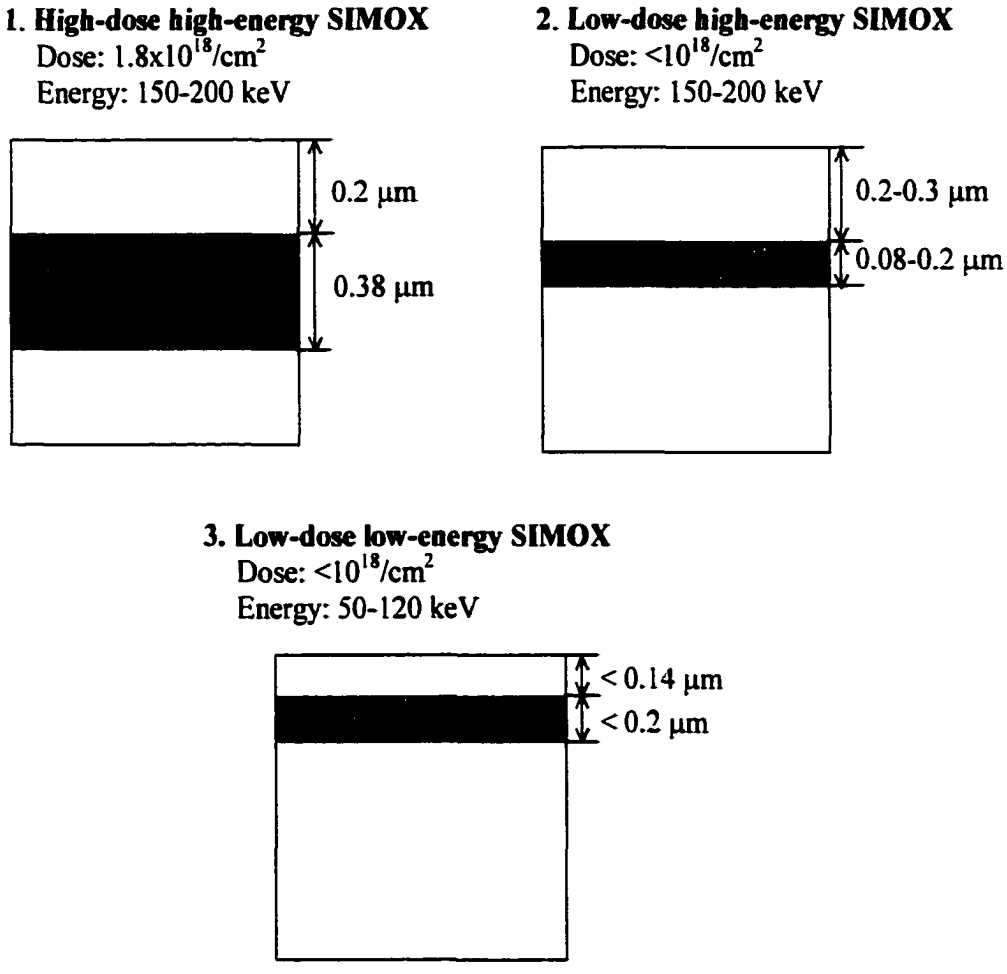

Figure 2.1 SIMOX processing techniques

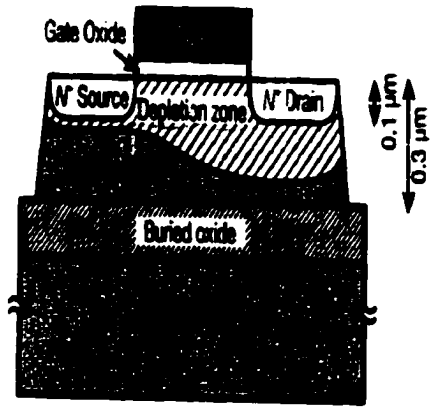

(a) Partially depleted transistor on conventional SIMOX

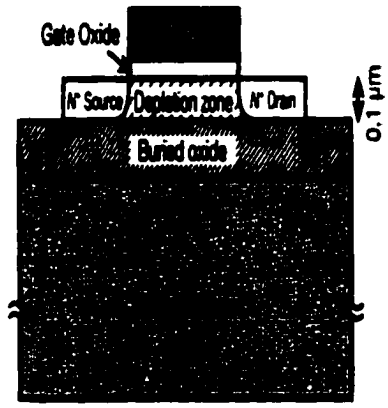

(b) Fully depleted transistor on ultra-thin SIMOX

Figure 2.2 A cross-sectional view of n-channel silicon MOSFET.

(a) Partially depleted and (b) Fully depleted SOI MOSFET [37].

2.4 Formation of the Buried Oxide Layer

The BOX layer in SIMOX is formed through SiO_2 precipitation processes which occur during ion implantation and subsequent annealing. The processes involved in the formation of SiO_2 precipitates by ion beam synthesis are very complex. Under the non-equilibrium conditions of ion implantation, the precipitation mechanism may be complicated by defects produced and the large variety of complexes formed by the implanted species. However, physically, five overlapping stages can be distinguished [38]: (i) supersaturation of oxygen, (ii) nucleation of precipitates, (iii) growth of precipitates, (iv) ripening of precipitates, and (v) coalescence of precipitates. During implantation, supersaturation of oxygen occurs when the concentration of oxygen is close to the solubility limit of oxygen in silicon ($2.0x10^{18}/cm^3$) at 1405°C, the melting point of silicon [39]. When the concentration exceeds this critical value, the system becomes thermodynamically unstable and the supersaturated oxygen nucleates in the form of stable SiO_2 precipitates. As the implantation proceeds, the precipitates grow at the expense of additional oxygen introduced into the implanted region. In the high-dose process, the growth process continues until a continuous oxide layer is formed around the projected range (R_p). Since the oxygen concentration in the wings of the oxygen profile is still high and above the solubility limit, precipitates are formed there. There is a gradient in the precipitate size with largest being adjacent to the BOX layer [40-42]. After the BOX layer is formed, oxygen in the top Si layer is present in two forms, in solution and in precipitates.

During high-temperature annealing, oxygen precipitates grow by consuming oxygen from either coming out of solution or from smaller precipitates which dissolve because the surface free energy is higher than the free energy of formation [43]. The precipitation mechanism by which larger precipitates grow at the expense of smaller ones is known as Ostwald ripening and is explained in terms of Gibbs-Thomson effect which is the free energy, ΔG, increase due to interfacial curvature:

$$\Delta G = 2\gamma V_m / r \qquad 2.1$$

where γ is interfacial energy, V_m is molar volume, and r is the radius of a spherical precipitate. Due to this effect, oxygen concentration in silicon adjacent to a precipitate will increase as the radius of curvature decreases. Therefore, there will be concentration gradients in the silicon matrix, which will cause oxygen atoms to diffuse in the direction of the largest precipitates away from the smallest, so that small precipitates shrink and disappear while large precipitates grow. The overall result is that the total number of precipitates decreases and the mean radius increases with time. Finally, the precipitates become so large that they may overlap and coalesce towards the BOX layer. The precipitation process ceases when all the oxygen in the wings of the implanted oxygen-depth profile has segregated to the BOX layer, which may be considered as a precipitate of infinite radius in the direction of the surface normal.

When the implantation dose is lowered, no continuous BOX layer is formed after implantation (substoichiometric doses). The implanted structure consists of isolated oxygen precipitates of various sizes, the largest occurring in the vicinity of the oxygen projected range (R_p). The coarsening and coalescence of these precipitates to a single

BOX layer during annealing is rather critical. After annealing of such substoichiometric materials, pattern formation like "humps" and "spikes" in the concentration profile and double or multiple bands of oxygen precipitates observed in TEM are often reported [44,45]. Therefore, for such materials a better understanding of the precipitation mechanisms becomes very important. It is critical to choose annealing conditions that will result in effective segregation of precipitates at the projected range where the precipitates are largest, and where they can act as sink for the implanted oxygen into a single continuous BOX layer. In this study we have evaluated the effects of annealing parameters on precipitate formation in ultra-thin SIMOX materials. Through a careful choice of annealing parameters, the precipitation behavior (growth or ripening) of the oxygen precipitates can be controlled to form a continuous BOX layer from substoichiometric doses.

The formation and growth of the BOX layer during implantation and annealing play a key role in the formation of crystallographic defects in the top Si layer. As mentioned above the BOX layer is formed through SiO_2 precipitation processes. The conversion of Si to SiO_2 involves an increase in molar volume and the generation of self-interstitials, Si_I, according to the reaction:

$$xSi + O_2 \rightarrow SiO_2 + (x - 1)\, Si_I \qquad 2.2$$

Ideally, a strain-free SiO_2 formation requires that $x = 2.2$ which implies an excess of Si interstitials in the silicon matrix. It has been reported that Si_I has high formation energy but very low migration energies and the sum of these two activation energies is about 5 eV [46,47]. Therefore, the self-interstitials created by irradiation can migrate

easily even at low temperatures [48]. These excess silicon interstitials tend to migrate towards the surface, which is the natural sink for them. Jaussaud et al [49] have identified the conditions under which the process can occur, namely: (i) the silicon interstitials must have easy paths to migrate to the free surface and (ii) incorporation of silicon atoms at the surface must be easy and effective. These can be difficult to achieve since the formation and growth of SiO_2 precipitates during implantation tends to inhibit the diffusion of the interstitials because of the extremely low diffusivity of silicon in SiO_2 ($10^{-20}cm^2/s$) [50,51]. This results in supersaturation of silicon interstitials which in turn leads to a build up of stress inside the BOX layer. The increase of stress results in the formation of multiply stacking faults (MFDs) in the top Si layer near the Si/BOX interface [22,52]. Many of these stacking faults are eliminated during high-temperature annealing. However, a fraction of them are transformed into dislocations through unfaulting reactions at high temperatures [53]. More information on MFDs is given in the next section.

2.5 Defects in the Top Si Layer in High-Dose SIMOX

Developments of the last 10-12 years have achieved significant control of defects in high-dose SIMOX materials. Two categories of defects have been identified in the as-implanted high-dose SIMOX. Defects of the first category are created at the uppermost part of the top Si layer due to migration of Si interstitials to the surface [50,54-57]. Conditions determining the defect density include the quality of the wafer surface, implantation temperature, flux of Si interstitials towards the surface, and crystallographic

orientation of the surface. The defects are mainly small dislocation loops of the extrinsic type, dislocation half loops (DHLs), and segments of dislocations. Several mechanisms have been proposed for the formation of DHLs but none of them can fully account for the experimentally observed stress dependence of DHL density. The density has been correlated to the state of the near surface stress in the as-implanted SIMOX, which is a function of both the implantation temperature and dose. So far, the stress-assisted climb mechanism comes closest to explaining stress dependence of DHL [58]. Recent work on dislocation evolution suggests that the density of DHLs in high-dose SIMOX increases exponentially with increasing implantation dose [59]. Most of the DHLs escape to the surface during the high-temperature annealing. However, some of them act as precursors to form pairs of threading dislocations, as will be discussed later.

Defects of the second category are created at the bottom of the top Si layer near the Si/BOX interface due to radiation damage (generating both Si interstitials and vacancies) and strain created due to oxide formation [54]. This is the most defective zone because the implantation damage has its maximum there. The defects are small dislocations of about 40 nm in length and are formed during the early stages of implantation. In addition to radiation-damage defects, there are defects created due to stress developed by the inability of volume accommodation of the BOX [52], and these are MFDs. The structure of the MFDs was reported by Visitserngtrakul et al. [52], who found that they consist of overlapping extrinsic and intrinsic stacking faults randomly spaced between two and eight atomic layers apart. MFDs are usually associated with SiO_2 precipitates and are clearly created by silicon lattice deformation at the upper interface. Most defects in this

zone are eliminated during annealing, pinned by the growing SiO_2 precipitates, or are annihilated at the upper interface.

Many of the defects found in the as-implanted state are eliminated during the high-temperature annealing. The major defects that remain in the top Si layer after high-temperature annealing are threading dislocations (TDs), which thread from the wafer surface to the BOX. TDs are found to occur in pairs and at density of 10^4-10^6/cm^2 for high-dose SIMOX. TDs originate presumably from DHLs that form during the implantation process. During annealing the DHLs expand downward and intersect the BOX layer creating pairs of dislocations. Stacking faults tetrahedra (SFTs), and stacking fault pyramids (SFPs) can also be introduced during dissolution of the oxygen precipitates in the Si layers [60]. It is found that the formation of SFPs is closely related to the evolution of MFDs in as-implanted sample [61].

2.6 Defects in the Top Si Layer in Low-Dose SIMOX

Low-dose implantation is one of the methods expected to reduce defect density in SIMOX. This is found to be true down to a certain dose limit. Recently, it was found that for a set of samples implanted at 180 keV, an increasingly high density of defects formed below a threshold dose of $0.4\text{x}10^{18}$/cm^2 [44]. These results showed that up to 10^8/cm^2 TDs formed at doses down to $0.2 \text{ x } 10^{18}$ cm^2, while less than 10^5cm^{-2} TDs formed in the doses lying between $0.4\text{x}10^{18}$/cm^2 and $1.5\text{x}10^{18}$/cm^2. The defect formation in low-dose SIMOX has become a subject of discussion in several studies. The formation mechanism of TDs in low-dose SIMOX is found to be different from that in high-dose SIMOX. It has

been reported [62] that the TDs originate from long (3-10μm) extrinsic stacking faults which are unfaulted when annealed above 1200°C. The stacking faults were reported to form at an intermediate annealing temperature of 1100°C and then disappear above 1200°C leaving behind TD pairs. Since there is no reported data on DHLs in as-implanted low-dose SIMOX, the TDs in low-dose SIMOX evidently do not originate from DHLs as proposed for the high-dose SIMOX.

Defects in the top Si layers of low-dose low-energy SIMOX materials have not been extensively studied due to the difficulty in characterizing them. Dilute chemical etchants that are normally used to analyze low-defect density SIMOX materials are not reliable when the top Si layer is thinner than about 100 nm [63]. Consequently, the formation mechanisms for defects in the top Si layer of ultra-thin SIMOX materials are not well understood. The challenge to the defect characterization was addressed in this study. Using a more reliable etching solution, we successfully characterized defects in the top Si layers of low-dose low-energy SIMOX. The results are presented in Chapter 4.

CHAPTER 3

EXPERIMENTAL PROCEDURE

3.1 SIMOX Sample Acquisition and Processing Conditions

This work has been carried out in collaboration with Ibis Technology Corporation based in Danvers, Massachusetts. Ibis is the world leading SIMOX supplier, and provided all the samples used in this study. The samples were (100) p-type silicon wafers implanted with $^{16}O^{+}$ at a current density of 40 mA/cm^2 with Ibis 1000 implanter. This high-current implanter is the second generation of Ibis own design shown in Figure 3.1 [26]. It has been used in the fabrication of SIMOX wafers since June 1995. High-quality 150 and 200 mm SIMOX wafers are being produced with uniformity and reproducibility. The system includes an ion source, analyzer, beam scan system, and vacuum loadlock robotics wafer handler. Wafer temperature during implantation is maintained through a servo-controlled heat lamp array. The beam is scanned at a rate of 150 Hz across a circular array of wafers held by pedestals in a hub and spoke arrangement rotating at 105 rpm. The ion beam is only allowed to impinge on silicon in the regions upstream and downstream of the implant plane to prevent metallic contamination and particulate generation. The wafer holders individually rotate to set implantation angle and to facilitate horizontal movement. The beam generation and transport system shown schematically on the left side of the figure consists of an ion source, mass analyzer, accelerator column, scanner magnet, neutral filter magnet, and a collimator. The system is capable of delivering up to 70 mA of $^{16}O^{+}$ at 210 keV while maintaining a parallel beam scan across 200 mm wafers. After implantation, high-temperature annealing was

performed to restore the crystallinity of the top Si layer, and to obtain a high-quality BOX layer. The final annealing temperatures were 1300°C to 1350°C. The annealing matrix in this study was designed to examine the effect of annealing temperature. The intermediate-temperature annealing of 900°C to 1200°C (for 2 hours at each temperature) was carried out to study the evolution of defects and oxygen precipitates, and crystal recovery process. A surface capping experiment was also performed to study the effect of surface capping during annealing on the microstructure. In this experiment two sets of samples were implanted at 65 keV with the same dose range. After implantation, one set was annealed for 4 hours at 1350°C in Ar + 0.5% O_2 without a protective cap on the sample surface. The second set was annealed for 6 hours at 1350°C in Ar + 5% O_2 covered with a protective cap on the sample surface. The protective cap was formed by decomposition of TetraEthyl OrthoSilicate (TEOS) to prevent the top Si layer from being oxidized. The 5% O_2 used in the capping ambient was the minimum required to prevent decomposition of the TEOS material during annealing. The specific implantation and annealing parameters used for preparation of samples used in this study are listed in Table 3.1. All samples were implanted at 65 keV. The wafer temperature during implantation was maintained at 500°C and the ramp rate was 10°C/min.

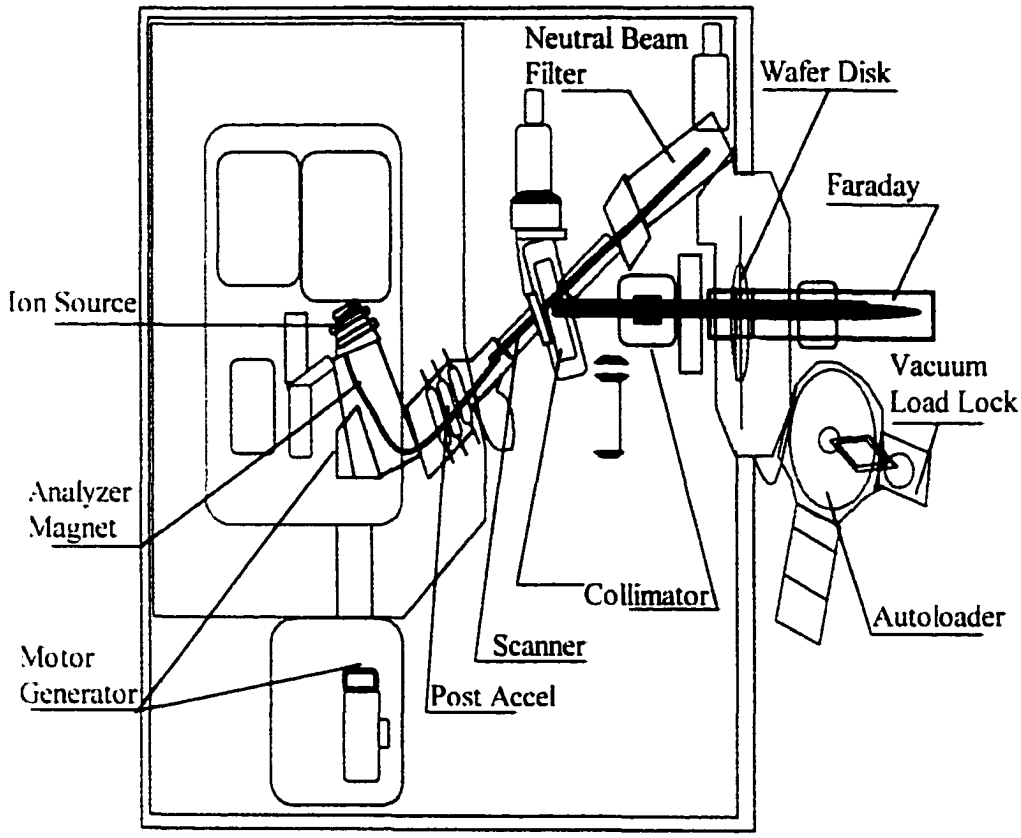

Figure 3.1 Schematic illustration of Ibis 1000 implanter [26].

Table 3.1 Specific processing conditions used in this study. All samples were implanted at 65 keV with wafer temperature of 500°C. The ramp rate at the annealing step was kept constant at 10°C/min for all experiments.

Investigated Effect	Implantation Dose $x10^{17}/cm^2$	Annealing		
		Temperature °C	Time hr	Ambient
I. Dose	1.5 2.0 2.5 3.0 3.5 4.0 5.0 7.0	1350	4	Ar+1%O_2
II. Structural evolution	4.5	900 1100 1200	2	Ar+ 1%O_2
III. Annealing temperature	4.5	1300 1350	6	Ar+ 1%O_2
IV. Surface capping	1.5 2.0 2.5 3.0 3.5 4.0 5.0 7.0	without capping layer		
		1350	4	Ar+ 0.5%O_2
		with capping layer		
		1350	6	Ar+ 5%O_2

3.2 Characterization of Samples

Structural and chemical characterization of SIMOX samples prepared under different processing conditions was performed using TEM, SEM, AES, RBS, and Optical microscopy. TEM provided information on layer thickness, types of defects and their locations in the top Si layer, distribution of silicon islands in the BOX layer, interface roughness, and the morphology of the BOX layer (continuous or discontinuous). SEM was used to evaluate quantitatively the area density of silicon islands in the BOX layer. AES analysis was performed to acquire oxygen depth profiles in the intermediate annealed samples. RBS was used to determine the damage depth profiles in the as-implanted and annealed samples. Optical microscopy was used to determine the density of defects in the top Si layers of the annealed samples. Each characterization technique used in this study is described in the following sections.

3.2.1 Transmission Electron Microscopy

Two modes of TEM operations were used: (1) conventional bright field imaging to view overall morphology, layer thickness, defects, silicon islands, and interfaces. (2) high-resolution imaging to examine the quality of the interfaces (smooth or rough), to accurately measure the thickness of the top Si and the BOX layers and the size of oxygen precipitates. Samples were examined with a Hitachi H-8100 microscope at 200 keV. This microscope has a double-tilting stage of $\pm$ 30°, which is suitable for diffraction contrast imaging including bright and dark field imaging. In analyses of defects, two-beam conditions were set up for recording the images. At this condition, only two beams are

strongly excited, i.e. one transmitted beam (0 beam) and one diffracted beam (g beam). In bright field imaging, a small objective aperture is inserted into the back focal plane to allow only the transmitted beam to form the image. In dark field imaging, beams are tilted in such a way that the transmitted beam is moved to where the diffracted +g beam is located, and the -g beam is moved to the optic axis. The objective aperture is then inserted at the optic axis to allow the -g beam to form the image. This technique is called centered dark field (CDF) imaging. It gives better information about dislocation geometry and dissociation than a bright field mode. In high-resolution TEM (HRTEM) imaging the specimen is tilted so that the <110> zone axis is coincident with the electron beam, and a large aperture is inserted in order to allow many beams to pass and recombine on the image plane. Due to the limits of resolution of the microscopes (0.27 nm), only two sets of {111} planes could be resolved when viewing along a <110> beam direction. Each dot in the HRTEM image of a silicon specimen corresponds to a column of pairs of silicon atoms with a spacing of 0.14 nm.

TEM Sample Preparation

Sample preparation is a critical step for effective TEM analysis. A sample must be made thin enough to be transparent to an electron beam, typically 1000 times thinner than a human hair. The process is time-consuming and requires a great deal of skill and patience. The section below describes in detail procedures of sample preparation methods for cross-sectional view and plan view.

I. Cross-section TEM Sample Preparation

Cross-section samples were prepared based on the method of Ma and Chevacharoenkul [64] as shown in Figure 3.2. The wafer is cleaved along <110> into a piece about 10 mm wide and 10 mm long with a diamond pen. It is then cut with a diamond saw into four slices about 2 mm wide. The individual slices are cleaned and washed in acetone and distilled water, and then glued together with "M-Bond 610 adhesive", to form a stack about 3 mm in height. The two silicon pieces in the middle of this stack are placed side-of-interest to side-of-interest to increase the probability of preparing a usable sample. The outer two slices can be blank silicon if there is a limited supply of samples. The stack is pressed in a metal vice and heated at 100°C for at least one hour to thermo-set the adhesive glue. The laminated stack is then mounted on a saw and thin slices, 0.4-1 mm thick, are cut from one end. The sample is adhered to a dimpler sample platen with "crystal-bond". A plan-of-polish is produced on the exposed face using dimpler-set for flattening and polishing the sample. The sample is inverted and thinned to about 100 μm. Then, a dimpling tool is used to dimple into the center of the stack. Dimpling is a process whereby a rotating wheel, covered with decreasing grit-size slurry, is advanced into the rotating sample. The rotating wheel needs to be adjusted carefully so that it is positioned over the center of the sample. A hemispherical polish front will advance into the sample and create the thinnest portion at the center of the specimen. An end-point detecting device is set to stop the polishing operation when the thinnest portion is about 30 to 50 μm thick. The sample is removed from the dimpling platen, cleaned, and then glued to a single-hole microscope grid. Final thinning is

performed on the sample with Ar^+ ions in an ion mill until an electron-transparent region is obtained at the center of the sample. For cross-sectional samples two ion guns are operated to thin both sides of the sample. The ion-milling process can take 1 to 5 hours depending on the thickness of the sample at the beginning of the milling process.

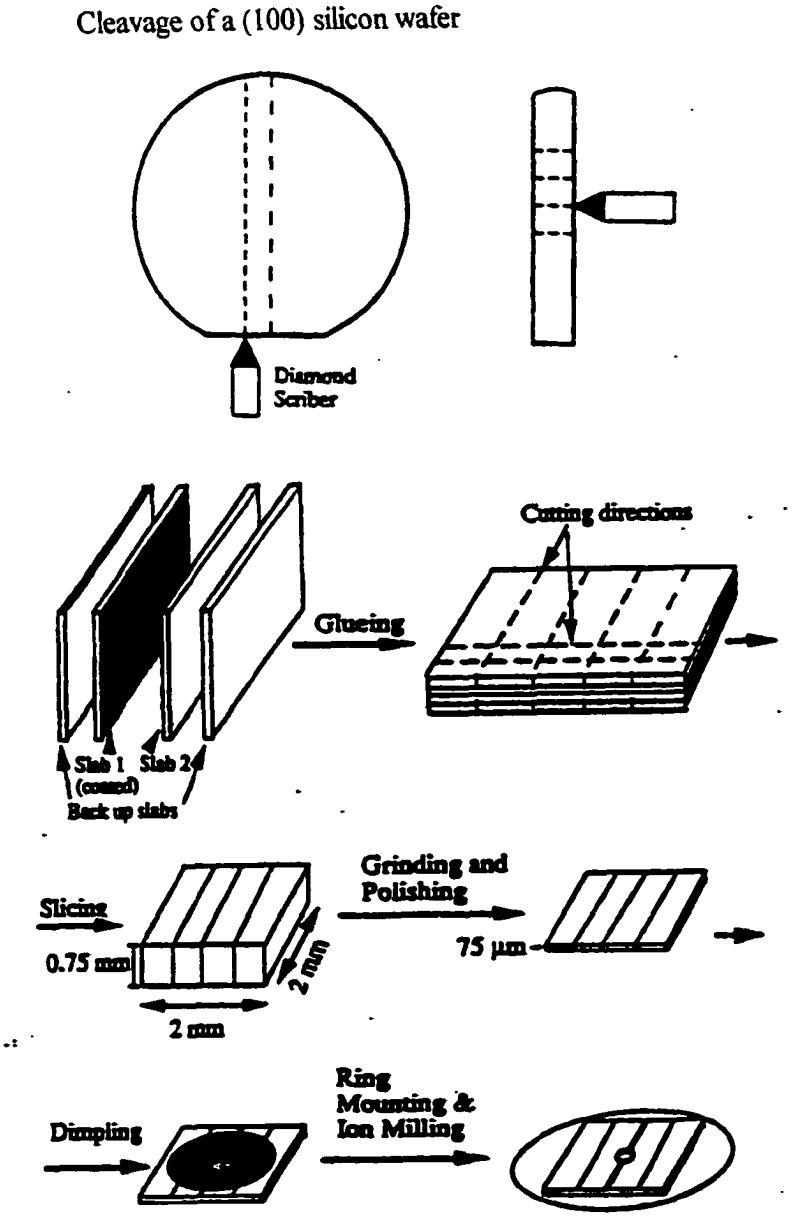

Figure 3.2 Schematic illustration of cross-sectional TEM sample preparation steps [64]

II. Plan-view TEM Sample Preparation

Conventionally, plan-view samples of high-dose SIMOX are prepared by hydrofluoric acid (HF) floating-off due the thickness of the top Si layer being in the range of 150 to 300 nm which falls conveniently within the range of electron transparency. They are prepared by putting samples of dimensions of 2 mm x 2 mm in 50% HF solution which dissolves the BOX layer after a few hours. The top Si layer is floated off as a thin film and placed on 200 mesh copper grid for TEM observation. For samples implanted at low energy with low doses, the layers are much thinner than those of the high-dose SIMOX. The floated top Si layer is usually warped and impossible to be placed flat on the grid. In many cases, the presence of discontinuity in the BOX layer prevents the top Si layer from floating off. Therefore, in this study, samples for plan-view analysis were prepared by the back-thinning ion milling method. A small-cleaved piece of SIMOX wafer was glued on a glass platen with crystal bond, and cut into disks (3mm in diameter) with an ultrasonic disk cutter. The disk was removed from the platen and mounted to a glass holder with the wafer surface held down with crystal bond. The backside of the sample was thinned down to about 100 μm with a fine grinding paper. The specimen was dimpled and polished, as mentioned before, until the thinnest portion reached about 30 to 40 μm. The sample was removed from the glass holder and cleaned in acetone to prepare for further thinning with an ion mill. During ion milling, only one ion gun was used to thin only the backside of the sample. After the ion milling was concluded the sample was ready for TEM examination.

3.2.2 Scanning Electron Microscopy

Scanning electron microscopy (SEM) is one of the most efficient techniques for performing statistical analysis of structural defects in SIMOX due to its large field of view capability. In addition, SEM provides a more accurate area density measurement than for example TEM since all features that are imaged lie on the same plane of focus. SEM imaging was performed to determine the area density of silicon islands in the BOX layers of annealed samples. The presence of silicon islands in the BOX layer is undesirable since it undermines the dielectric integrity of the BOX such as its breakdown strength. The results from this analysis are important for the electrical characterization of the samples which is the next phase of this research. All samples prepared for SEM observation were sputtered-coated with thin layers of platinum to eliminate charging effect. The SEM images were recorded with Hitachi S-2460N at 25 keV.

SEM Sample Preparation

SEM sample preparation for detection of silicon islands in the BOX layer was done by wet chemical etching. Since the islands are located in the BOX layer, the top Si layer must be removed first in potassium hydroxide (KOH) and then the islands are delineated in HF as shown schematically in Figure 3.3. In the sequence, the top Si layer was removed in advance with isotropic wet etching by KOH at a controlled temperature for a predetermined time. The sample was promptly removed from the solution and washed in distilled water and dried. The KOH etching required knowledge of two parameters. The first parameter was the thickness of the top Si layer, which was determined by cross-

sectional TEM imaging of the same sample. Once the thickness of the top Si layer is known, the next step was to determine the time required to dissolve this thickness in KOH solution. The second required parameter is the etch rate of silicon in KOH solution. This parameter was yielded by the work of Kendall [65]. Figure 3.4 is graphical representation of the etch rate of silicon in the <100> and <110> direction in 44 weight % KOH aqueous solution. For the samples used in this study, a temperature of 50°C was selected which gave an etch rate of about 130 nm/min. After the removal of the top Si layer as shown in Figure 3.3 (b), The BOX layer was then etched selectively in 20:1 buffered HF, which leaves the silicon islands unetched as shown in Figure 3.3 (c). The etch rate was estimated at 100 nm/min. Table 3.2 gives the etching time used to dissolve the top Si layer and BOX layer in KOH and HF solutions, respectively. With the exception of the highest-dose sample ($7.0x10^{17}/cm^2$) all the BOX layers were dissolved to the middle. The BOX layer in the highest dose sample was completely dissolved since the silicon islands formed preferentially near the BOX/ substrate interface.

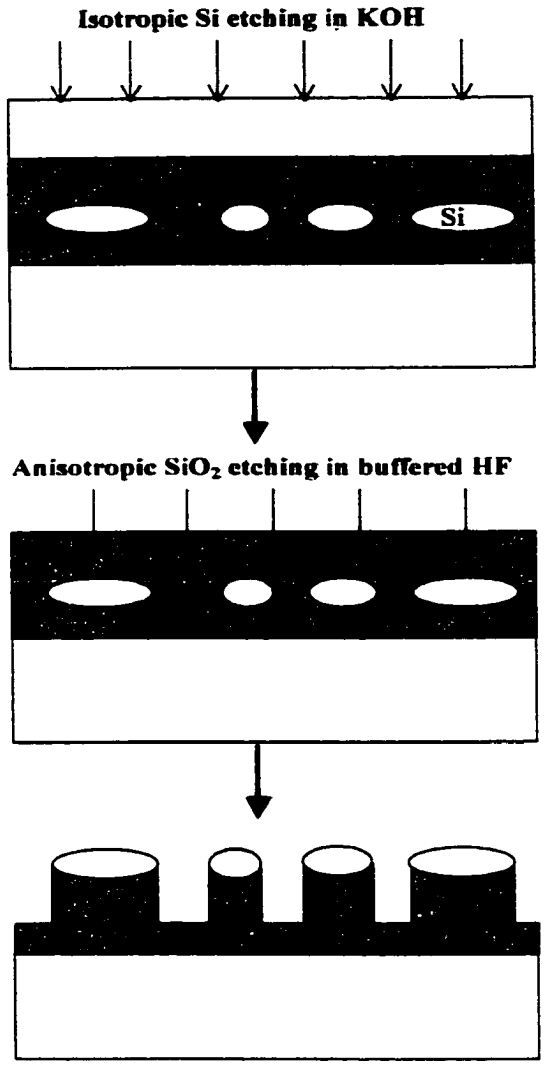

Figure 3.3 Schematic illustration of silicon islands etching sequence.

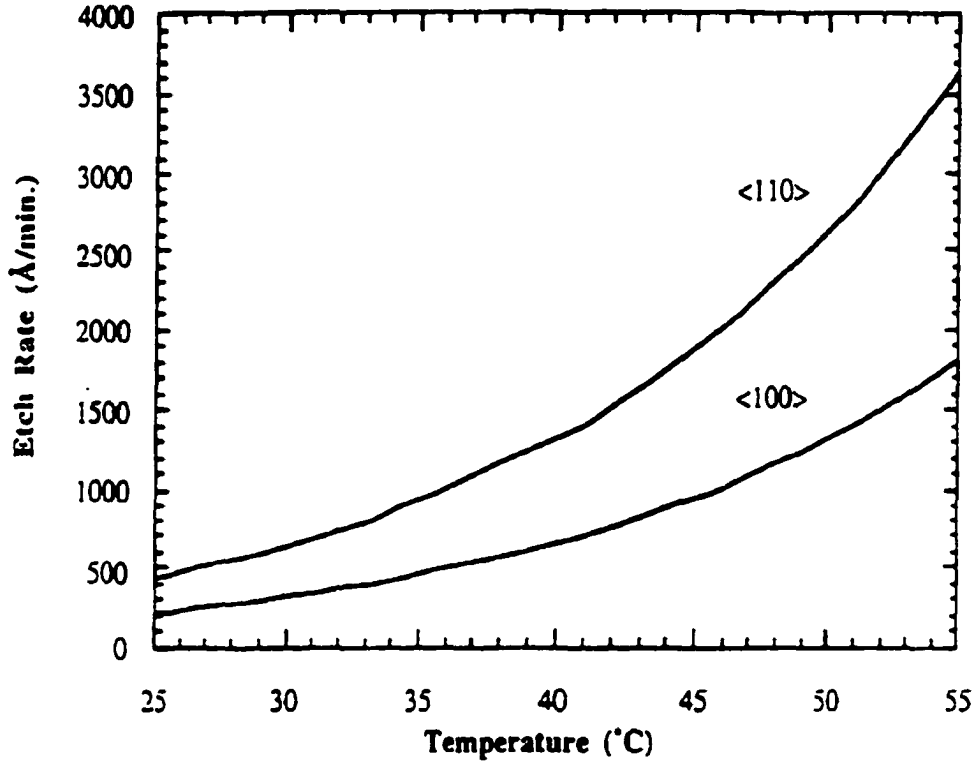

Figure 3.4 A graphical representation of the etch rate along the <100 and <110> directions of silicon wafer in 44% (weight) KOH aqueous solution as a function of temperature [65].

Table 3.2 Layer thickness vs. Etching time

Dose $X10^{17}/cm^2$	Top Si layer Thickness nm	Etch time in KOH sec	BOX Layer Thickness nm	Etch time in HF sec
2.5	93	43	57	17
3.0	80	37	73	22
3.5	68	31	88	26
4.0	58	27	115	35
5.0	38	18	142	43
7.0	24	11	177	106

3.2.3 Auger Electron Spectroscopy

Auger electron spectroscopy (AES) is among the most widely used surface analytical techniques capable of providing elemental composition of the top most layer of a solid. AES profiling is a commonly used technique for obtaining compositional information as a function of depth in the sample. To obtain a depth profile, a sample is placed in a vacuum chamber and energetic inert gas ions, for example 1 to 5 keV Ar ions are used to sputter the surface, followed by detection of Auger signals corresponding to the elements in the sputtered material. AES profiling was used to obtain the oxygen depth profiles of the as-implanted and annealed SIMOX samples. The objective for this analysis was to understand how the implanted oxygen redistributes during annealing. The AES spectra were obtained by Perkin-Elmer PHI600 Scanning Auger Microscopy (SAM) multiprobe system using a cylinder mirror analyzer. The instrument is located at the Dept. of Materials Science and Engineering, University of Arizona. An electron gun, located coaxially to the mirror analyzer, produced an electron beam of 200 μm in size at energy of 4 keV. The depth profiling was performed by sputtering the sample surface using 3 keV Ar ion beam at incidence angle of 10° with respect to the surface normal and an ion current density of 62 $\mu A/cm^2$. The sputtering area was 3 mm^2 and the area analyzed was 130 μm in diameter.

3.2.4 Rutherford Backscattering Spectrometry (RBS)/Ion Channeling

In this study, RBS/Ion channeling was used to determine the damage depth profiles in as-implanted and annealed samples. Channeling RBS analyses were performed using

He ion beam (accelerated by a Van de Graff accelerator) with energy of 2.0 MeV. The channeling was done along <100>, the axis normal to the sample surface. A goniometer was used for target manipulation and crystal orientation. RBS is a nondestructive analytical technique used for obtaining information about compositions of thin films, layered structures or bulks, measurements of surface impurities of heavy elements on substrates of lighter elements, lattice location of impurities in single crystal and defect distribution depth profile in single-crystal sample. In RBS, monoenergetic high-energy particles (in MeV), for instance, proton and alpha particle are used to bombard the sample surface. These incident particles will be scattered back when they collide with the sample materials. The energy of the backscattered particles will depend on the atomic mass and also the depth of the atoms which collide with the incident particles. Therefore we can determine accurately the chemical composition and also the depth of various elements within the sample.

Ion channeling in conjunction with ion backscattering provides information about the crystallinity of the target. When a sample is channeled, the rows of atoms in the lattice are aligned parallel to the incident He ion beam. The bombarding He ions will backscatter from the first few monolayers of material at the same rate as a non-aligned sample, but backscattering from buried atoms in the lattice will be drastically reduced since these atoms are shielded from the incident He ions by the atoms in the surface layers. For example, the backscattering signal from a single silicon sample, which is in channeling alignment along the <100> axis, will be approximately 3% of the backscattering signal from a non-aligned crystal, or amorphous or poly-crystalline

silicon. By measuring the reduction in backscattering when a sample is channeled, it is possible to quantitatively measure and profile the crystal perfection of a sample.

3.2.5 Optical Microscopy

Optical microscopy imaging provided information about the density of defects in the top Si layers of the annealed samples. The defects in the top Si layers were delineated using enhanced chemical etching solution that is based upon HF: HNO_3: H_2O [66]. The formula used was 50 ml HF (40%): 70 ml HNO_3 (70%): 170 ml H_2O (1.0 g $K_2Cr_2O_7$ + 4.0 g Cu $(NO_3)_2$:$3H_2O$). The etching procedure adopted in this work involved, immersion of the samples in the etching solution, using gently agitation to remove the reaction products. After rapid quenching in distilled water, thorough rinsing, and drying, the samples were then immersed in concentrated HF to form cavities in the BOX layer. After rinsing and drying the samples were examined under optical microscope at magnifications of 500X and 1000X.

CHAPTER 4

EFFECT OF IMPLANTATION DOSE

Implantation dose is a critical parameter in the processing of SIMOX material. The effect of dose on the microstructure of SIMOX is extremely important, as the performance of devices fabricated on SIMOX is critically dependent upon its quality. Moreover, from economic point of view, the implantation dose is the most important parameter since it controls the implantation time which largely determines the cost of SIMOX material. In this study, we have investigated the effect of implantation dose on the microstructure of SIMOX materials implanted at 65 keV in the dose range of $1.5x10^{17}/cm^2$ and $7.0x10^{17}/cm^2$. This work described in this chapter was conducted with the objective of determining the optimum dose at 65 keV for forming a continuous BOX layer without silicon islands and with low density of defects in the top Si layer. In the following sections, the effect of implantation dose on the microstructure of as-implanted and annealed samples, depth profile of implanted oxygen and implantation damage to the crystallinity of silicon are presented.

4.1 Microstructure of As-Implanted Samples

The state of the sample prior to annealing plays a key role in the development of the final structure of SIMOX. From the as-implanted structure an appropriate set of annealing conditions can be applied to obtain a good quality material. The microstructures of the as-implanted samples are presented first to serve as reference to the annealed samples.

Figure 4.1 shows cross-sectional TEM micrographs of as-implanted SIMOX samples with doses of (a) $2.0x10^{17}/cm^2$, (b) $3.5x10^{17}/cm^2$, (c) $4.5x10^{17}/cm^2$, (d) $5.0x10^{17}/cm^2$, and (e) $7.0x10^{17}/cm^2$. The microstructure after implantation changes as the implantation dose increases. In the dose range between $2.0x10^{17}/cm^2$ and $5.0x10^{17}/cm^2$, a continuous BOX layer is not formed. However, two or three distinct regions can be observed overlaying the substrate depending on the dose. In the microstructure of the lowest dose sample, two distinct regions can be identified, labeled I and II in Figure 4.1a. Region I is the top Si layer, which extends to about 115 nm below the sample surface. The region contains several multiply faulted defects (MFDs). No other observable crystallographic defects in this region were evident in the TEM micrograph. Many oxygen precipitates exist in the region as well and their sizes increase away from the sample surface. Region II is heavily defective and contains numerous oxygen precipitates. The region extends to about 215 nm below region I. This region forms around the depth corresponding to the peak concentration of the implanted oxygen, the projected range (R_p), which is about 147 nm at 65 keV according to calculation by TRIM-90 program [67]. In the dose range between $3.5x10^{17}/cm^2$ to $5.0x10^{17}/cm^2$, three distinct regions can be recognized in the microstructure of the samples (Figure 4.1b to 4d). The regions are labeled I, II, and III in Figure 4.1b. Region I is the same as described for the lowest dose sample in Figure 4.1a. The thickness of the region however, decreases to about 120 nm as the implantation dose increases. Region II is characterized by a mixed structure composed of striations of oxide and silicon formed around R_p. The vertical extent of region II increases with increasing implantation dose and the mixed structure

contains more oxide compared to silicon. Region III forms the defect-rich zone below the striated region and extends into the substrate. Defects observed in this region included {113} defects and small stacking faults.

In the highest dose sample ($7.0x10^{17}/cm^2$), a continuous BOX layer is formed. The microstructure of this sample is shown in Figure 4.1e. It consists of three regions: (i) a top Si layer of about 85 nm thick containing oxygen precipitates with sizes that increase from the surface to the Si/BOX interface, (ii) a continuous BOX layer of about 120 nm in thickness and (iii) a defect-rich zone below the BOX layer and extending about 250 nm into the substrate. As it can be seen from the micrograph in Figure 4.1e, there exist small, silicon striations near the BOX/substrate interface due to incomplete oxidation.

A high-resolution TEM (HRTEM) imaging was performed in order to obtain more information on the mixed structure observed in the as-implanted samples. Figure 4.2 shows a HRTEM micrograph of the mixed structure of the sample implanted with a dose of $4.5x10^{17}/cm^2$. The two phases, marked A and B in the micrograph correspond to striations of silicon and oxygen precipitates, respectively. In phase B, no lattice is observed indicating an amorphous structure of SiO_2. In phase A on the other hand, most of the silicon retain their crystallinity as revealed by the appearance of the lattice fringes. This region contains also pockets of small oxygen precipitates.

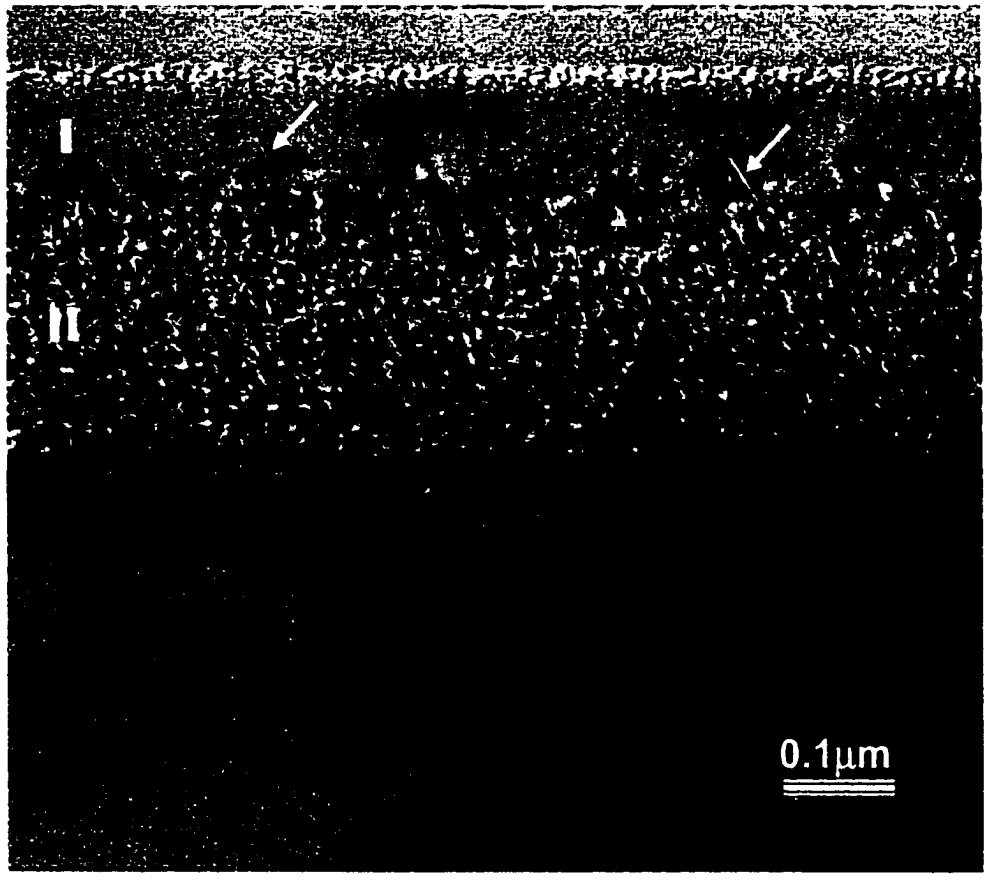

(a) $2.0x10^{17}/cm^2$

Figure 4.1 Cross-sectional TEM micrographs of SIMOX samples implanted at 65 keV, 500°C to a dose of (a) $2.0x10^{17}/cm^2$; (b) $3.5x10^{17}/cm^2$; (c) $4.5x10^{17}/cm^2$; (d) $4.5x10^{17}/cm^2$; and (e) $7.0x10^{17}/cm^2$. Arrows indicate multiple faulted defects (MFDs).

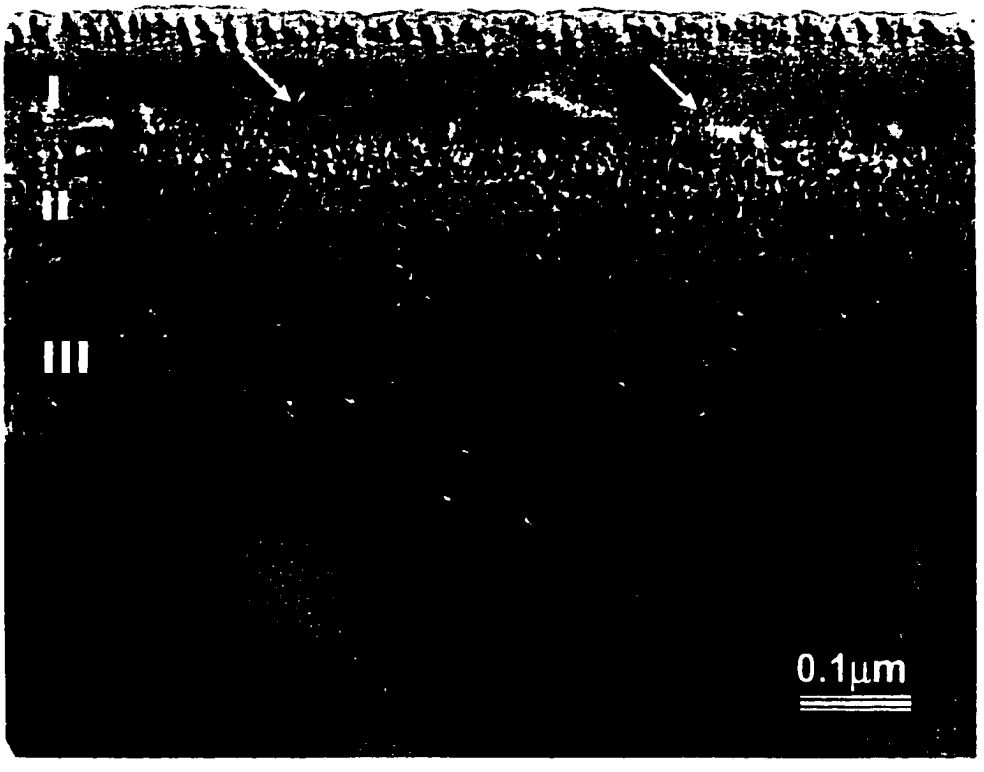

Figure 4.1 cont., (b) $3.5x10^{17}/cm^2$

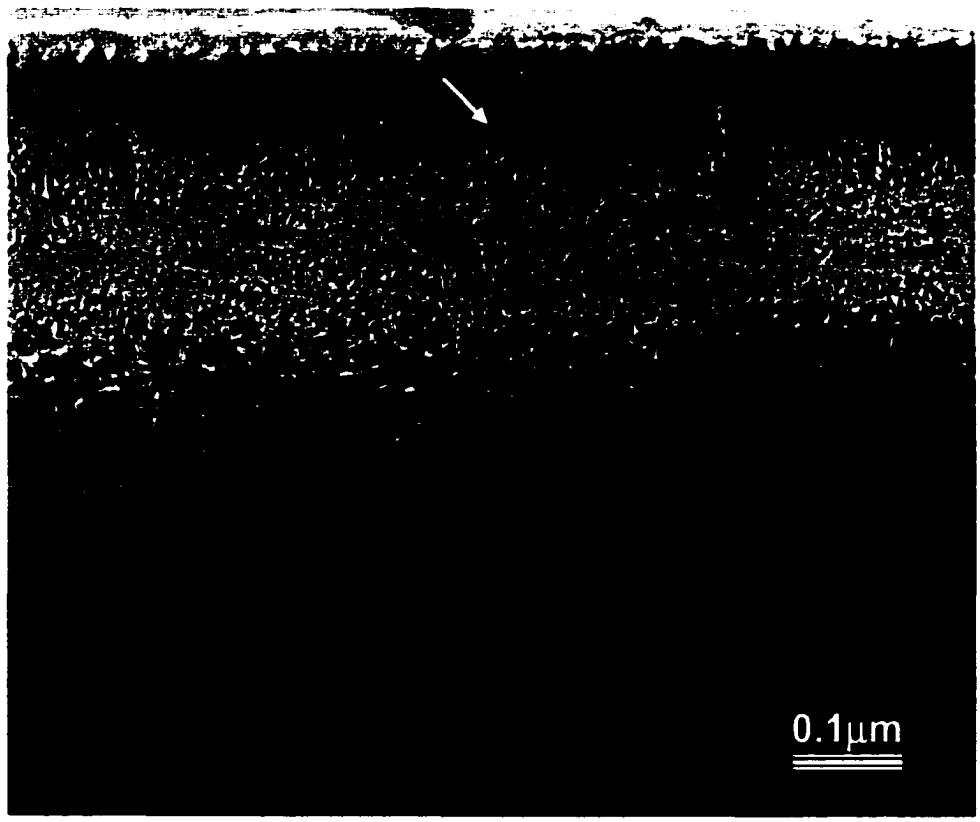

Figure 4.1 cont., (c) $4.5x10^{17}/cm^2$

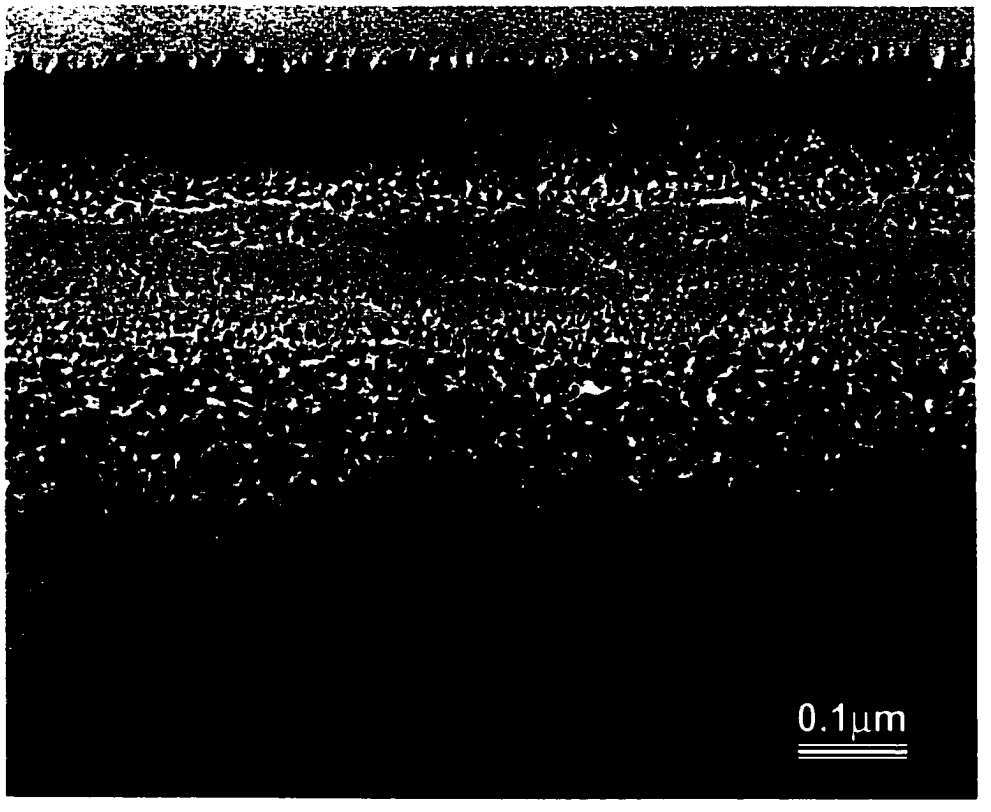

Figure 4.1 cont., (d) $5.0 \times 10^{17}/cm^2$

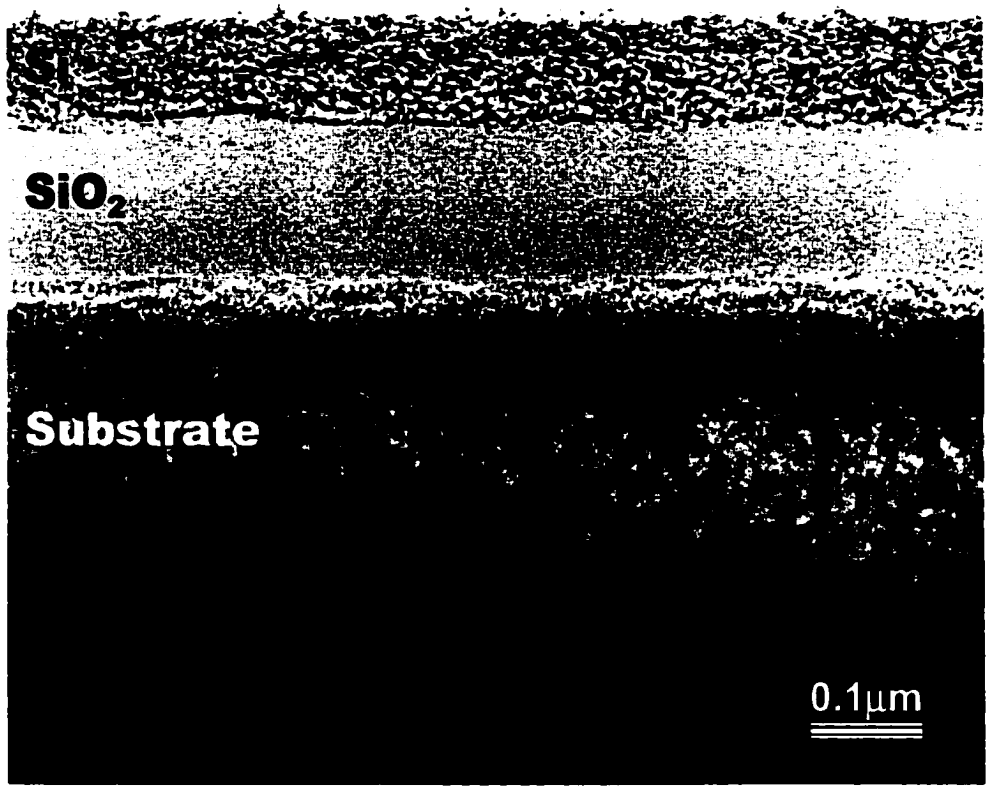

Figure 4.1 cont., (e) $7.0x10^{17}/cm^2$

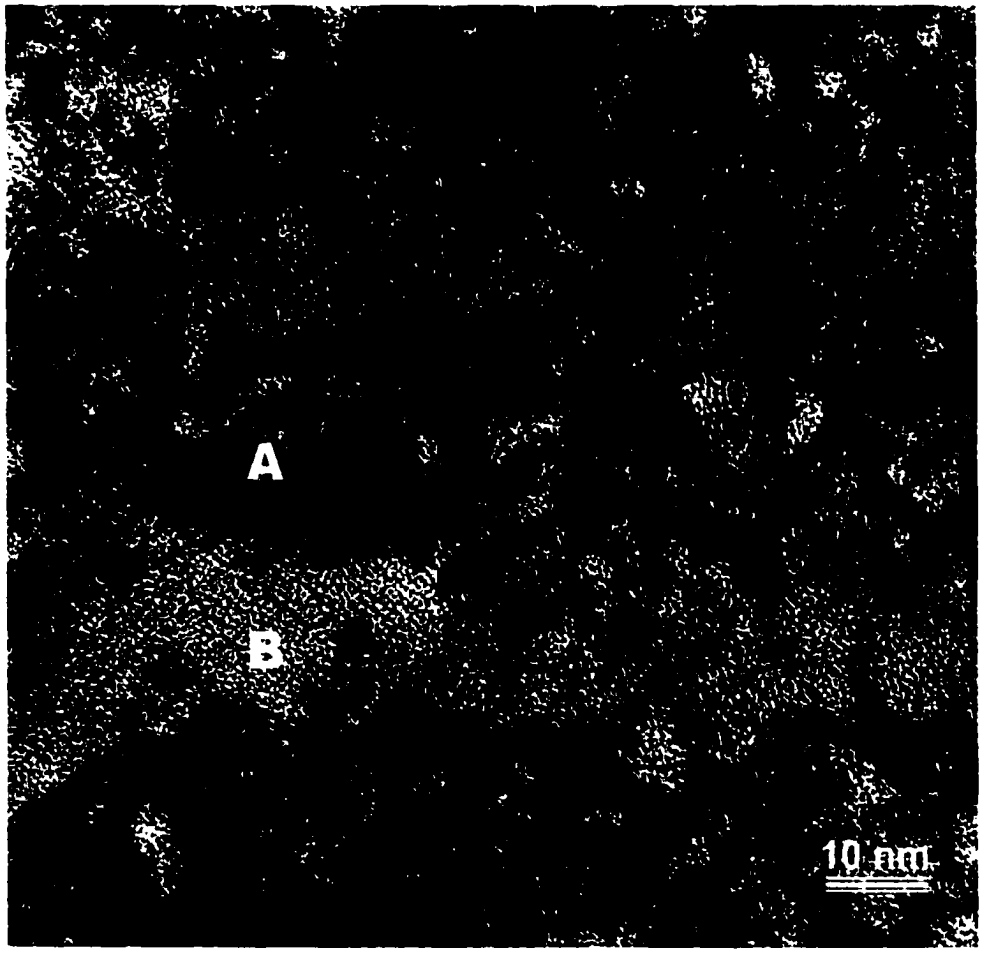

Figure 4.2 HRTEM micrograph of the mixed structure in the sample implanted with a dose of $4.5 \times 10^{17}/cm^2$. A and B indicate silicon-rich and oxide-rich regions, respectively.

4.2 Oxygen Concentration Profiles in As-implanted Samples

SIMS depth profile analysis was performed in the as-implanted samples with the objective of understanding how the implantation dose affects the depth profile of the implanted oxygen. This analysis was performed by Ibis and it covered the range of samples used in this study

Figure 4.3 shows SIMS oxygen concentration profiles in unmasked silicon wafers implanted at 65 keV with doses of 1.5, 2.0, 2.5, 3.5, 4.0, 4.5, and $7.0x10^{17}/cm^2$ [68]. A skewed Gaussian distribution is observed for the implanted doses in the range of $1.5x10^{17}/cm^2$ to $4.5x10^{17}/cm^2$. At a dose of $7.0x10^{17}/cm^2$ the oxygen distribution has become flat-topped, which indicates the formation of a continuous layer of SiO_2. In the lowest dose sample, the profile has a peak around 155 nm from the surface which is consistent with the value around 147 nm obtained from the simulation program, TRIM-90 [67]. The full width at half-maximum was about 134 nm. The oxygen peak tended to shift away from the surface with increasing dose (155 to 180 nm). This is due to increased sputtering at the surface with increasing dose. The full width at half-maximum, however tended to decrease with increasing dose up to $4.5x10^{17}/cm^2$ (134 to 94 nm) and then increased to 156 nm at the highest implanted dose ($7.0x10^{17}/cm^2$). This occurs because as the dose increases, oxygen builds up faster around the projected range until the stoichiometric concentration is reached when the profile expands towards the wings.

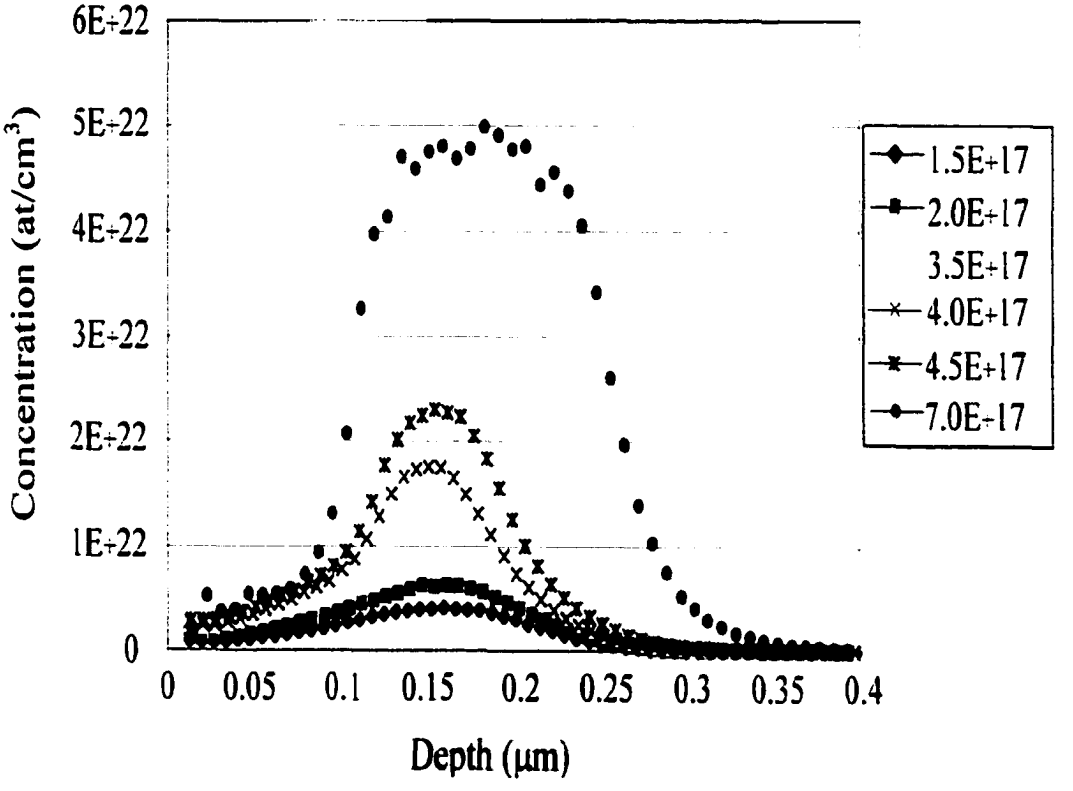

Figure 4.3 SIMS depth profiles of oxygen concentrations in as-implanted samples at 65 keV [68].

4.3 Crystal Disorder Profiles in As-implanted Samples

Figure 4.4 shows random and channeled RBS spectra from as-implanted samples with doses ranging from $2.0x10^{17}/cm^2$ to $7.0x10^{17}/cm^2$. Regions I, II, and III marked in the figure correspond to the top Si layer, the precipitate or BOX layer depending on the dose, and the damage extent into the substrate, respectively. It can be seen that in regions I and III, the yield of the channeled spectrum for each as-implanted sample is less than that of the random spectrum, which indicates that some degree of crystallinity was retained after implantation. The degree of crystallinity retained depends on the implantation dose which was found as expected to increase with decreasing dose. In region II, the channeling trend is opposite to that of regions I and III. The channeled spectrum is lowest in the highest-dose sample ($7.0x10^{17}/cm^2$) and tends to increase with decreasing implantation dose. This suggests that this region becomes more disordered with decreasing implantation dose. This is unusual because generally as more oxygen becomes available through increased dose, the more oxide is formed. More studies are needed to clarify this behavior. The extent of implantation damage to silicon in the top Si layer (region I) was evaluated by determining the crystal disorder parameter (χ_{min}) which is defined as the ratio of the channeled to the random backscattering yield. The value of χ_{min} for each sample was obtained and the data are collated in Figure 4.5. For each sample, χ_{min} was assessed just below the depth of the damage peak. The crystal disorder was found to increase with increasing dose as is evident by the increase of χ_{min} from 20% for the lowest dose sample to 70% for the highest dose sample.

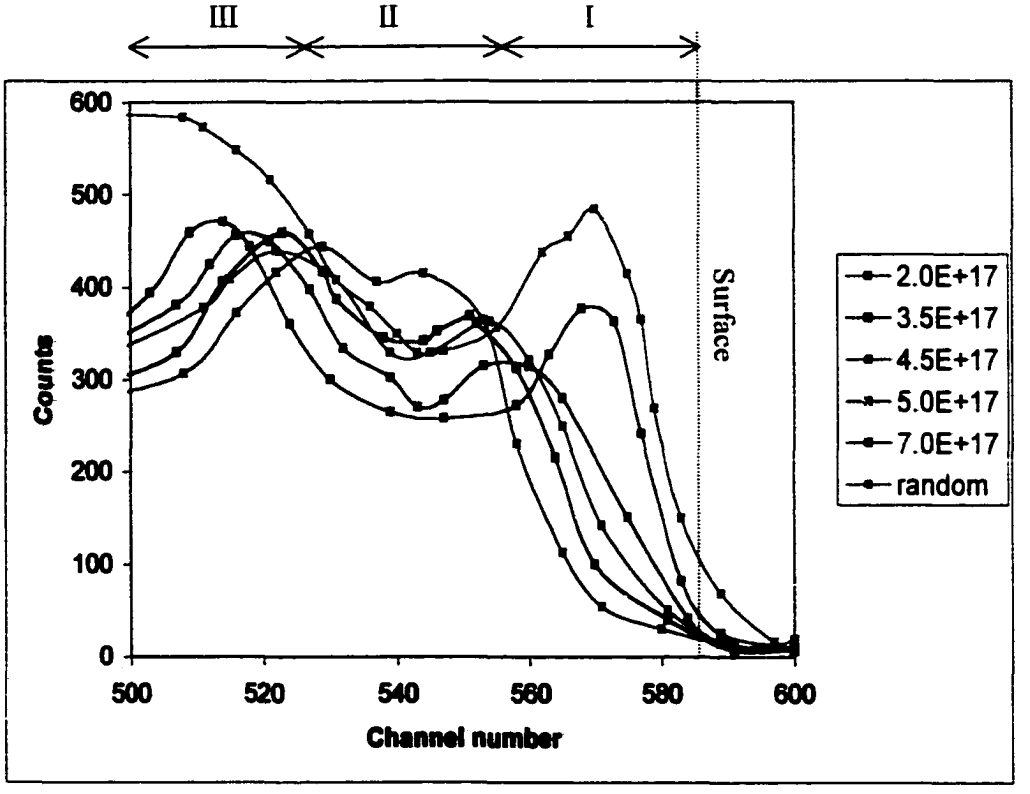

Figure 4.4 Random and channeled RBS spectra from as-implanted samples at 65 keV.

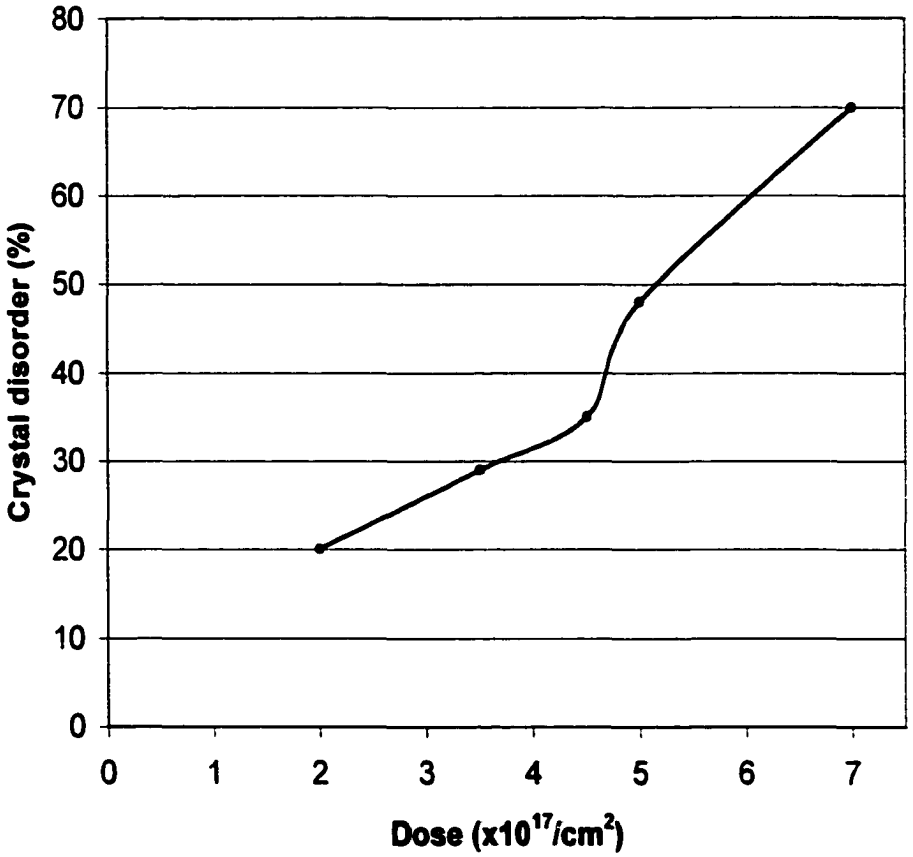

Figure 4.5 A plot of χ_{min} as function of implantation dose at 65 keV.

4.4 Microstructure of Annealed Samples

The work described in this section was conducted with the objective of studying the effect of implantation dose on the microstructure of fully annealed samples. The doses studied ranged from $1.5x10^{17}/cm^2$ to $7.0x10^{17}/cm^2$. All the samples were annealed at 1350°C for 4 hours under Ar + 0.5%O_2.

Figures 4.6 to 4.13 show TEM micrographs of fully annealed SIMOX samples with doses of $1.5x10^{17}/cm^2$, $2.0x10^{17}/cm^2$, $2.5x10^{17}/cm^2$, $3.0x10^{17}/cm^2$, $3.5x10^{17}/cm^2$, $4.0x10^{17}/cm^2$, $5.0x10^{17}/cm^2$, and $7.0x10^{17}/cm^2$, respectively. The microstructures of these samples exhibit significant sensitivity towards variations in the implantation dose. In the lowest-dose sample ($1.5x10^{17}/cm^2$), there is no continuous BOX layer but only a collection of disjointed SiO_2 precipitates in the vicinity of the oxygen projected range (R_p) as shown in Figure 4.6 (a). The thickness of the precipitates is approximately 70 nm and the mean distance of separation between them is about 140 nm. Figure 4.6 (b) shows a plan-view TEM micrograph of this sample. The plan-view image from this projection revealed that the layer consists of 60% oxide and 40% silicon. For the second lowest-dose sample ($2.0x10^{17}/cm^2$) there is a continuous BOX layer without any observable silicon islands, as shown in the cross-sectional and plan-view TEM micrographs (Figures 4.7(a) and 4.7(b), respectively). For the next higher dose ($2.5x10^{17}/cm^2$), again the BOX layer formed continuously without any silicon islands observed as evident from the cross-sectional and plan-view TEM micrographs in Figures 4.8(a) and 4.8(b), respectively. For doses above $2.5x10^{17}/cm^2$, a continuous BOX layer formed as well but with silicon islands present as shown in the TEM micrographs (Figures 4.9 to 4.13) and SEM images

of the silicon islands presented in Figure 4.14. In the dose range between $3.0x10^{17}/cm^2$ to $4.0x10^{17}/cm^2$, the silicon islands occupied the center of the BOX layer (Figures 4.9 to 4.11). In the sample implanted with the dose of $5.0x10^{17}/cm^2$ (Figure 4.12a), the silicon islands varied in sizes and were distributed over the thickness of the BOX layer with the largest occurring near the BOX/substrate interface. In the highest-dose sample ($7.0x10^{17}/cm^2$), the silicon islands diminished in size and occupied a smaller volume at the bottom of BOX layer (Figure 4.13a). The plan-view and SEM micrographs in Figure 4.13 (b) and Figure 4.14 (d), respectively show a lower density of islands in this sample.

The thickness of the top Si layer and the BOX layer of the above samples were measured from TEM images. The data are listed in Table 4.1 and plotted in Figure 4.15. The thickness of the top Si layer decreases while that of the BOX layer increases with increasing dose. The calculated values of the layers are also listed Table 4.1.The thickness of the BOX layer, T^A_{SiO2} was calculated from the following simple relationship [69].

$$T^A_{SiO2} = (\Phi/No^{SiO2}) \qquad 4.1$$

where Φ is the implantation dose ($\geq \Phi c^A$, the critical dose to form a continuous BOX layer after annealing) and No^{SiO2} is the number of oxygen atoms per unit volume in SiO_2 ($4.48x10^{22}/cm^3$ for thermally grown oxide). The thickness of top Si layer, T^A_{Si} was calculated from the following relationship [69].

$$T^A_{Si}(nm) = R_p(nm) - 11.0x\Phi\ [10^{17}/cm^2] \qquad 4.2$$

where R_p is the implanted oxygen projected range. Comparison of calculated and measured values for the top Si layer shows that the former are higher than the latter. For

the BOX layer on the other hand, the observed values are higher than the calculated ones. The discrepancy or fairly good agreement at some of the doses is discussed in Chapter 7.

Silicon islands in the BOX layers of the samples were quantitatively analyzed through an etching experiment and observed in SEM. The data are listed in Table 4.2 and plotted in Figure 4.16. The island density increases with increasing dose up to $5.0x10^{17}/cm^2$ and then decreases at the dose of $7.0x10^{17}/cm^2$. Finally, the density of defects in the top Si layers of the annealed samples was determined through the etch-pit technique and observed in an optical microscope. The densities of the defects are listed in Table 4.3 and plotted as function of dose in Figure 4.17. The results show that there exists a threshold dose of $3.5x10^{17}/cm^2$ at which a low defect density is formed. The density of the defects increases with dose away from this threshold dose. The observed trend in the defect density plot is discussed in Chapter 7.

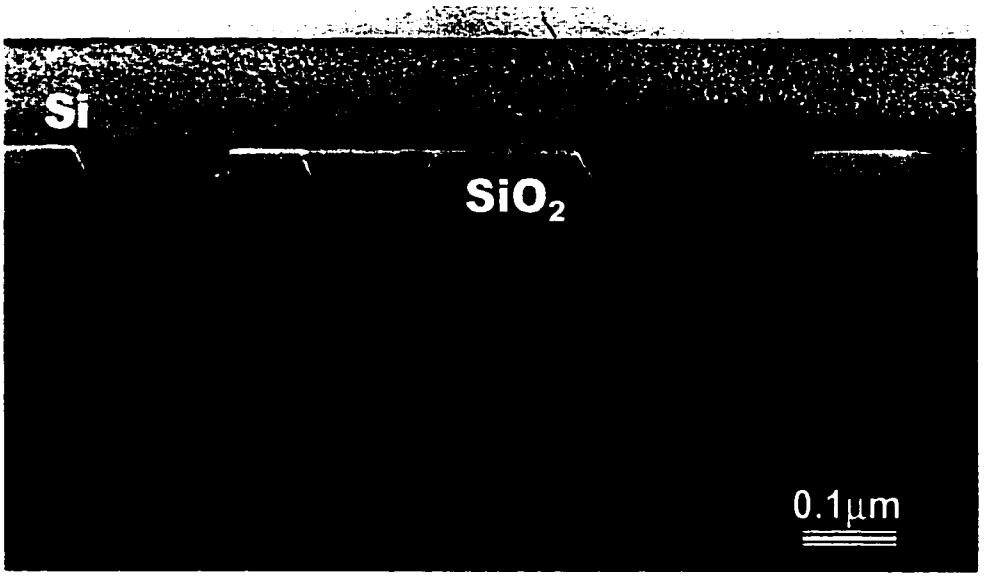

(a) Cross-sectional

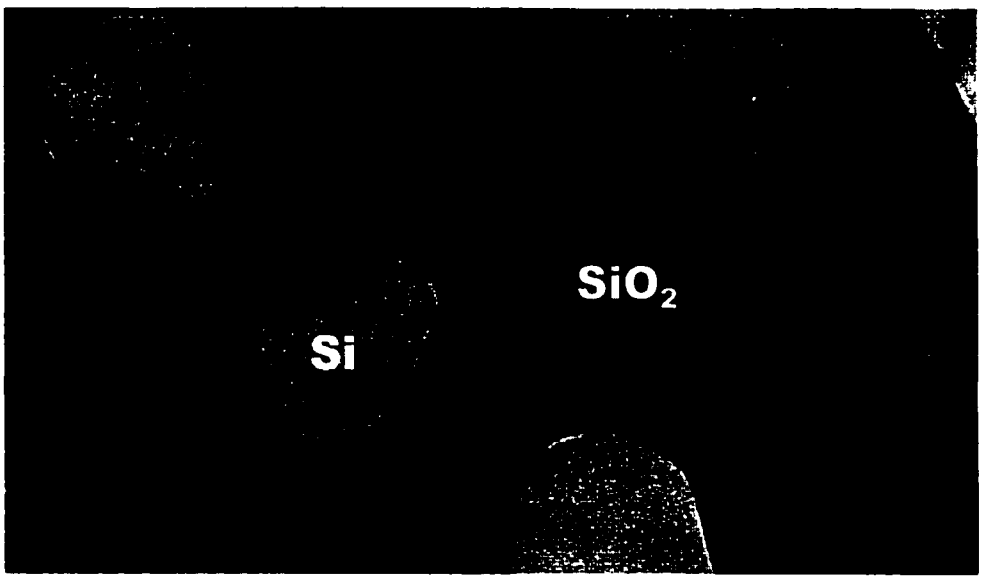

(b) Plan-view

Figure 4.6 TEM micrographs of (a) cross-sectional and (b) plan-view of SIMOX sample implanted with a dose of $1.5 \times 10^{17}/cm^2$ and annealed at 1350°C for 4 hours.

(a) Cross-sectional

(b) Plan-view

Figure 4.7 TEM micrographs of (a) cross-sectional and (b) plan-view of SIMOX sample implanted with a dose of $2.0 \times 10^{17}/cm^2$ and annealed at 1350°C for 4 hours.

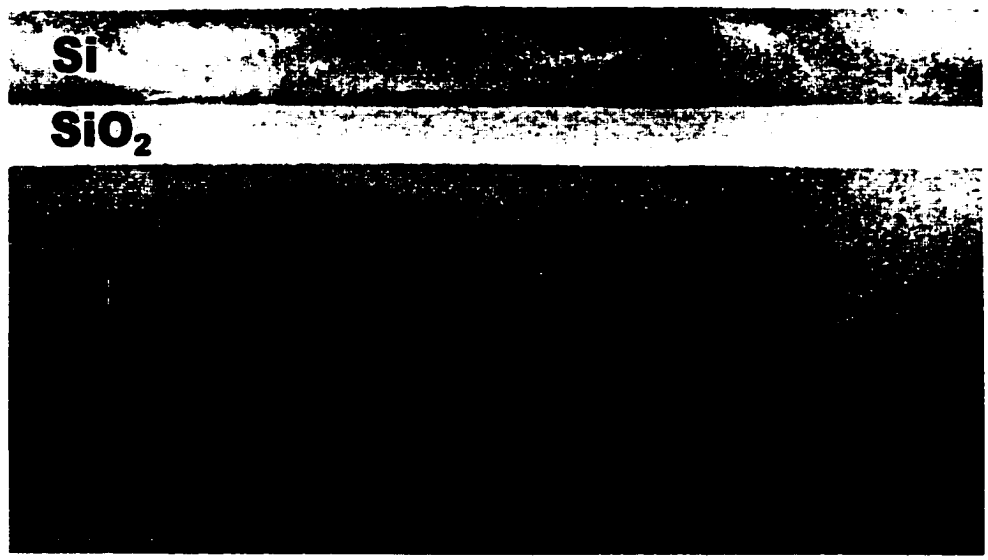

(a) Cross-sectional

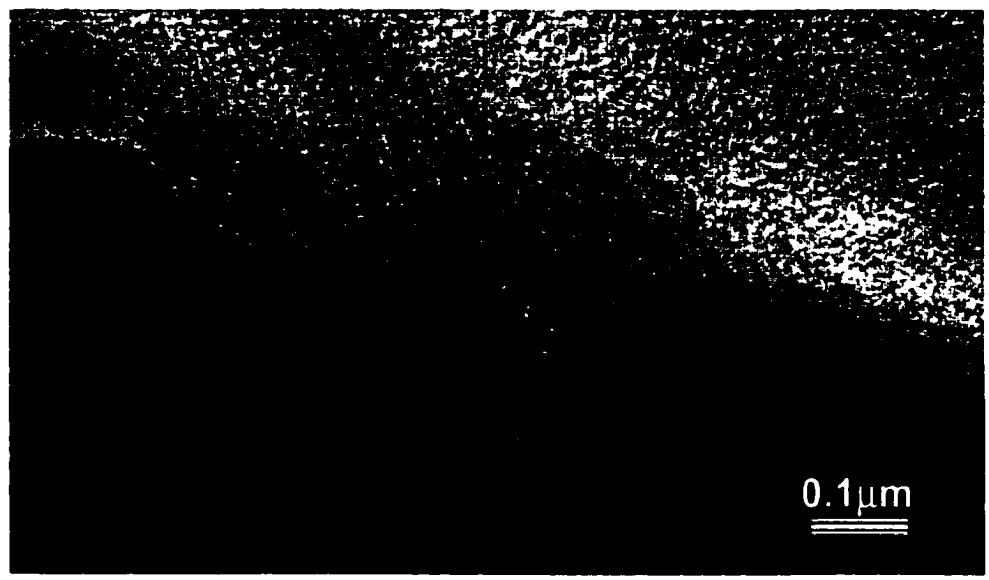

(b) Plan-view

Figure 4.8 TEM micrographs of (a) cross-sectional and (b) plan-view of SIMOX sample implanted with a dose of $2.5 \times 10^{17}/cm^2$ and annealed at 1350°C for 4 hours.

(a) Cross-sectional

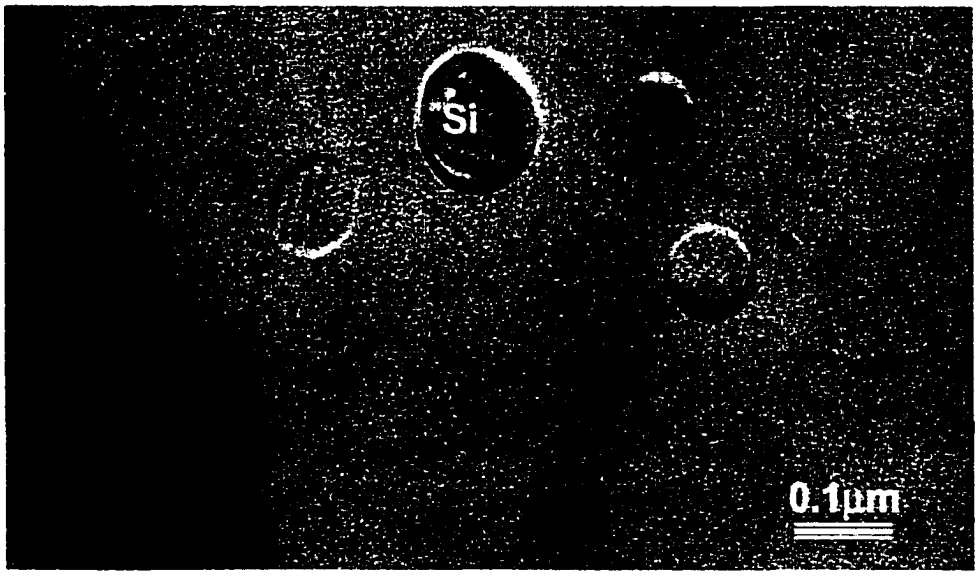

(b) Plan-view

Figure 4.9 TEM micrographs of (a) cross-sectional and (b) plan-view of SIMOX sample implanted with a dose of $3.0 \times 10^{17}/cm^2$ and annealed at 1350°C for 4 hours.

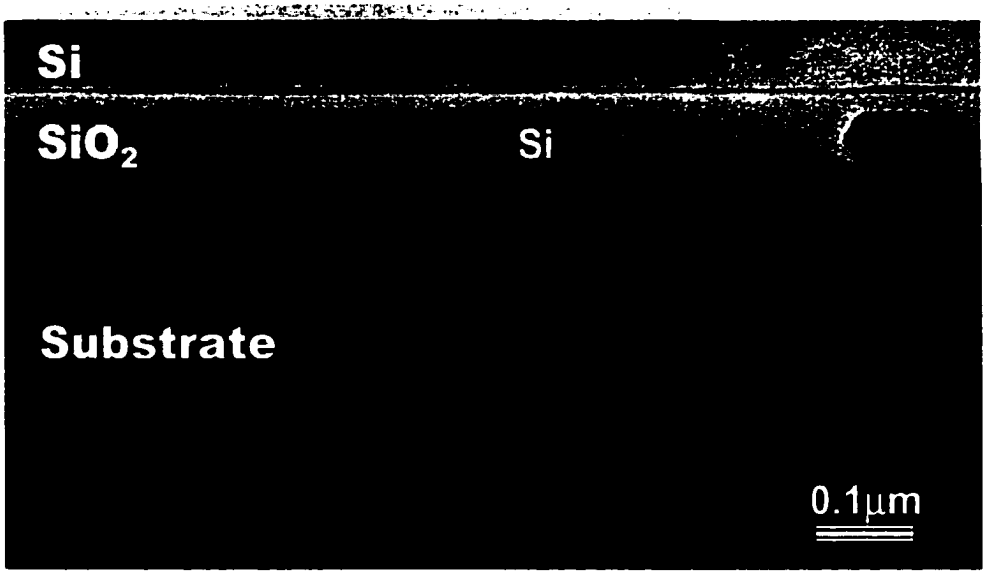

(a) Cross-sectional

(b) Plan-view

Figure 4.10 TEM micrographs of (a) cross-sectional and (b) plan-view of SIMOX sample implanted with a dose of $3.5 \times 10^{17}/cm^2$ and annealed at 1350°C for 4 hours.

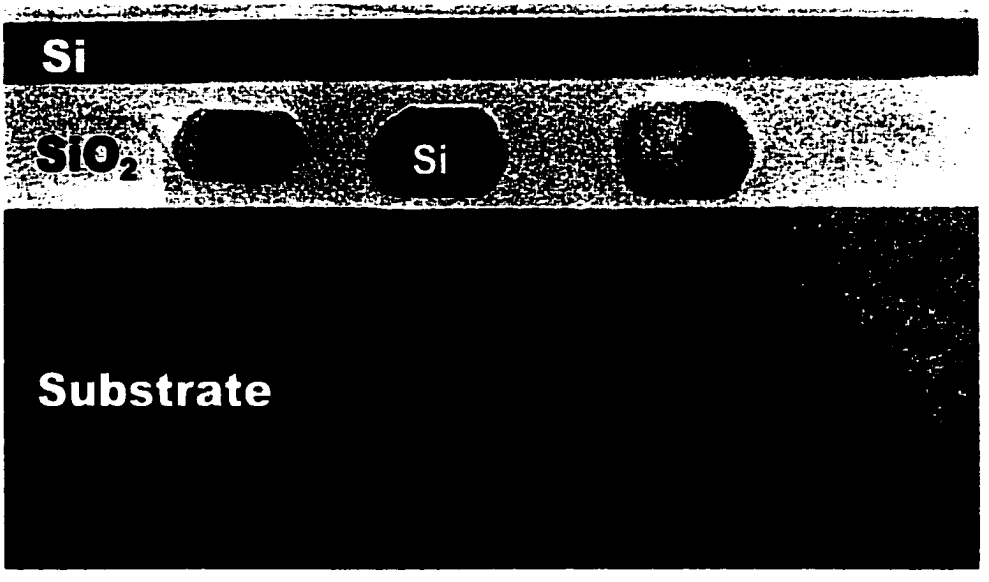

(a) Cross-sectional

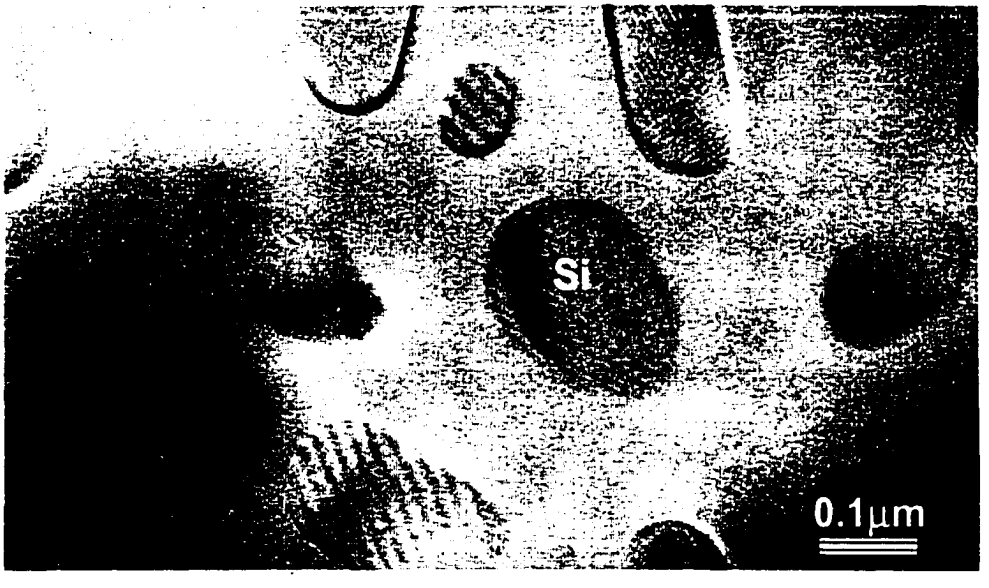

(b) Plan-view

Figure 4.11 TEM micrographs of (a) cross-sectional and (b) plan-view of SIMOX sample implanted with a dose of $4.0 \times 10^{17}/cm^2$ and annealed at 1350°C for 4 hours..

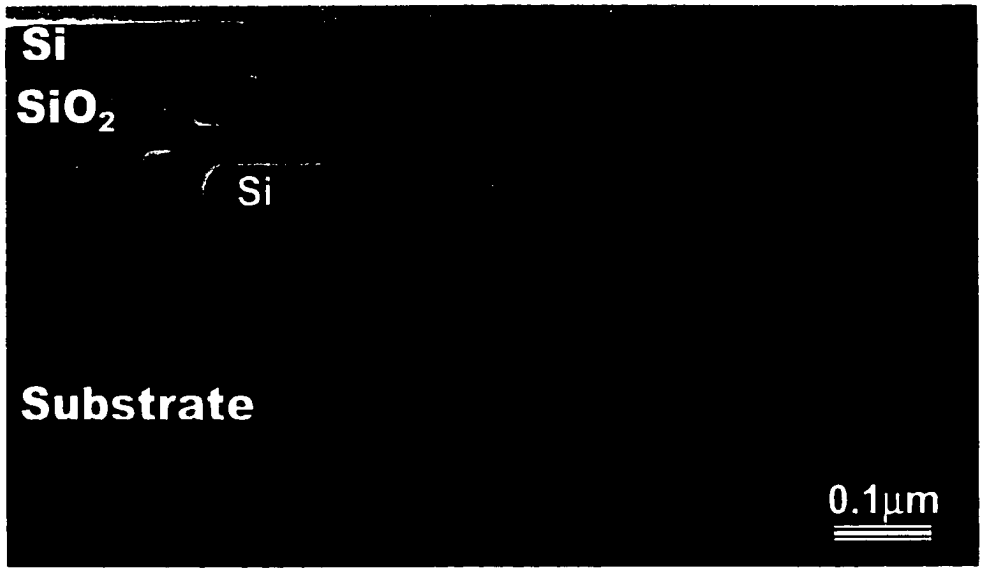

(a) Cross-sectional

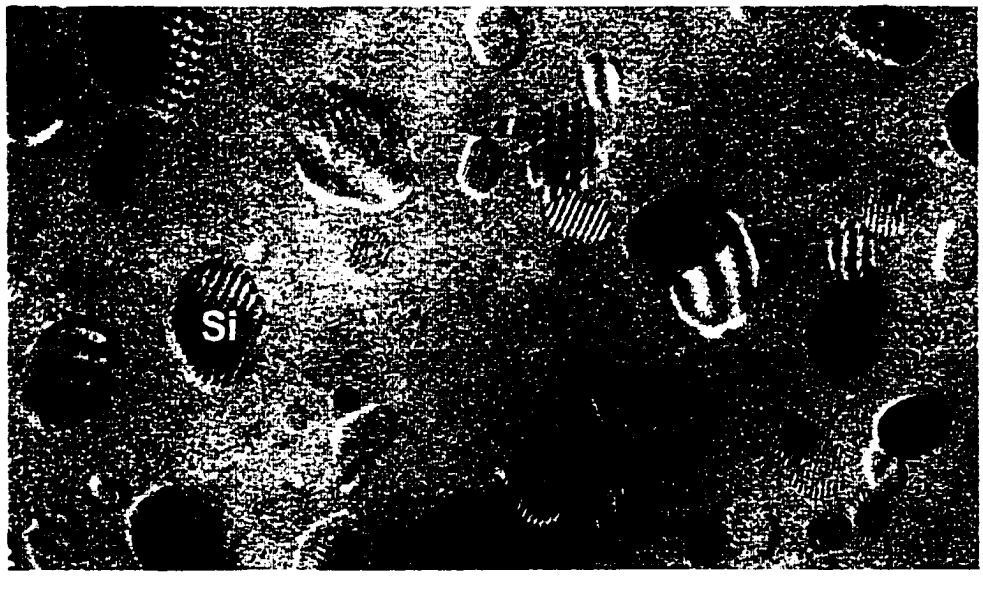

(b) Plan-view

Figure 4.12 TEM micrographs of (a) cross-sectional and (b) plan-view of SIMOX sample implanted with a dose of $5.0 \times 10^{17}/cm^2$ and annealed at 1350°C for 4 hours.

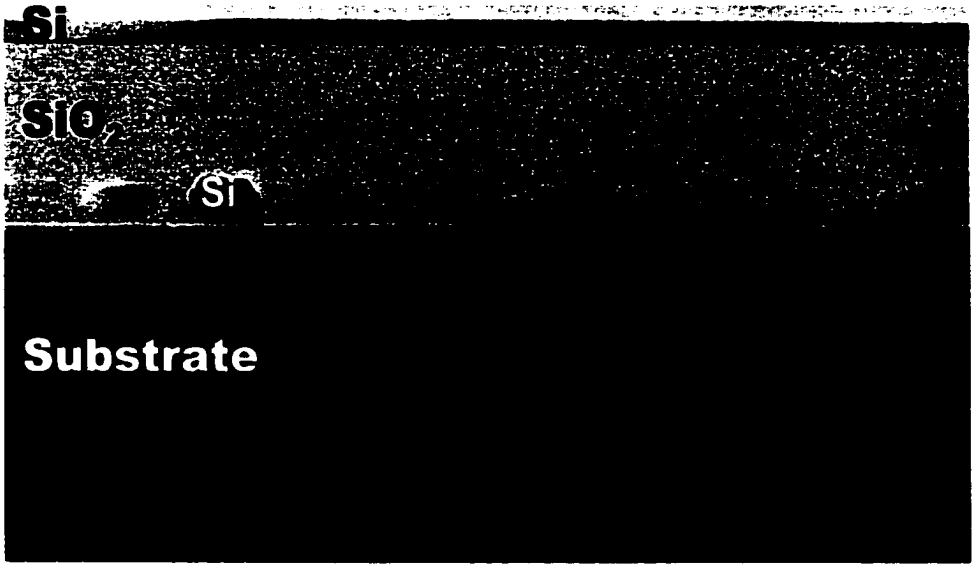

(a) Cross-sectional

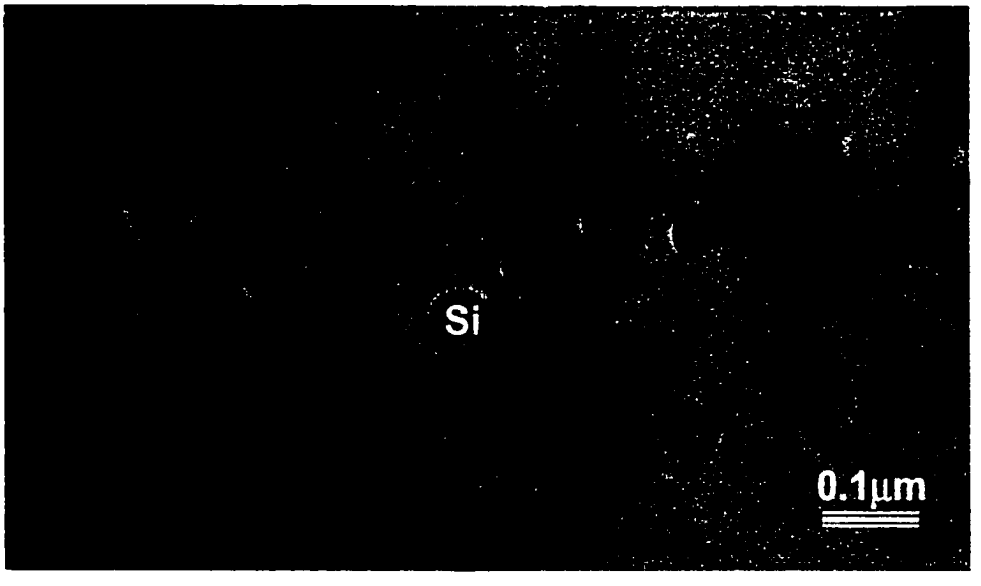

(a) Plan-view

Figure 4.13 TEM micrographs of (a) cross-sectional and (b) plan-view of SIMOX sample implanted with a dose of $7.0 \times 10^{17}/cm^2$ and annealed at 1350°C for 4 hours.

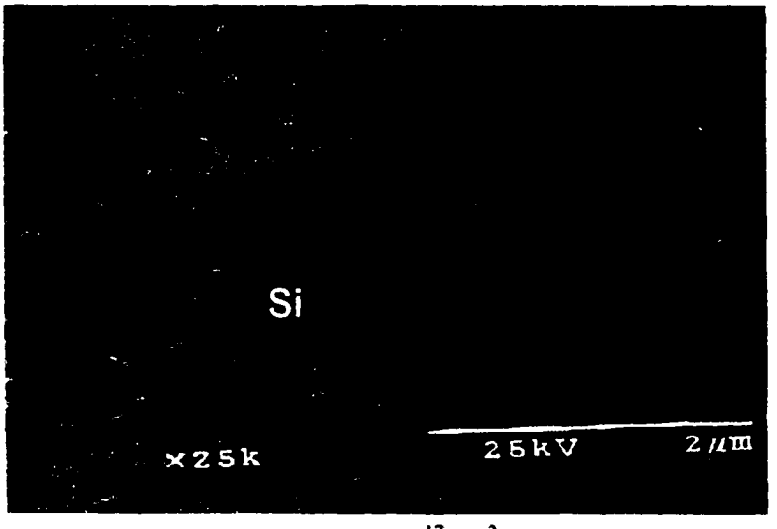

(a) $3.0x10^{17}/cm^2$;

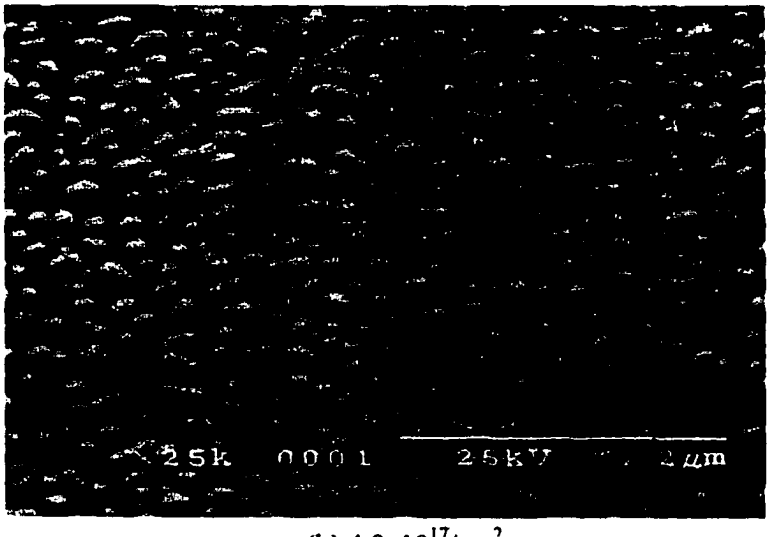

(b) $4.0x10^{17}/cm^2$;

Figure 4.14 SEM micrographs of silicon islands in SIMOX sample implanted at 65 keV with dose of (a) $3.0x10^{17}/cm^2$; (b) $4.0x10^{17}/cm^2$; (c) $5.0x10^{17}/cm^2$; and (d) $7.0x10^{17}/cm^2$ and annealed at 1350°C for 4 hours.

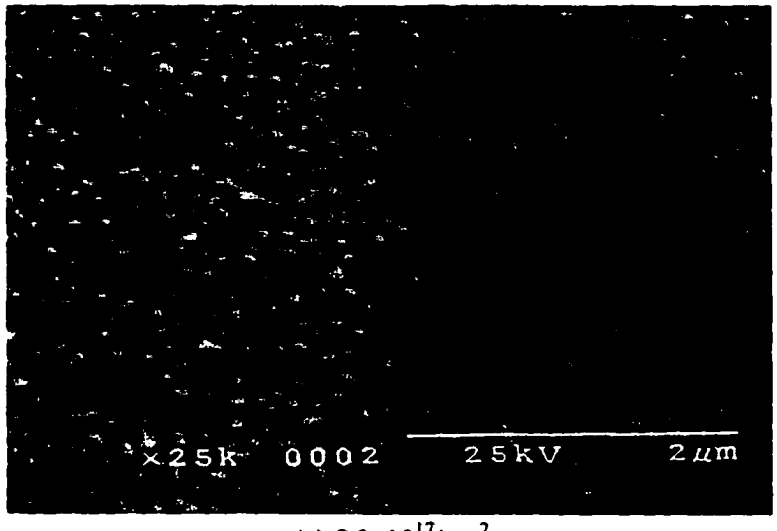

(c) $5.0x10^{17}/cm^2$;

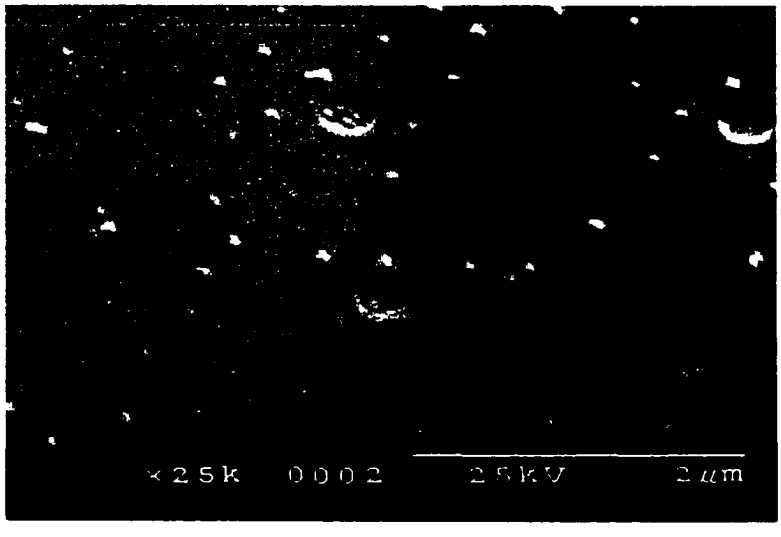

(d) $7.0x10^{17}/cm^2$;

Figure 4.14 cont., (c) $5.0x10^{17}/cm^2$ and (d) $7.0x10^{17}/cm^2$.

Table 4.1 A comparison of the calculated and experimentally determined layer thickness of annealed SIMOX samples over the range of implantation doses considered in this study.

	Thickness of top Si layer			Thickness of BOX layer		
Dose ($x10^{17}/cm^2$)	Cal. (nm)	Exp. (nm)	Deviation from Cal. (%)	Cal. (nm)	Exp. (nm)	Deviation from Cal. (%)
2.0	126	105	-17	44	48	8
2.5	120	93	-22	56	57	2
3.0	115	80	-30	67	73	9
3.5	109	68	-37	78	87	11
4.0	104	58	-44	89	115	28
5.0	93	38	-59	111	149	33
7.0	71	24	-66	156	177	13

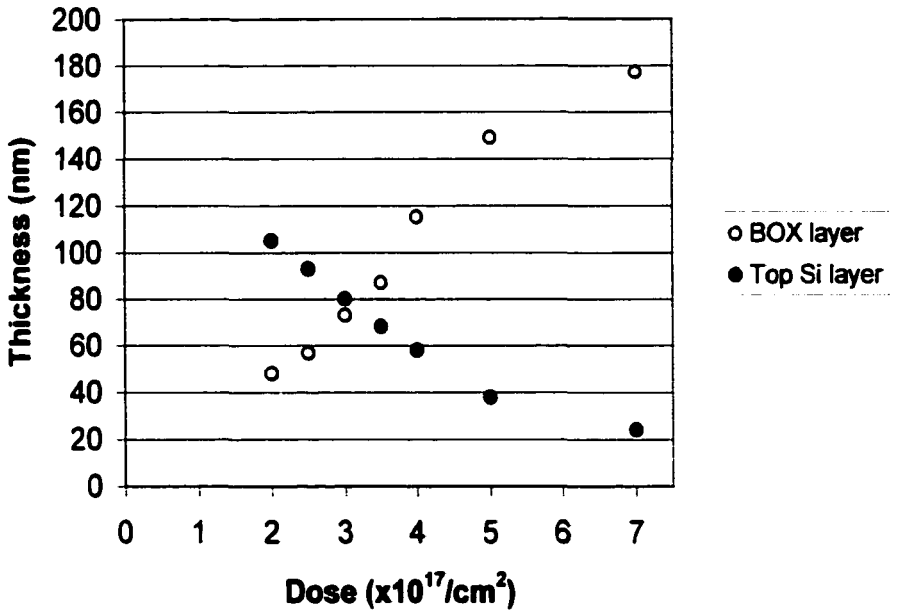

Figure 4.15 Thickness of the top Si and BOX layers as a function of implantation dose.

Table 4.2 The density of Si islands in the BOX layer of annealed SIMOX as a function of implantation dose. The sample implanted with dose of $1.5x10^{17}/cm^2$ did not have a continuous BOX layer and no islands were observed in the samples implanted with dose of $2.0x10^{17}/cm^2$ and $2.5x10^{17}/cm^2$.

Dose ($x10^{17}/cm^2$)	Si island density ($x10^8/cm^2$)
1.5	-
2.0	-
2.5	-
3.0	18.2
3.5	32.9
4.0	44
5.0	109
7.0	1.3

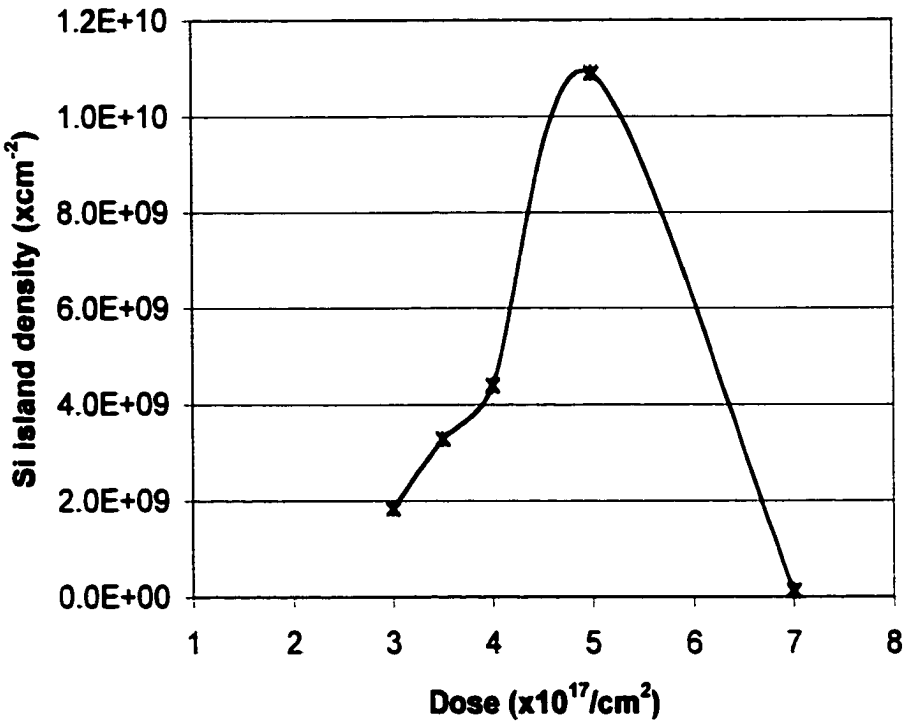

Figure 4.16 The density of Si islands in the BOX layer of SIMOX as a function of implantation dose.

Table 4.3 The density of defects in the top Si layer as a function of implantation dose

Dose ($x10^{17}/cm^2$)	Defect density ($x10^3/cm^2$)
1.5	100
2.5	40
3.0	3
3.	1.5
4.0	2.0
5.0	700

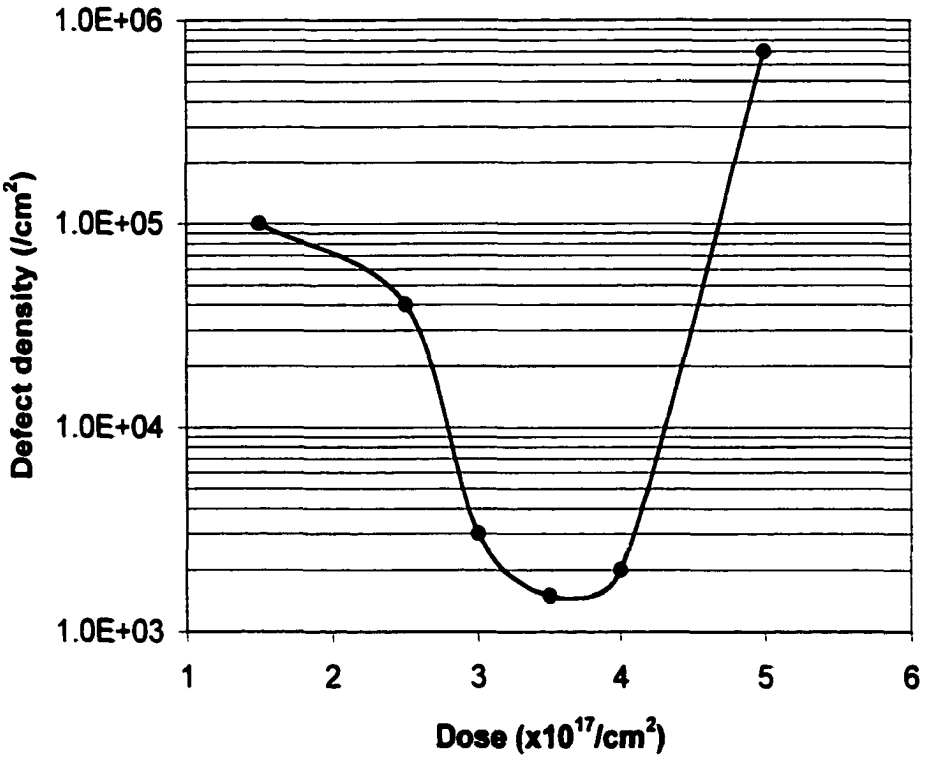

Figure 4.17 The density of defects in the top Si layer of annealed SIMOX (uncapped during annealing) as a function of implantation dose.

CHAPTER 5

EFFECT OF INTERMEDIATE-TEMPERATURE ANNEALING

Ion implantation introduces severe damage to the crystallinity of silicon. High-temperature annealing between 1300-1350°C is therefore required to restore the crystallinity and to complete the formation of the SIMOX structure. A drastic change occurs in the microstructure during the heating up to the final temperature. Though the industrial process focuses on the final annealing temperature, it is important to understand the microstructural developments leading to the final temperature annealing step which helps using right annealing matrix for achieving good quality material. In this study, intermediate-temperature annealing was performed at 900°C, 1100°C and 1200°C each for 2 hours to understand the microstructural developments which take place when an as-implanted sample is ramped up (gradually heated up) to the final annealing temperature. Through TEM, AES, and RBS analyses, it will be shown how the microstructure changes, oxygen redistribute and the crystal recovery process advances at the above temperatures.

5.1 Microstructural Developments

The samples used for this study were implanted at 65 keV to a dose of $4.5 \times 10^{17}/cm^2$. The microstructure of the as-implanted sample is presented here as reference point for comparing with the annealed ones. Figure 5.1 shows cross-sectional TEM micrograph of the as-implanted sample. A continuous BOX layer does not form in this sample. However, three distinct regions labeled I, II, and III in the figure the can be

recognized overlaying the substrate. Region I is the top Si layer of about 0.1μm in thickness and contains several MFDs as indicated by arrows. Region II is a mixed structure of oxide and silicon formed at the projected range of the implanted oxygen (R_p). The thickness of the region is about 0.1μm. Region III contains the defect-rich zone extending into the substrate. Defects observed in this region include {113} defects and small stacking faults (SFs).

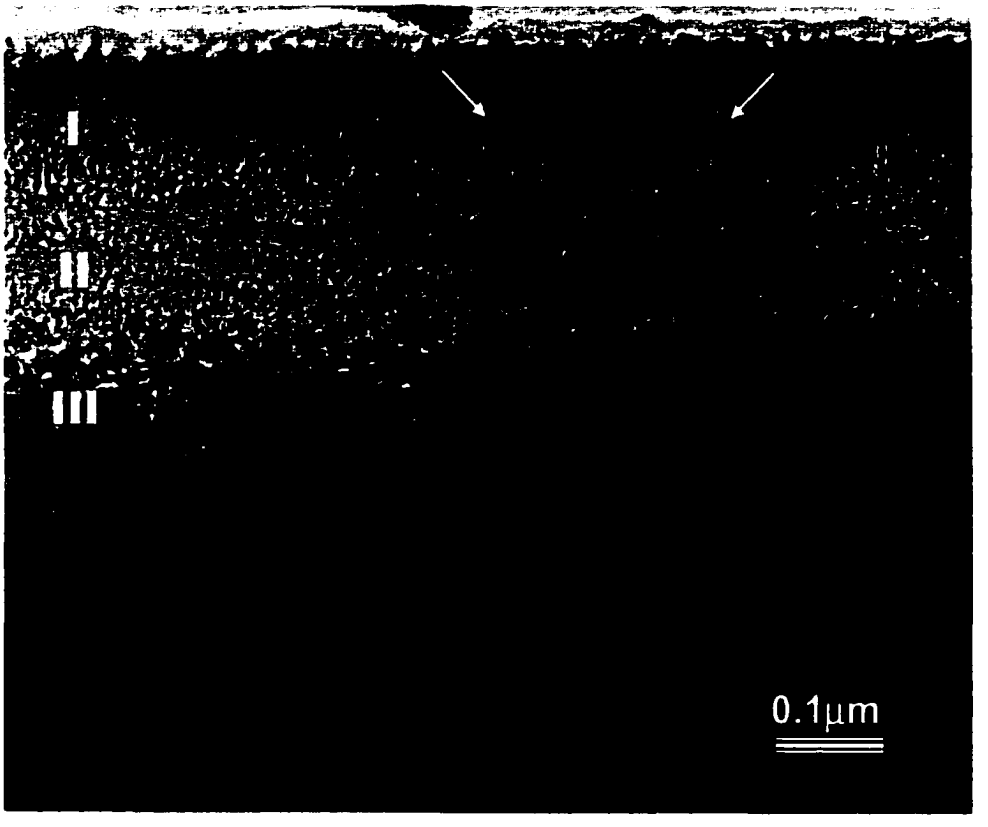

Figure 5.1 Microstructure of SIMOX sample implanted at 65 keV, 500°C with a dose of $4.5 \times 10^{17}/cm^2$. Arrows indicate MFDs.

Figure 5.2 shows the microstructure of the sample annealed at 900°C for 2 hours. The microstructure of the sample is not significantly different from that of the as-implanted sample, except in region III where the damage extent into the substrate was slightly reduced. This possibly indicates that the thermal energy at 900°C is not high enough to induce mass redistribution of oxygen and silicon interstitials required to bring about major structural changes.

Figure 5.3 shows the microstructure of the sample annealed at 1100°C for two hours. Significant changes have occurred in the microstructure compared to that of the as-implanted sample. The rough surface in the as-implanted sample has smoothened considerably due to surface regrowth. Larger but fewer oxygen precipitates can be observed near the interface in region I, which is an evident of appreciable ripening of the precipitates which were stable at this annealing temperature. No MFD was observed in the sample, which suggests that they have all been removed, probably by stress relief at elevated temperatures. Region II has also undergone some structural changes. The oxide striations in the structure have grown larger and become better defined than in the as-implanted sample. It can also be seen that the vertical extent of region III has decreased considerably due to thermal assisted recovery of the crystalline order.

Figure 5.4 shows the microstructure of the sample annealed at 1200°C for 2 hours. A complete SIMOX structure has not formed but there is a dramatic change in the microstructure compared to that of the as-implanted sample. Region III (the defect-rich zone) has fully recovered and relatively sharp interface has formed. The top Si layer and the developing BOX layer have become more distinctive. The surface of the sample has

smoothened to a large extent. The implantation-induced crystalline damage was restored considerably in the top Si layer. Oxygen precipitates in the top Si layer have ripened and coalesced into larger precipitates. The bottom of the layer shows a heavily jagged interface roughly the size of the precipitates. The silicon layers in the mixed structure have broken up in most areas into elongated hexagonal shapes. The BOX/substrate interface has fully developed but with incursions in some areas due to connections between the substrate and silicon inclusions.

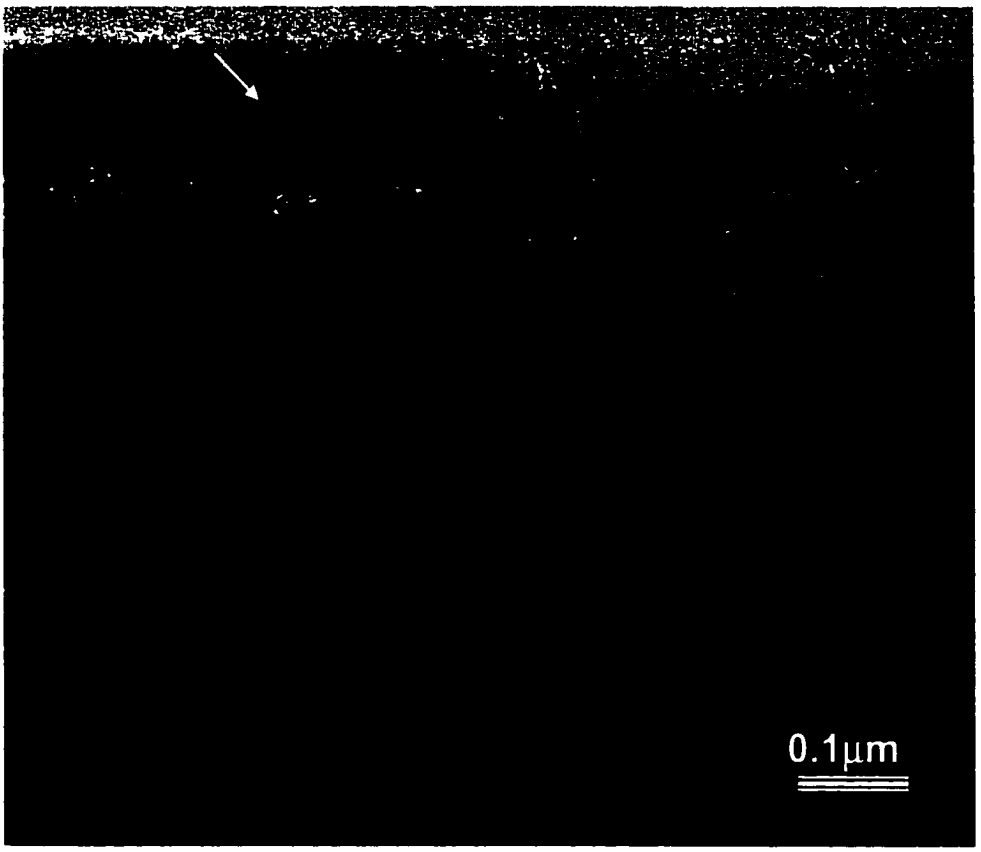

Figure 5.2 Microstructure of SIMOX sample implanted with a dose of $4.5 \times 10^{17}/cm^2$ and annealed at 900°C for 2 hours. Arrow indicates MFD.

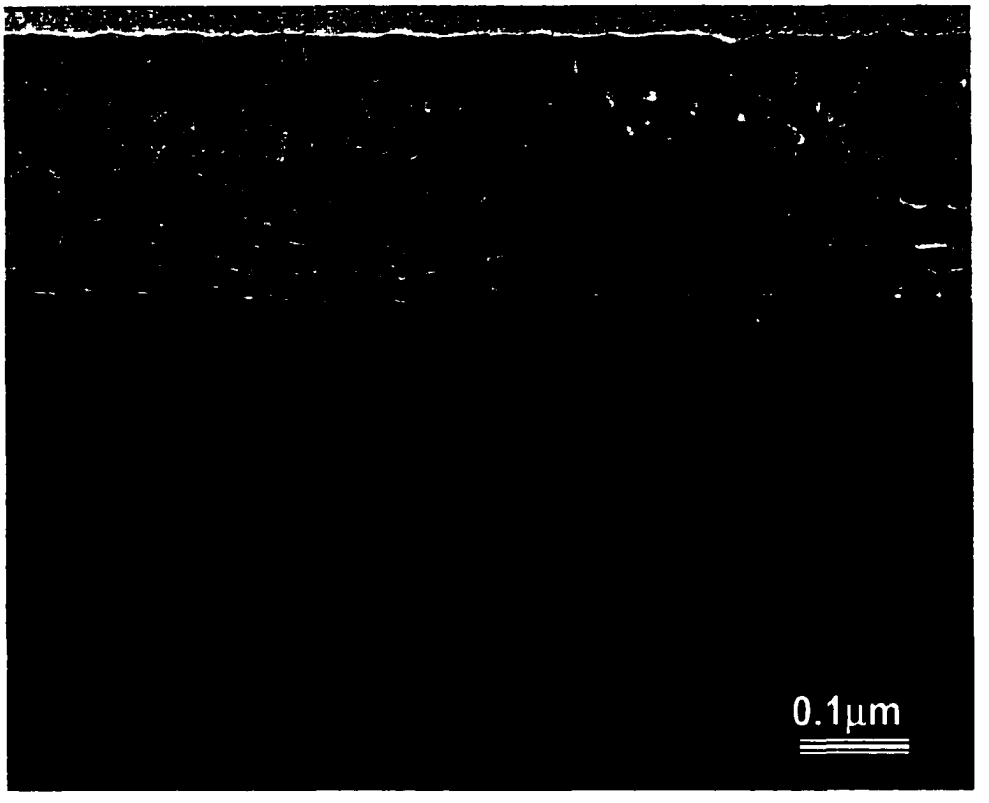

Figure 5.3 Microstructure of SIMOX sample implanted with a dose of $4.5x10^{17}/cm^2$ and annealed at 1100°C for 2 hours.

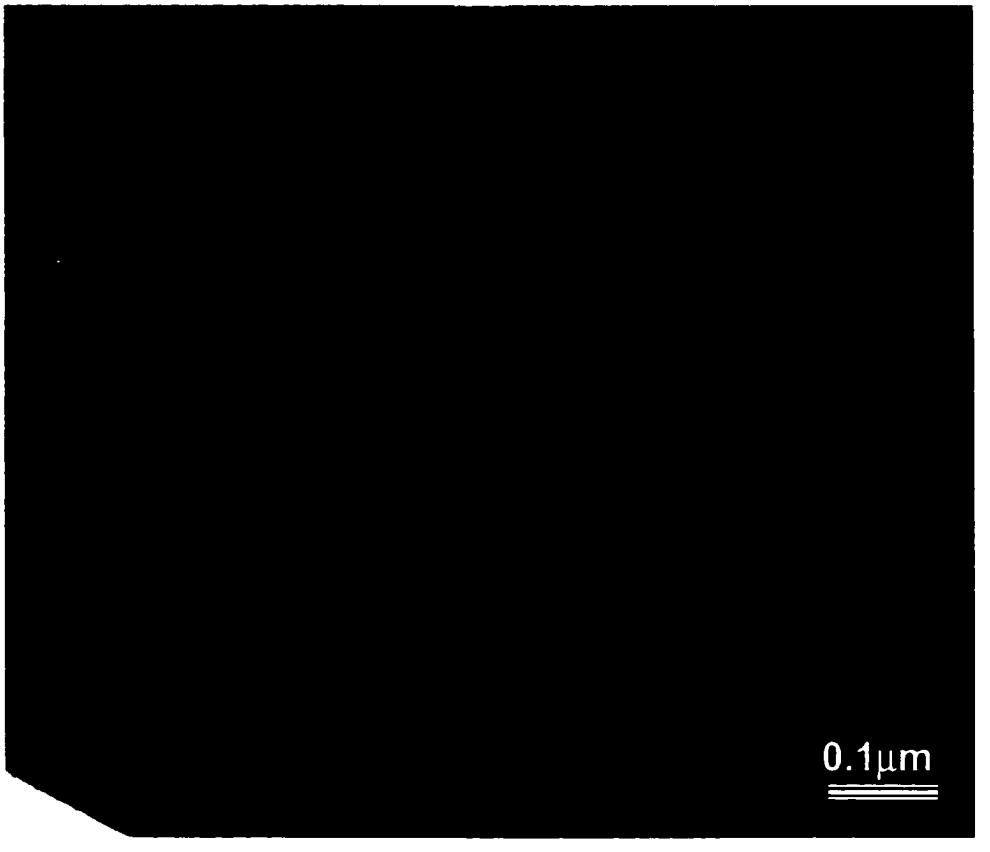

Figure 5.4 Microstructure of SIMOX sample implanted with a dose of $4.5 \times 10^{17}/cm^2$ and annealed at 1200°C for 2 hours.

5.2 Evolution of Surface Morphology

High-resolution transmission electron microscopy (HTREM) imaging was performed to study the atomic structure of the surface region during the intermediate-temperature annealing. All the samples were viewed in cross-section. Figure 5.5 shows a HRTEM image of the surface morphology of the as-implanted sample. It can be seen that the ion implantation creates a jagged surface of V-shaped grooves with edges oriented along <111> direction. The appearance of these preferentially oriented edges suggests that the ion sputtering rate appears to be faster in the direction normal to the <100> surface and slower along the <111> direction. The heavily damaged surface is due to excessive sputtering by lower-energy implantation.

Figure 5.6 shows a HRTEM image of the surface of the sample annealed at 900°C for two hours. It is not significantly different from that of the as-implanted sample. However, annealing at 1100°C for two hours significantly improved the surface morphology as shown in Figure 5.7. The surface improvement at this temperature is related to the surface regrowth with the driving force to minimize the surface energy by reduction in surface area.

Figure 5.8 shows HRTEM image of the surface morphology of the sample annealed at 1200°C for two hours. A remarkable improvement in the surface morphology occurred. The surface is generally flat within a few monolayers.

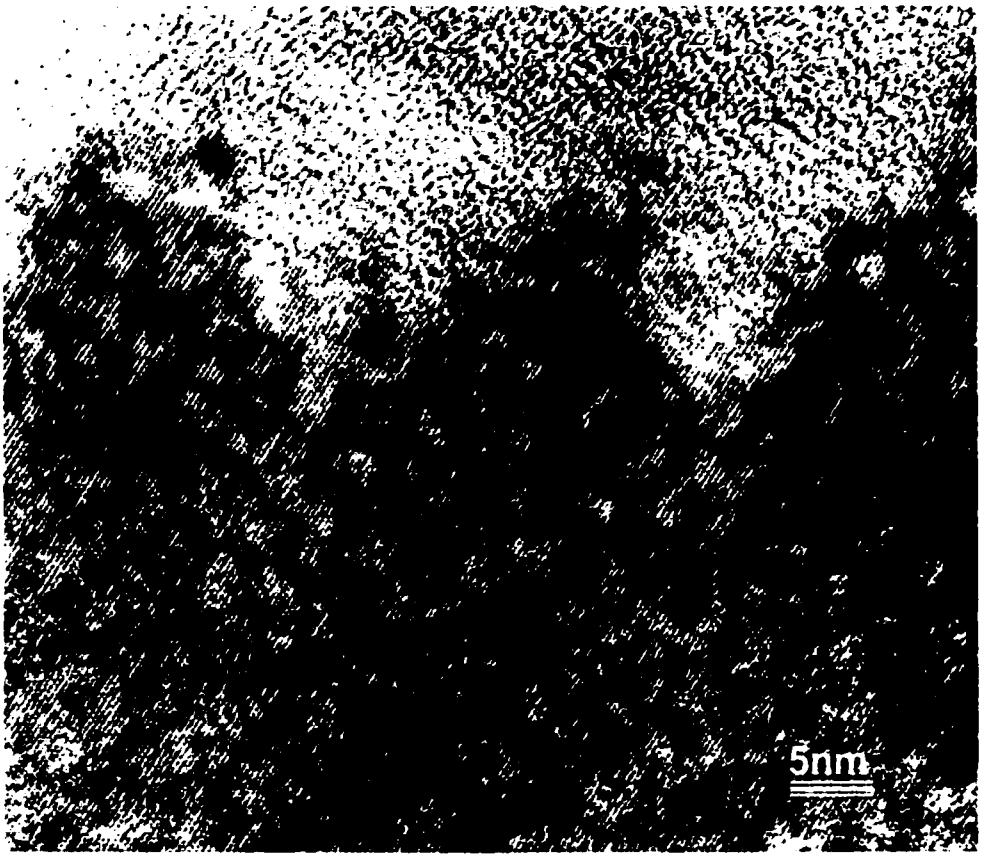

Figure 5.5 High-resolution TEM micrograph of the surface region of SIMOX sample implanted with a dose of $4.5 \times 10^{17}/cm^2$.

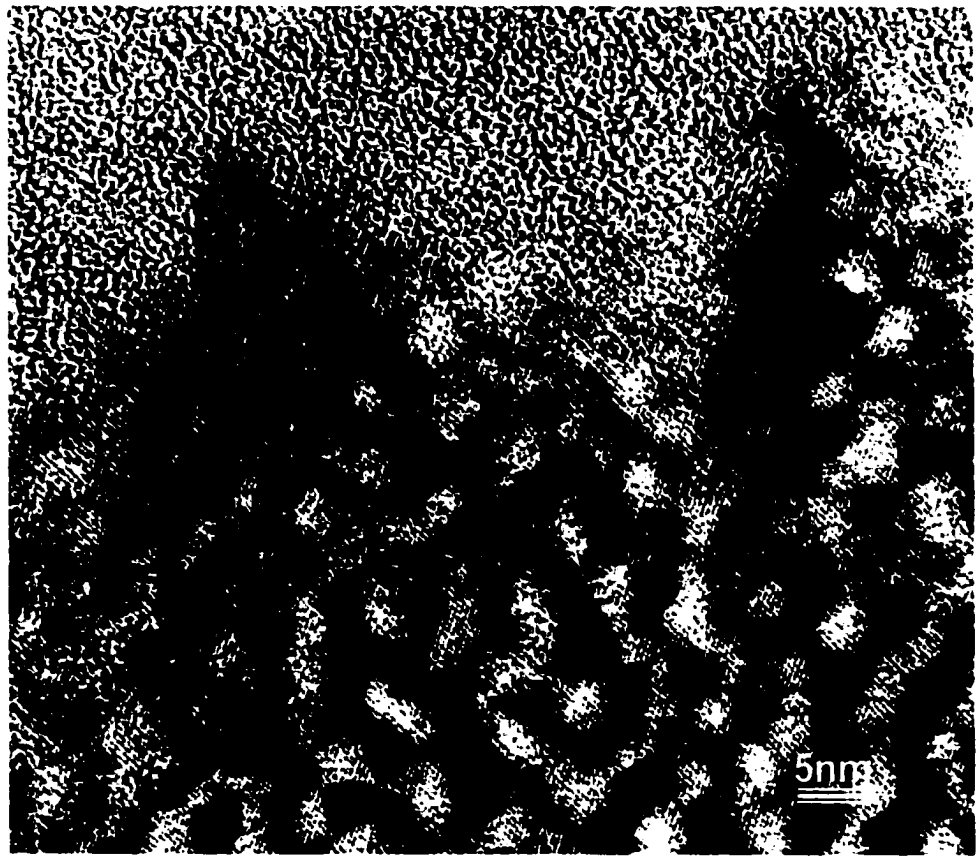

Figure 5.6 High-resolution TEM micrograph of the surface region of SIMOX sample implanted with a dose of $4.5 \times 10^{17}/cm^2$ and annealed at 900°C for 2 hours.

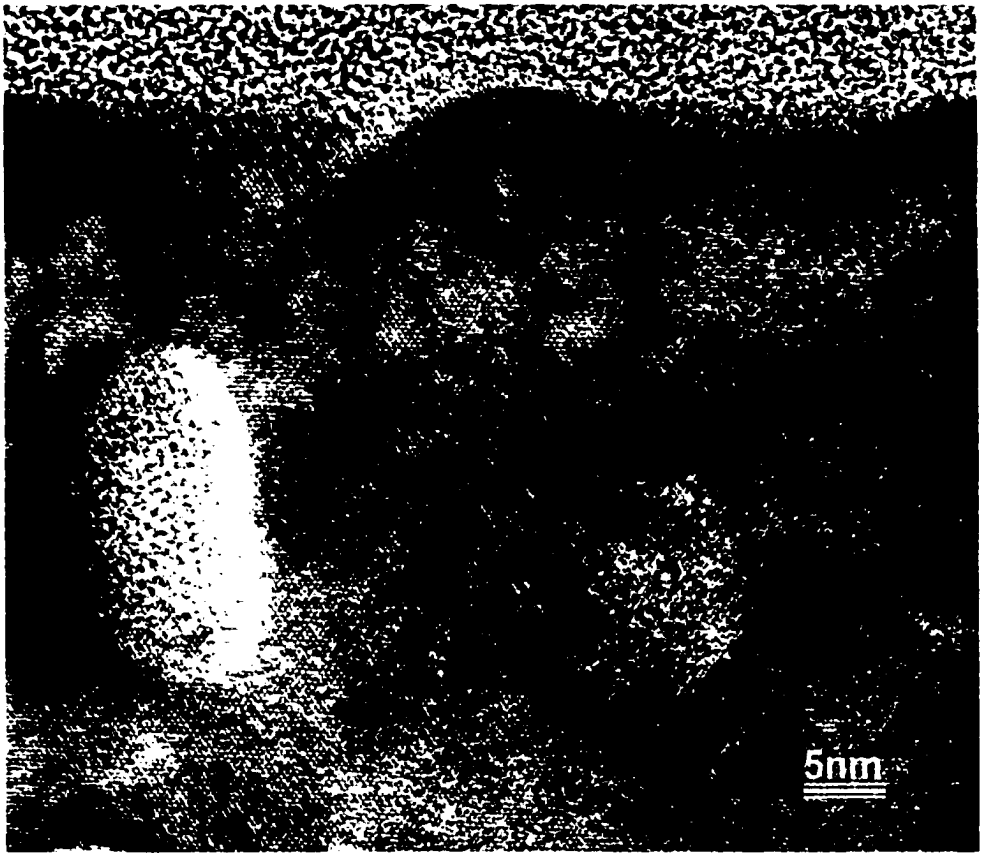

Figure 5.7 High-resolution TEM micrograph of the surface region of SIMOX sample implanted with a dose of $4.5 \times 10^{17}/cm^2$ and annealed at 1100°C for 2 hours.

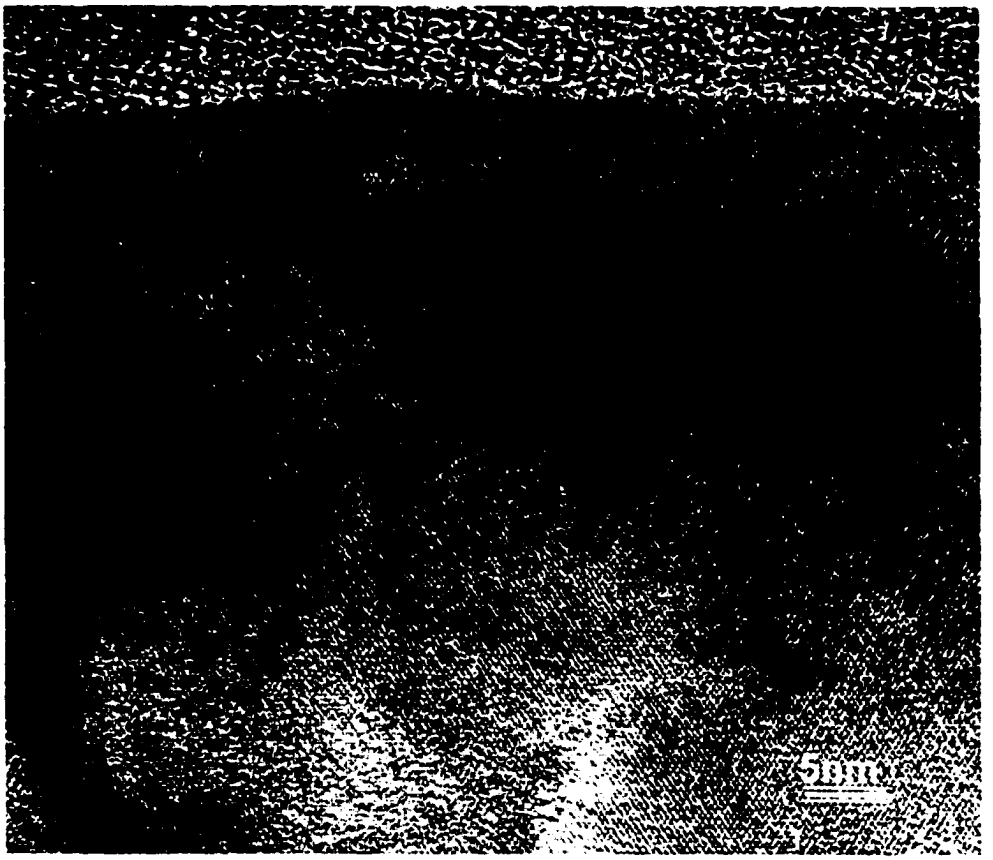

Figure 5.8 High-resolution TEM micrograph of the surface region of SIMOX sample implanted with a dose of $4.5 \times 10^{17}/cm^2$ and annealed at 1200°C for 2 hours.

5.3 AES analysis of oxygen distribution

AES analysis was performed to obtain oxygen depth profiles for the as-implanted and annealed samples. The objective of the analysis was to understand the oxygen redistribution process during the heating up of the as-implanted sample to final annealing temperature. Figure 5.9 shows AES depth profiles for the as-implanted and annealed samples including 1100°C for 2 hours, 1200°C for 2 hours and 1300°C for 6 hours. A skewed Gaussian distribution was observed for the as-implanted sample which was caused by significant backscattering of oxygen by silicon atoms. After annealing at 900°C for two hours (not shown here), no detectable change in the oxygen depth profile was observed. This shows that the oxygen redistribution process was not appreciable at 900°C. After annealing at 1100°C for 2 hours, limited oxygen redistribution occurred. It can be seen that the oxygen signal intensity dropped at the wings but increased slightly in the central part of the distribution. This shows that oxygen has diffused from the wings towards the striated region where the BOX layer formed.

The AES profile changed significantly after annealing at 1200°C for 2 hours. The oxygen concentrations at the wings of the profile dropped lower than the level of 1100°C sample and the central part rose considerably corresponding to the better-defined interfaces compared to the 1100°C sample. This indicates that more oxygen diffused from the top Si layer and from the damaged zone in the substrate into the BOX region. It can be seen that the slope of the profile corresponding to the lower interface is steeper than that of the upper one. This suggests that the oxygen gradient spread through wider region in the upper interface than in the lower corresponding to a better-defined lower

interface. The oxygen profile displays three peaks and two dips in the middle region of the profile. The peaks correspond to regions of high oxygen concentration while the dips represent the region with a high agglomeration of silicon islands. There was drastic oxygen redistribution during annealing at 1300°C for 6 hours. The oxygen signal intensity at the wings of the depth profile dropped insignificantly to the baseline level. The oxygen distribution has become more rectangular with the maximum levels approximately the stoichiometric SiO_2. The saddle region of the profile corresponds to the presence of a high density of silicon islands formed in the middle of the BOX layer.

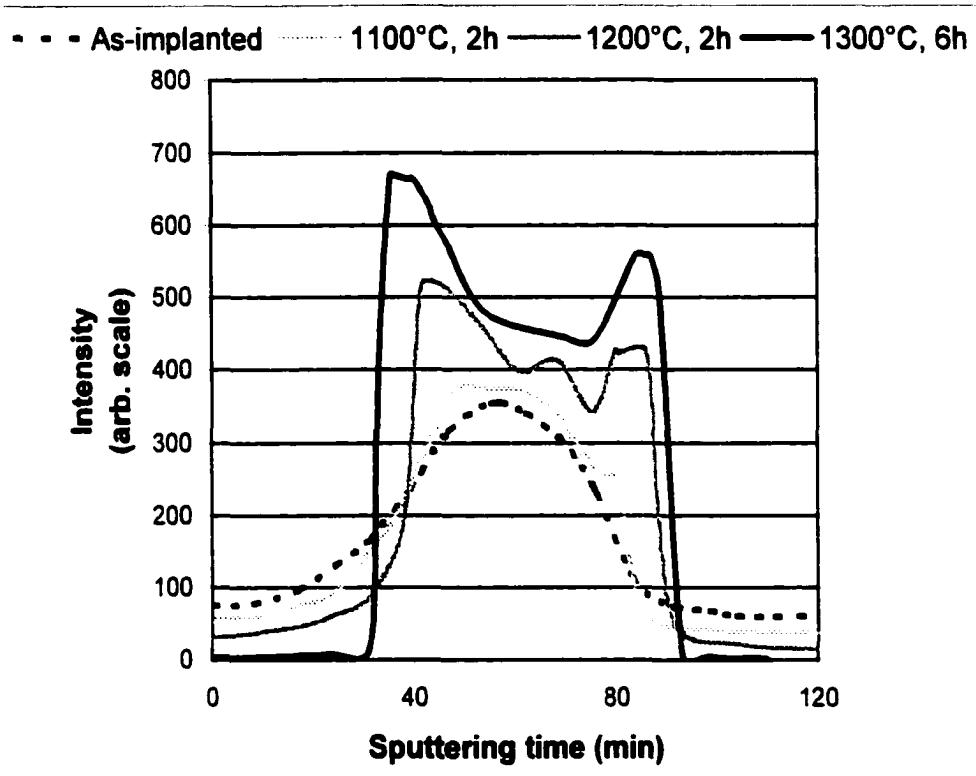

Figure 5.9 AES spectra from the as-implanted sample and samples annealed at various temperatures.

5.4 RBS analysis of crystal disorder

RBS analysis was performed to evaluate the extent of damage in the as-implant and the annealed samples. The purpose of the analysis was to investigate the progress of the crystal recovery process at annealing temperatures. Figure 5.10 shows random and channeled RBS spectra of the as-implanted and the annealed samples. Regions I, II, and III marked in the figure correspond to the three distinct regions in the as-implanted sample marked in Figure 5.1. The random spectrum for each sample was found to be identical and so for the sake of simplicity only that of the as-implanted sample is shown in Figure 5.10. It can be seen that in regions I and III of the as-implanted sample, the yield of the channeled spectrum is lower than that of random spectrum. This means that silicon in both regions retained some degree of crystallinity during ion implantation. On the other hand, in region II in the as-implanted sample, the yield of channeled spectrum is almost the same as that of the random spectrum. It indicates that the crystallinity of this region was lost after ion implantation. As shown by TEM results, the loss of crystallinity in region II is due to the presence of the heavy implantation damage and oxygen precipitates. The crystalline long-range order of the top Si layer was determined using the crystal disorder parameter χ_{min}, the ratio of the channeled to random backscattering yield in the near surface region. The χ_{min} of the as-implanted sample was estimated at 35% indicating that a reasonably good crystallinity of Si layer was maintained during implantation despite an increased level of disorder in the near surface during lower-energy implantation.

During the subsequent annealing redistribution of oxygen and silicon atoms

occurred which changed the channeling characteristics of the annealed samples. The channeled spectrum of the annealed samples differed from that of as-implanted sample as can be seen from Figure 5.10 except the sample annealed at 900°C. This indicates that the significant recovery to restore the crystallinity of the sample occurred above 900°C. As the annealing temperature increased above 900°C, the backscattered yield of the channeled spectrum in region I and III decreased dramatically, with no change occurring in region II. The decrease in the channeled backscattering yield of region I and III with increasing annealing temperature can be attributed to the progressive increase in the damage recovery process and dissolution of oxygen precipitates in these regions. The extent of crystalline disorder in the top Si layer of the annealed samples was also determined. The disorder parameter χ_{min} for each annealed sample was obtained by the same approach used for the as-implanted sample. For the sample annealed at 900°C for two hours, χ_{min} was about the same as for the as-implanted sample (35%). It decreased to 25% and 12% after 2 hours of annealing at 1100°C and 1200°C, respectively, and then to 5% after annealing at 1300°C or 1350°C for 6 hours. Figure 5.11 shows the plot of χ_{min} as a function of annealing temperature. The value of χ_{min} obtained for the sample annealed at 1300°C (5%) is comparable to that of a virgin-single crystal silicon (4%) indicating the excellent crystalline quality of the top Si layer of the low-dose low-energy SIMOX after annealing at 1300°C.

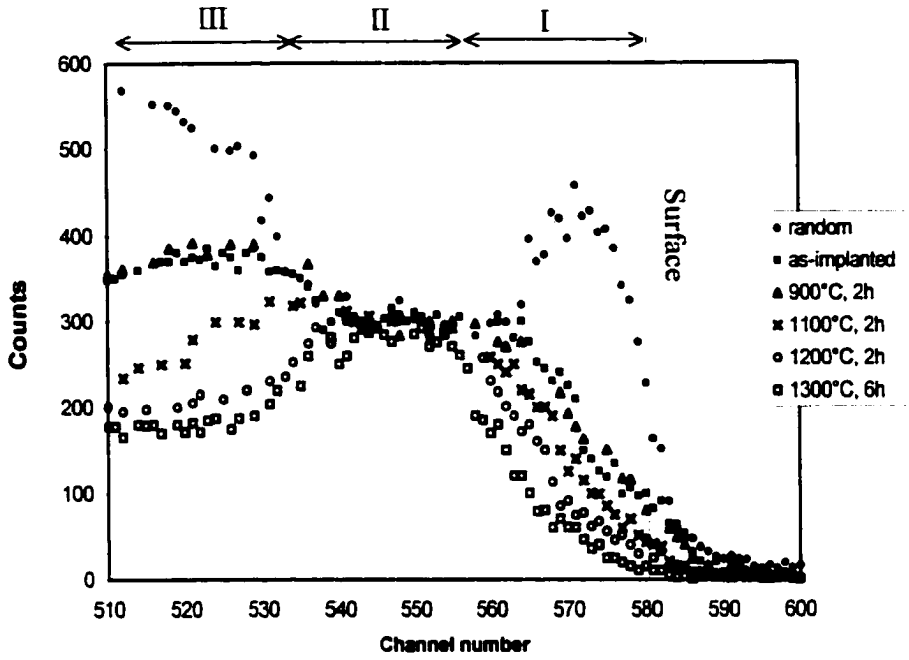

Figure 5.10 Random and channeled RBS spectra from the as-implanted sample and samples annealed at various temperatures.

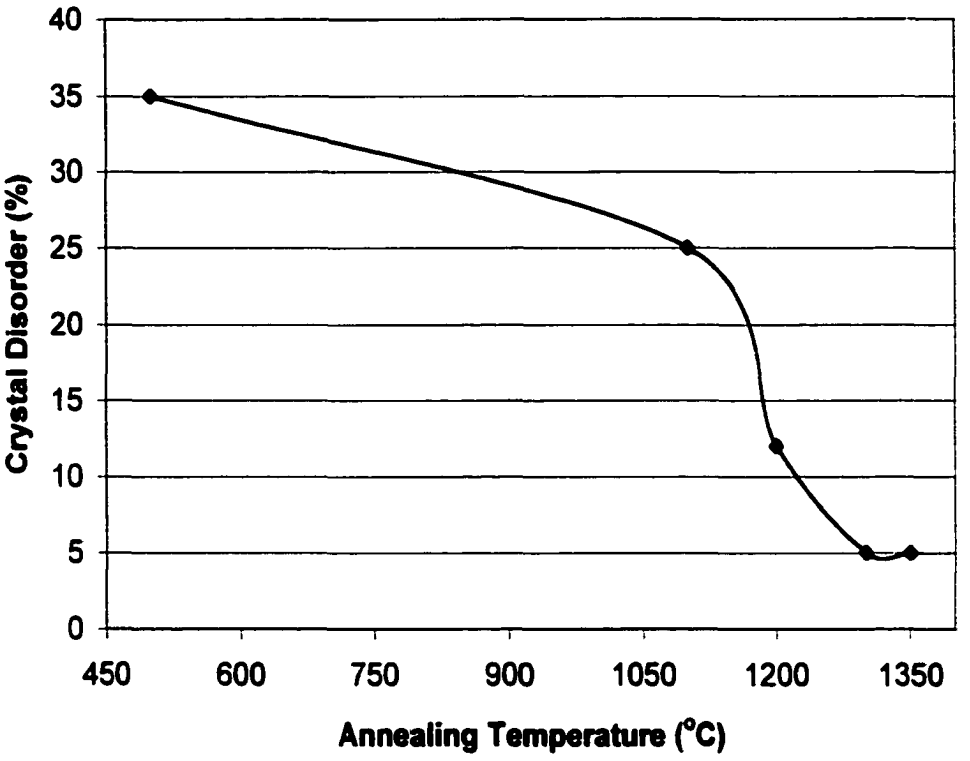

Figure 5.11 Crystal disorder, χ_{min}, as function of annealing temperature. Annealing temperature of 500°C indicated here refers to the wafer temperature during implantation.

5.5 Evolution of Oxygen Precipitates in the Top Si Layer

High-resolution transmission electron microscopy (HRTEM) imaging was performed to analyze oxygen precipitates in the top Si layers of the as-implanted sample and the intermediate-temperature annealed samples. The samples used for the analysis were implanted at 65 keV with dose of $4.5 \times 10^{17}/cm^2$ and annealed at 900°C, 1100°C and 1200°C each for 2 hours. The objective of the analysis was twofold: (i) to quantify oxygen precipitates in the as-implanted sample as well as the intermediate annealed samples, and (ii) use the acquired data to determine the kinetics underlying the precipitate growth and coarsening during annealing. Spatial quantities of interest were size distribution, number density, and volume fraction. The top Si layer of the as-implanted sample (region I in Figure 5.1) can be divided into two portions based on precipitate size distribution. The upper portion extends to about 60 nm below the sample surface and the lower portion is about 50 nm below the upper one. Figures 5.12 and 5.13 show HRTEM micrographs obtained from the upper and lower portions, respectively. It is clear from these images that the oxygen precipitates gradually increase in size with depth from the surface.

The size and depth distribution of the oxygen precipitates did not change significantly after annealing at 900°C for 2 hours (not shown here). However, from 1100°C and above growth and ripening occurred which resulted in a considerable increase in the precipitate size but a decrease in the density. Figures 5.14 and 5.15 shows HRTEM micrographs of the top Si layers of the samples annealed for 2 hours at 1100°C and 1200°C, respectively.

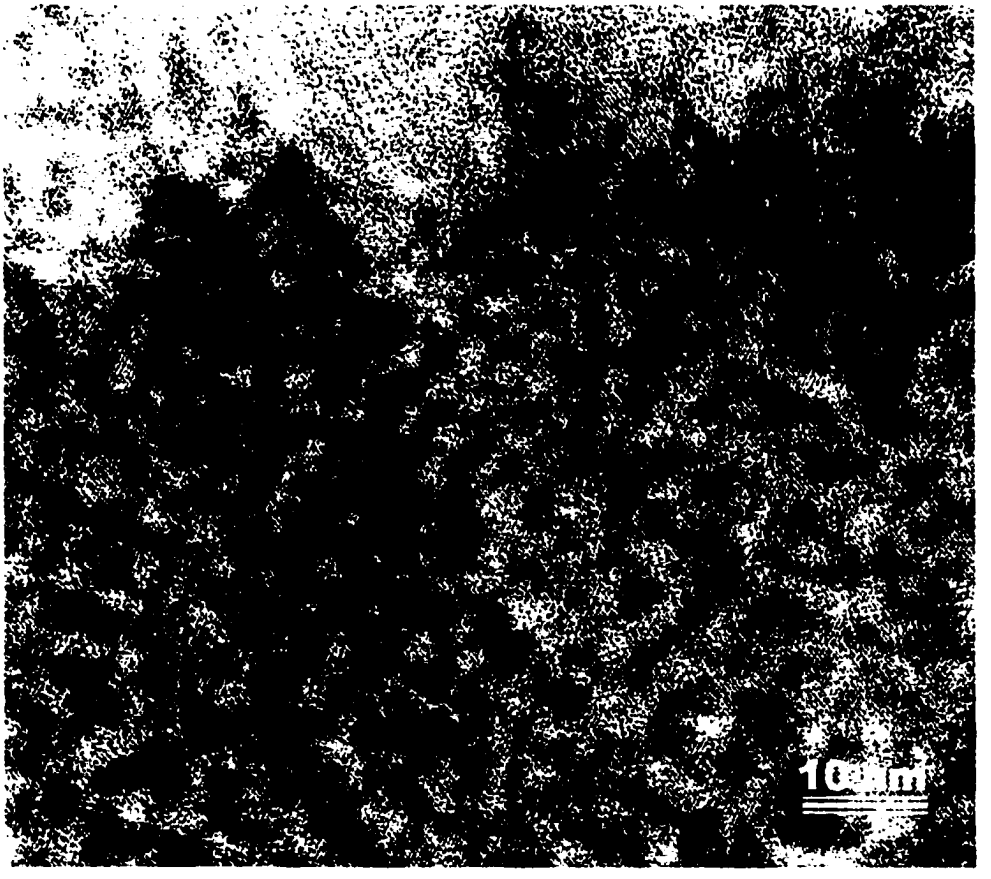

Figure 5.12 High-resolution TEM micrograph of oxygen precipitates in the upper portion of the top Si layer of the sample implanted with a dose of $4.5 \times 10^{17}/cm^2$.

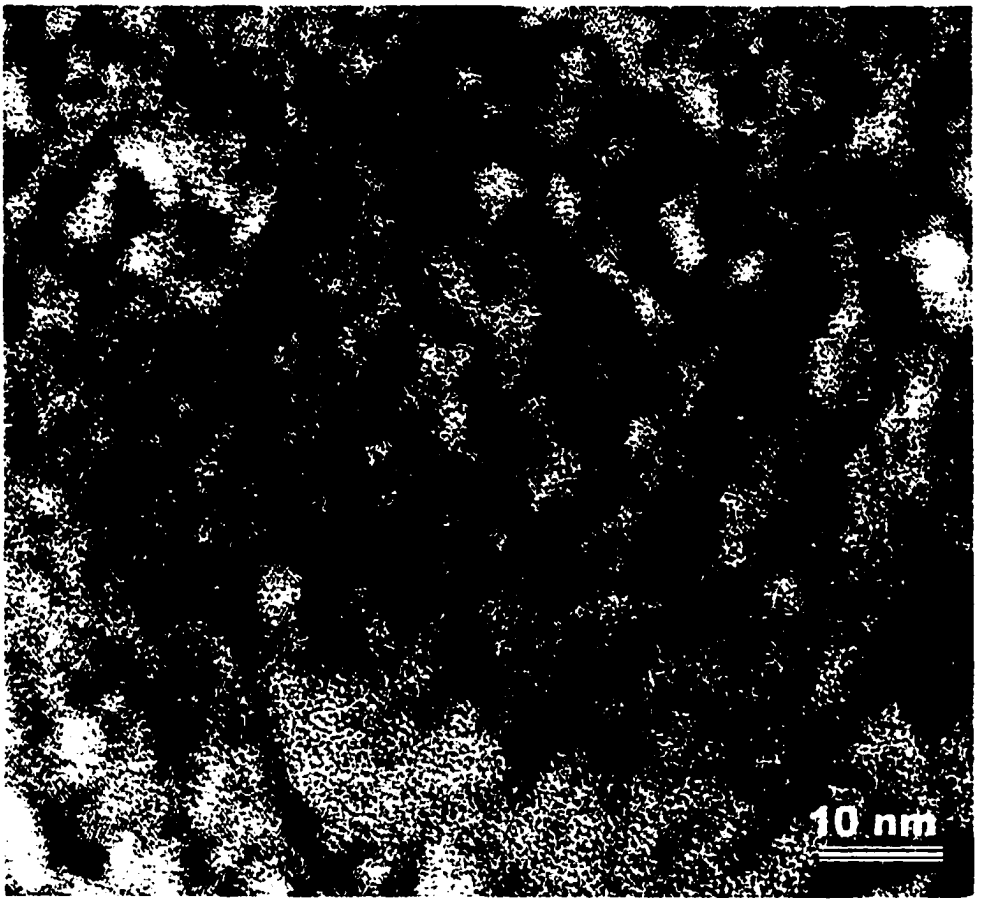

Figure 5.13 High-resolution TEM micrograph of oxygen precipitates in the lower portion of the top Si layer of the sample implanted with a dose of $4.5 \times 10^{17}/cm^2$.

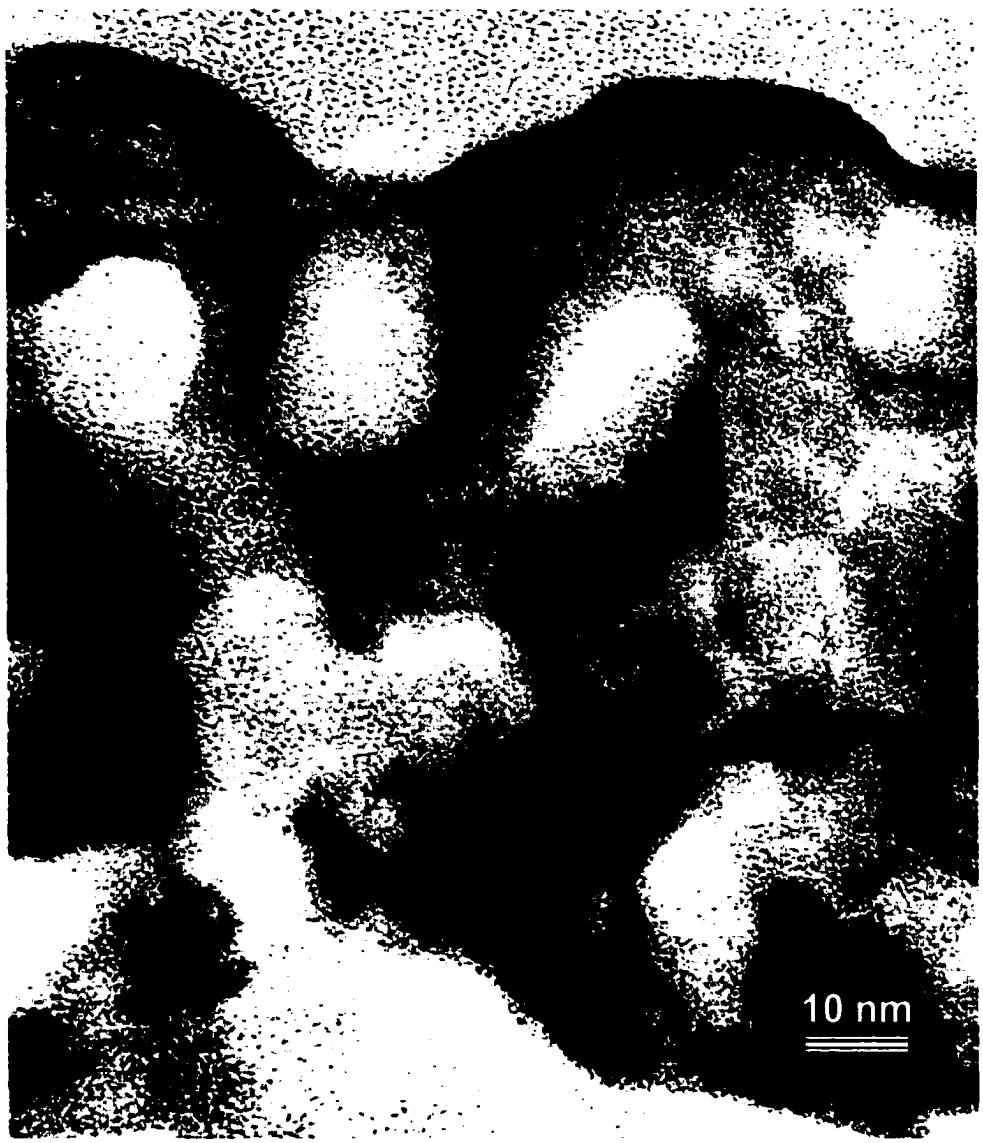

Figure 5.14 High-resolution TEM micrograph of oxygen precipitates in the top Si layer of the sample implanted with a dose of $4.5 \times 10^{17}/cm^2$ and annealed at 1100°C for 2 hours.

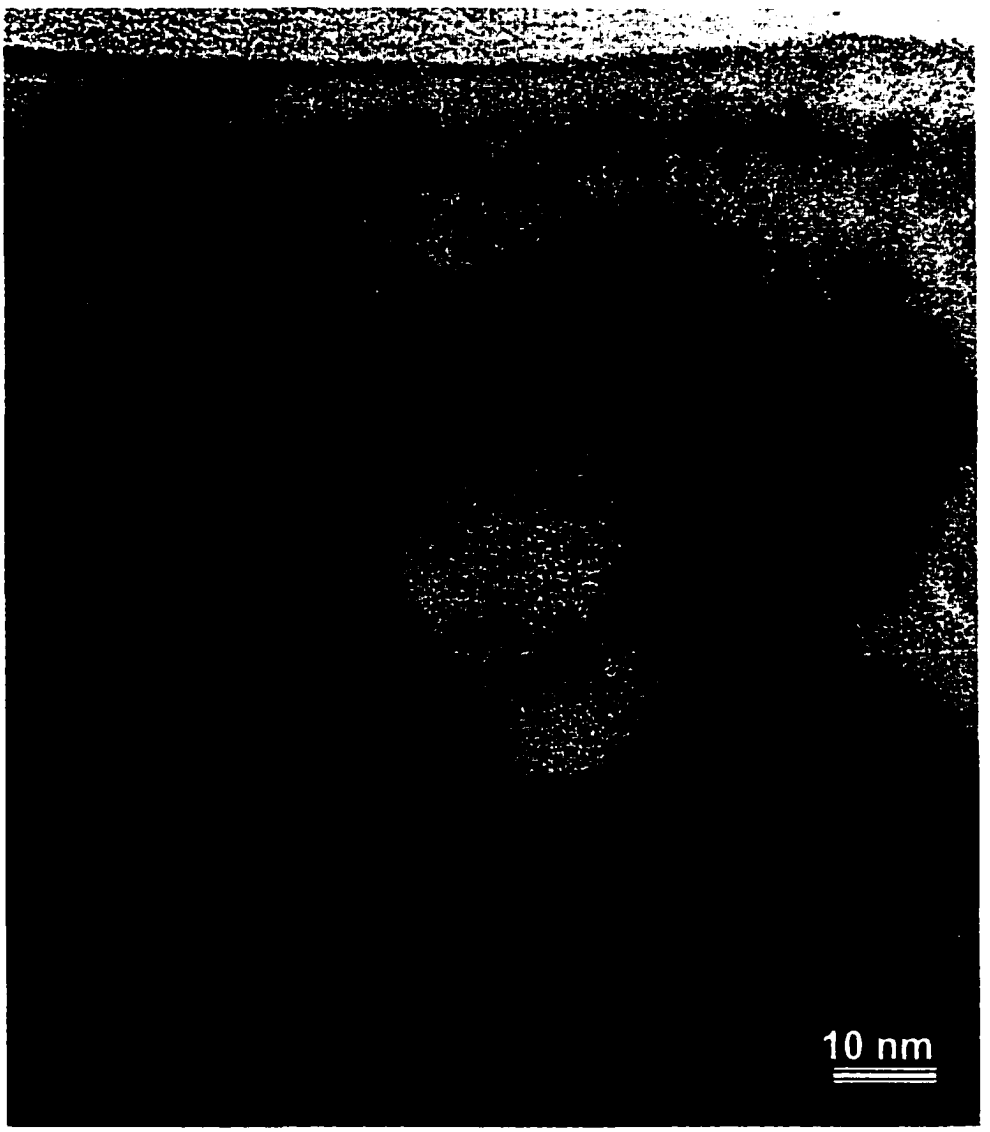

Figure 5.15 High-resolution TEM micrograph of oxygen precipitates in the top Si layer of the sample implanted with a dose of $4.5 \times 10^{17}/cm^2$ and annealed at 1200°C for 2 hours.

5.5.1 Precipitation Kinetics under Annealing

In order to understand the kinetical behavior of oxygen precipitates in the top Si layer during annealing, it requires the determination of the size, number density, and volume fraction of precipitates in the as-implanted and the intermediate-temperature annealed samples. These parameters allow evaluating the extent of precipitate ripening and oxygen out-diffusion in the top Si layer. Oxygen precipitates in the top Si layer of the as-implanted sample and the samples annealed at 900°C, 1100°C each for 2 hours were characterized for this study. To obtain the number density and volume fraction it requires the knowledge of the thickness of the region under analysis. For crystalline matrix, the thickness can be estimated through thickness fringes produced by the multi-beam imaging conditions. These fringes are the multi-beam equivalence of two-beam thickness fringes, i.e., they are formed by the propagation effects of Bloch waves excited in the crystal. For Si <110> multi-beam conditions, the fringe periodicity is ~27 nm [70]. All HRTEM images in this study were obtained over distances within the so-called flat region (first visible fringe), which corresponds to a thickness of ~13.5 nm. It can be seen from the HRTEM micrographs presented in Figures 5.11 to 5.14 that the precipitates vary from spherical to oblate spheroidal in shape. Therefore, the size of the precipitates is reported as the mean equivalent radius, $\bar{R}_e$. For non-spherical precipitates, this parameter is obtained based on equivalent radius. Given the mean size, $\bar{R}_e$ and the number density, N, the volume fraction, V_f, was estimated as:

$$V_f = \frac{4N\bar{R}_e^3}{3\pi} \qquad 5.1$$

The number of oxygen atoms within the precipitates in the as-implanted sample was deduced from the volume fraction and was obtained by:

$$N_{ox} = N_{ox}^{SiO_2} V_f \qquad 5.2$$

where $N_{ox}^{SiO_2} = 4.48 \times 10^{22}/cm^3$ is the oxygen atomic density of stoichiometric thermally grown SiO_2. Note that this analysis does not account for possible non-stoichiometric precipitation. The data obtained from the analysis are presented in Table 5.1. Calculated mean sizes at 900°C and 1100°C from a growth equation are given in the table. The derivation of the equation is shown below. The TEM results show that the mean size increases while the number density and volume fraction decrease with increasing temperature. These prove that that the precipitates undergo an Ostwald ripening mechanism. The decrease in volume fraction shows however that the ripening process is non-conservative since the total amount of oxygen during the growth process does not remain constant over time.

To test the accuracy of the TEM data, the area density of oxygen atoms in the as-implanted sample was calculated and compared to that obtained from SIMS profile for the as implanted sample. The value from the TEM data was obtained as follows. First, the number of oxygen atoms in the precipitates, N_{ox} was obtained by inserting into equation 5.2 the volume fraction of the precipitates, V_f (0.075) which gave $3.36 \times 10^{21}/cm^3$. By multiplying this value by the thickness of the layer within which the precipitates were found (13.5 nm), this corresponds to $4.5 \times 10^{15} atoms/cm^2$, which is the number of oxygen atoms within the precipitates by surface unit. The value from the SIMS profile was obtained by integrating the oxygen profile for the dose of $4.5 \times 10^{17}/cm^2$ in Figure 4.3 from

the surface to the depth of 13.5 nm, which gave 4.7×10^{15} atoms/cm^2. The comparison shows an excellent agreement which gives good confidence in the TEM data. The data was analyzed to determine the precipitate growth rate.

From classical nucleation theory [71], a nucleated, stable and spherical particle of radius R and solute concentration C_p embedded in a supersaturated matrix (of solute concentration C_s (t) far away from the precipitate) will grow at a rate of:

$$\frac{dR}{dt} = \frac{(C_s(t) - C_R)}{(C_p - C_R)} * \frac{D}{R} \qquad 5.3$$

where C_R is solute concentration at the interface. By assuming monodispersive system and $C_R = C_e = C_s$ ($t \rightarrow \infty$) the equilibrium concentration and $C_s = C_o$ the initial concentration, integrating equation 5.3 yields:

$$R^2(t) = \frac{2(C_o - C_e)}{(C_p - C_e)} * (Dt) \qquad 5.4$$

So far, there is only little experimental evidence for the existence of a precipitation stage during which particle growth follows strictly equation 5.4. In reality, as in our case one has to deal with precipitate size distribution f (R,t) rather than with precipitates of uniform size. In this case, C_R depends on R according to the Gibbs-Thomson equation

$$C_R = C_e \exp\{\frac{2\gamma V_m}{kT} * \frac{1}{R}\} \qquad 5.5$$

where V_m is molar volume; k is Boltzman's constant, and γ is interfacial energy. The growth rate is still given by equation 5.3. However, in a ripening regime, by virtue of equation 5.5, the precipitates grow ($dR/dt > 0$) or dissolved depending on whether $R > R^*$ or $R < R^*$ with:

$$R^{*} = \frac{2\gamma V_m}{kT} \qquad 5.6$$

The time evolution of the precipitate size distribution (f (R,t) satisfies continuity equation [71]:

$$\frac{\partial f}{\partial t} + \frac{\partial}{\partial R}\{f * \frac{\partial R}{\partial t}\} = 0 \qquad 5.7$$

Equations 5.3 and 5.7 form the basis of the well-known LSW (Lifshitz, Slyozov and Wagner) theory of Ostwald ripening. To solve these equations of motions analytically, it requires certain assumptions. If it is assume that the volume fraction of precipitates, V_f is close to zero which we can in our case, then in the asymptotic limit ($t \rightarrow \infty$) the theory yields for diffusion controlled ripening this expression for time evolution of the mean radius of the precipitates [72].

$$R^3_m = Kt + R^3_o \qquad 5.8$$

with K = (C/T)exp (-Ea/kT) the coarsening rate, Ea is the activation energy for precipitate growth, R_o is the mean precipitate radius at the onset (t =0), and C =1.63x10^5 nmK. Using the following data E_a = 1 eV [73], R_o = 1.8 nm from TEM measurement and t = 2 hours (7200s) equation 5.8 was tested at 900°C and 1100°C which yielded 3.8 nm and 5.7 nm, respectively for the mean precipitate size.

Table 5.1 Mean radius, number density, and volume fraction of oxygen precipitates in the top Si layer at various annealing temperatures.

Annealing Temperature °C	Holding Time hrs	Mean Radius Measured nm	Standard Deviation	Mean Radius Calculated nm	Number Density /cm^3	Volume Fraction
500	0	1.8	1	-	3.9×10^{18}	0.075
900	2	2.5	1.6	3.8	2.4×10^{18}	0.058
1100	2	7.5	2.9	5.7	9.8×10^{14}	0.007

CHAPTER 6

EFFECT OF ANNEALING CONDITIONS

High-temperature annealing is the final step in the processing of SIMOX material. The purpose of this step is to transform the heavily damaged as-implanted material into a device quality substrate. The set of annealing conditions applied is determined by the state of the material prior to annealing and is generally performed between 1300°C and 1350°C for a duration of 4 to 6 hours under Ar + O_2 ambient. The principal parameters are temperature, time, and the ambient. The work described in this chapter was performed with objective of studying effects of annealing temperature and surface capping on the microstructure of ultra-thin SIMOX samples implanted at 65 keV.

6.1 Effect of Final Annealing Temperature

The effect of final annealing temperature was evaluated at temperatures of 1300°C and 1350°C. Each annealing cycle was performed under Ar + O_2 ambient for 6 hours. The wafers used were implanted at 65 keV with a dose of $4.5 \times 10^{17}/cm^2$. Figure 6.1 shows cross-sectional TEM micrograph of a sample annealed at 1300°C for 6 hours. A complete SIMOX structure has formed with well-defined layers. The top Si layer and The BOX layer were measured and are approximately 50 nm and 140 nm. There was no evidence for the presence of oxygen precipitates in the top Si layer, which indicates that the precipitation process towards the formation of the BOX layer was completed at this temperature. The figure shows that numerous silicon islands are present in the BOX layer

which can be related to a large amount of silicon atoms contained in the mixed structure formed during the implantation step.

Figure 6.2 shows cross-sectional TEM micrograph of the sample annealed at 1350°C for 6 hours. It is clear from the figure that the microstructure of this sample is not significantly different from that of the 1300°C sample. Channeling RBS analysis was performed to evaluate the cystallinity of the top Si layer of the sample at the two annealing temperature. The results are presented in Figure 6.3. The crystal disorder parameter; χ_{min} obtained was the same (5%) for each sample. This suggests that under these implantation conditions, a good quality top Si layer can be obtained by annealing at either 1300°C or 1350°C.

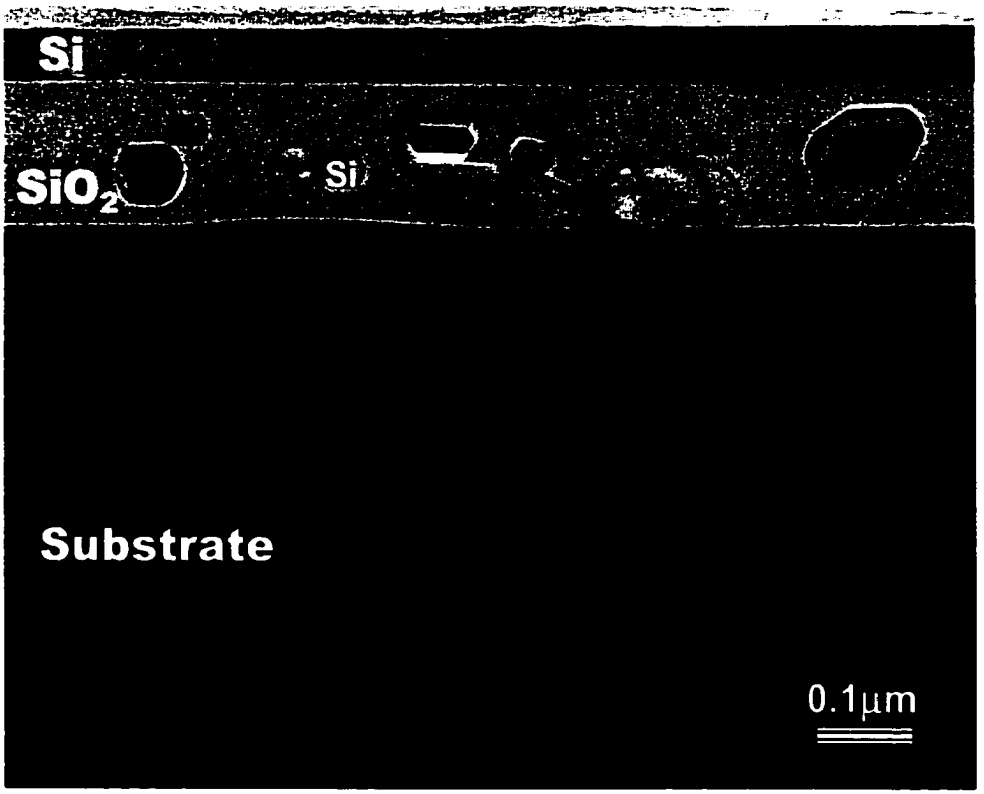

Figure 6.1 Cross-sectional TEM micrograph of SIMOX sample implanted with a dose of $4.5 \times 10^{17}/cm^2$ and annealed at 1300°C for 6 hours.

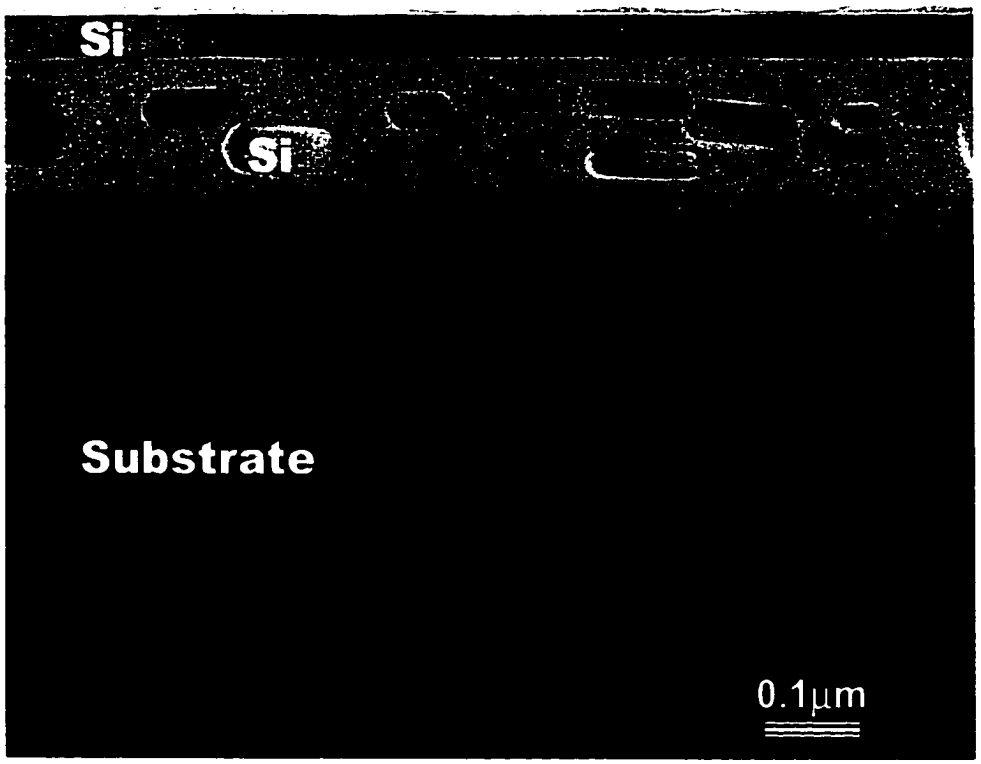

Figure 6.2 Cross-sectional TEM micrograph of SIMOX sample implanted with a dose of $4.5 \times 10^{17}/cm^2$ and annealed at 1350°C for 6 hours.

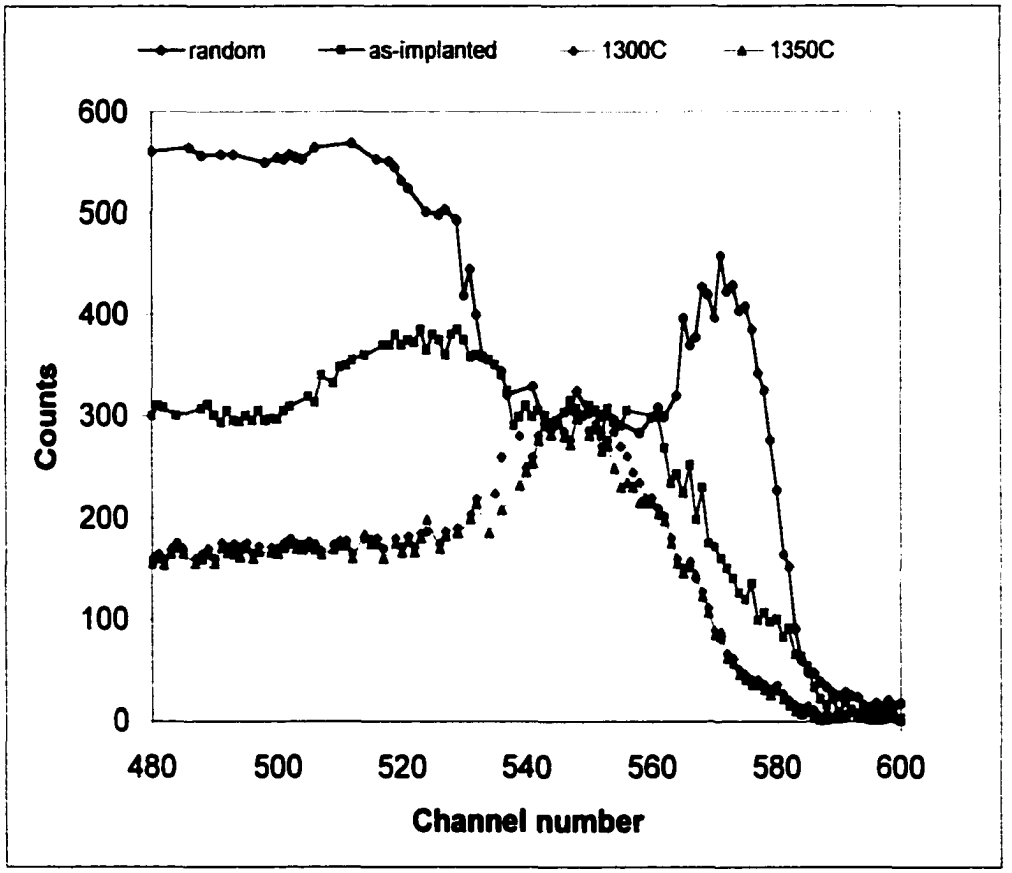

Figure 6.3 Random and channeled RBS spectra from as-implanted sample with a dose of $4.5 \times 10^{17}/cm^2$ and samples annealed at two final temperatures.

6.2 Effect of Surface Capping

Capping the sample surface to prevent external thermal oxidation during annealing is important to preserve the thickness of the top Si layer. This is particularly critical for the ultra-thin SIMOX produced by the low-dose low-energy process. However, the surface capping also affects the formation of the BOX layer.

The effect of surface capping during annealing was studied using two sets of samples. One set of samples with doses of 1.5, 2.0, 2.5, 3.0, 3.5, 4.0, 5.0, and $7.0x10^{17}/cm^2$ was annealed for 4 hours at 1350°C in Ar + 0.5% O_2 without a protective cap on the surface of the sample. The second set also with the same doses as the first set was annealed for 6 hours at 1350°C in Ar + 5% O_2 covered with a protective cap on the surface of the sample. The protective cap was formed by decomposition of TetraEthyl OrthoSilicate (TEOS) to prevent the top Si layer from being oxidized. The 5% O_2 used in the capping ambient was the minimum required to prevent decomposition of the TEOS material during annealing.

Figures 6.4 to 6.11 show TEM micrographs of the above samples annealed with (a) no protective cap and (b) with protective cap on the sample surface. At the lowest dose ($1.5x10^{17}/cm^2$), the BOX layer does not form continuously under both annealing conditions but consists of a collection of disjointed SiO_2 precipitates. The precipitates are, however, longer in size and less isolated in the uncapped sample (Figure 6.4a) than in the capped sample (Figure 6.4b). This indicates that the extra oxygen from the ambient caused a lateral growth of the oxide precipitates in the uncapped sample. At the next lowest dose ($2.0x10^{17}/cm^2$), the BOX layer forms continuously in the uncapped sample

(Figure 6.5a) but not in the capped sample (Figure 6.5b). The BOX layer starts to form continuously in the capped samples at the dose of $2.5 \times 10^{17}/cm^2$ (Figure 6.6b).

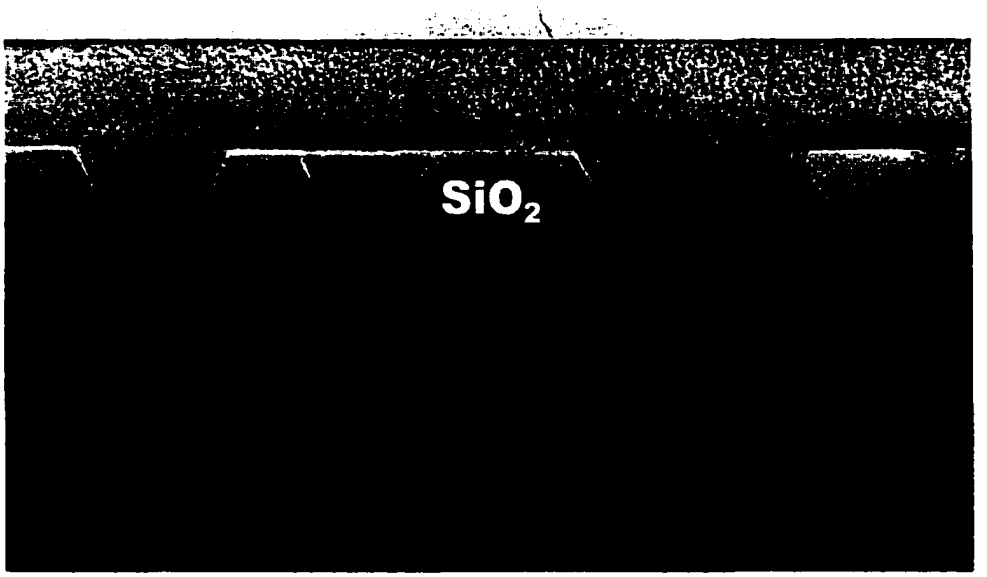

(a) Uncapped

(b) Capped

Figure 6.4 TEM micrographs of SIMOX samples implanted with a dose of $1.5x10^{17}/cm^2$ and annealed at 1350°C (a) without and (b) with protective cap.

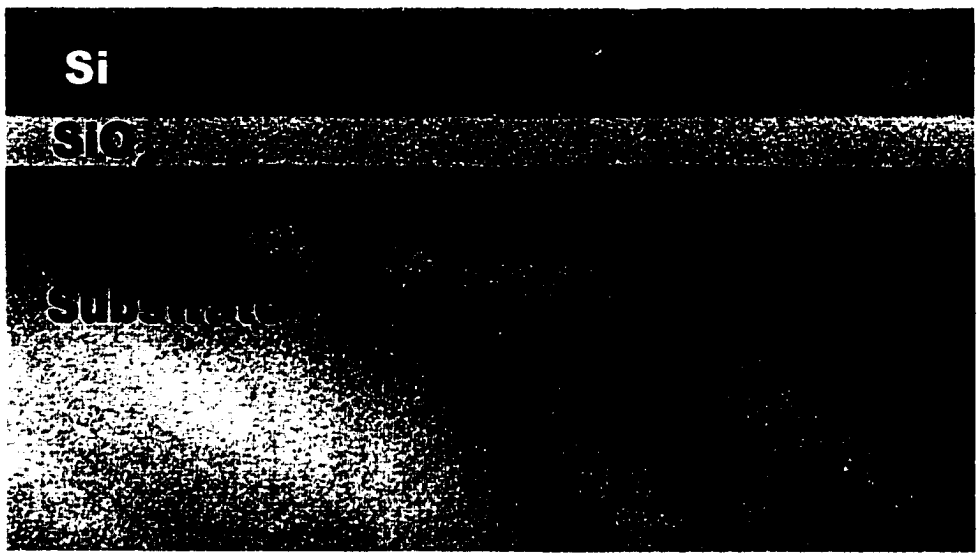

(a) Uncapped

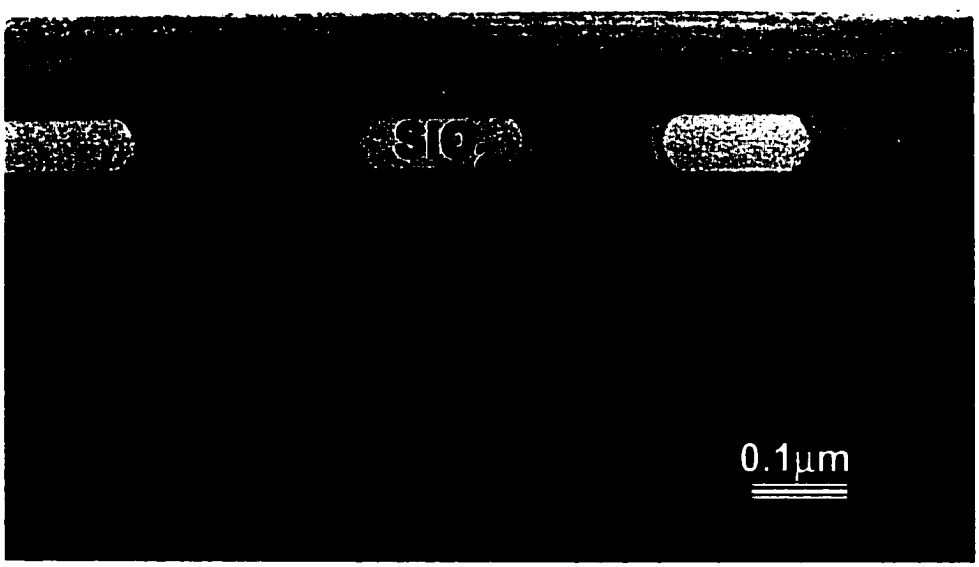

(b) Capped

Figure 6.5 TEM micrographs of SIMOX samples implanted with a dose of $2.0 \times 10^{17}/cm^2$ and annealed at 1350°C (a) without and (b) with protective cap.

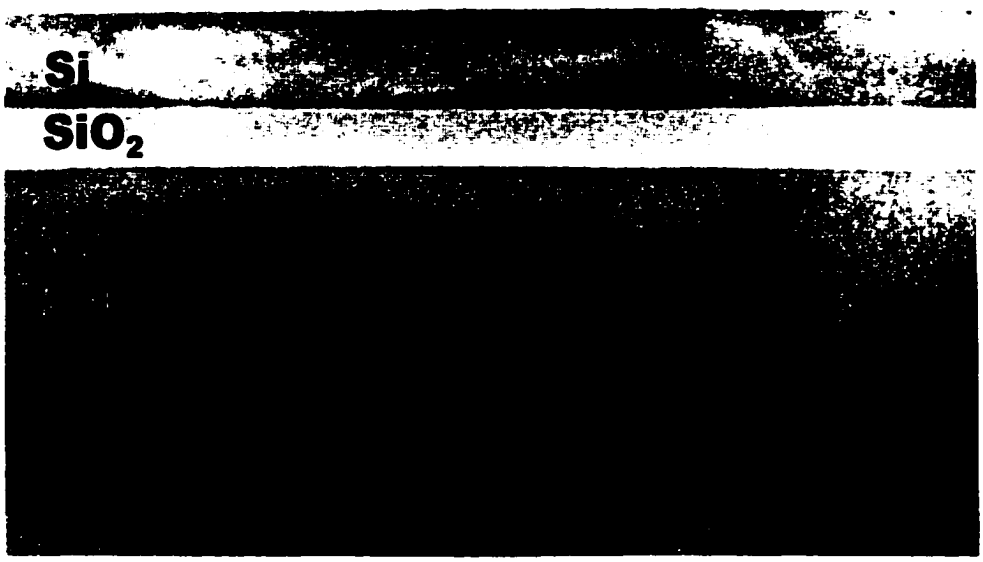

(a) Uncapped

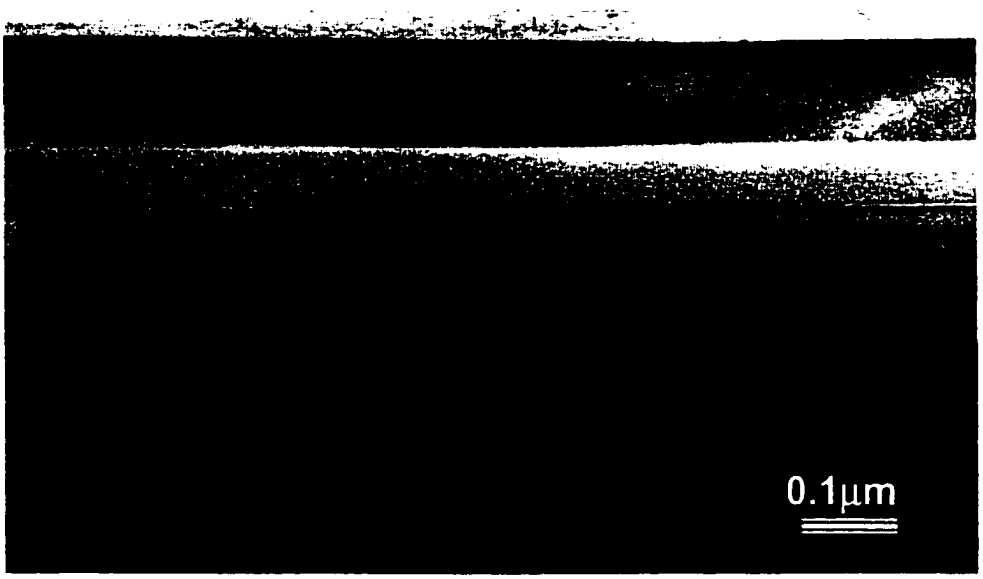

(b) Capped

Figure 6.6 TEM micrographs of SIMOX samples implanted with a dose of $2.5 \times 10^{17}/cm^2$ and annealed at 1350°C (a) without and (b) with protective cap.

At doses greater than $2.5x10^{17}cm^2$ in both sets of samples, a continuous BOX layer forms but it contains numerous Si islands as shown in Figure 6.7 to 6.11. The uncapped samples (Figure 6.7a-6.11a) show slightly lower density of silicon islands than the capped samples (Figure 6.7b-6.11b) because the extra oxygen diffused in from the ambient helps to oxidize some of the entrapped Si interstitials reducing the number of islands in the BOX layer. It is clear from these TEM results that for an implantation energy of 65keV, a dose range of 2.0 to $2.5x10^{17}cm^2$ is an optimum dose window where a continuous BOX layer forms without Si islands.

The thicknesses of the top Si and BOX layers in both capped and uncapped samples were determined through TEM measurements, which are presented in Table 6.1. For both sets of samples the thickness of the top Si layer tends to decrease with increasing implant dose since the BOX layer grows at the expense of the top Si layer. However, the top Si layer of the uncapped sample is thinner than that of the capped sample because a portion (~17 nm) of the layer is consumed by thermal oxidation. The measurements performed on the BOX layer showed no significant difference in thickness between the capped and uncapped sample. The effect of surface capping on the dimension of both layers is shown schematically in Figure 6.12.

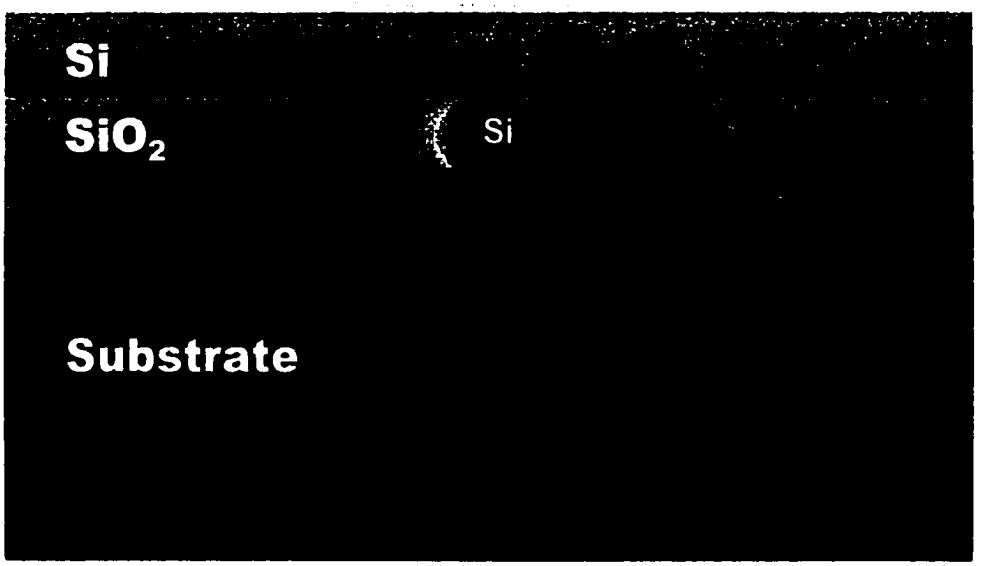

(a) Uncapped

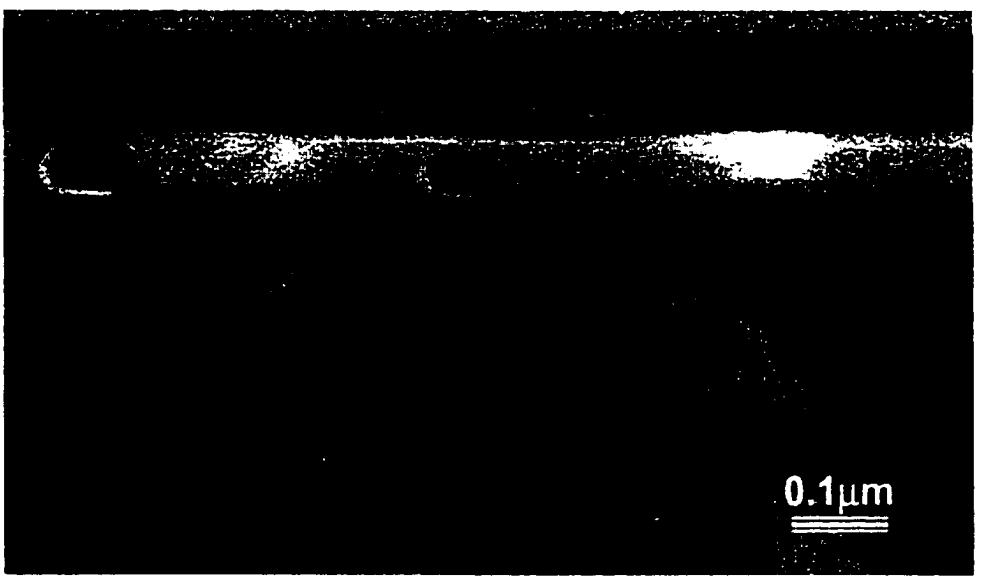

(b) Capped

Figure 6.7 TEM micrographs of SIMOX samples implanted with a dose of $3.0 \times 10^{17}/cm^2$ and annealed at 1350°C (a) without and (b) with protective cap.

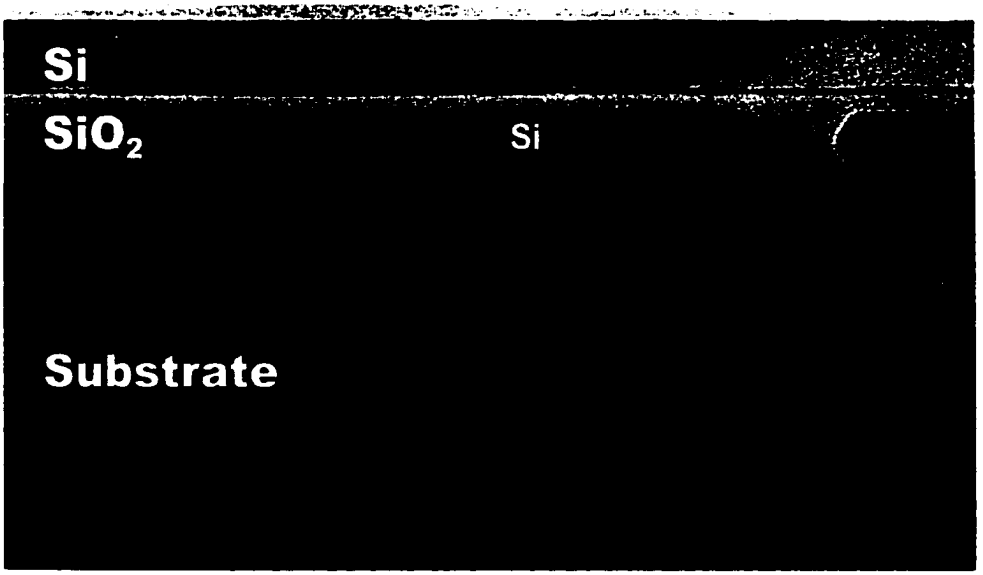

(a) Uncapped

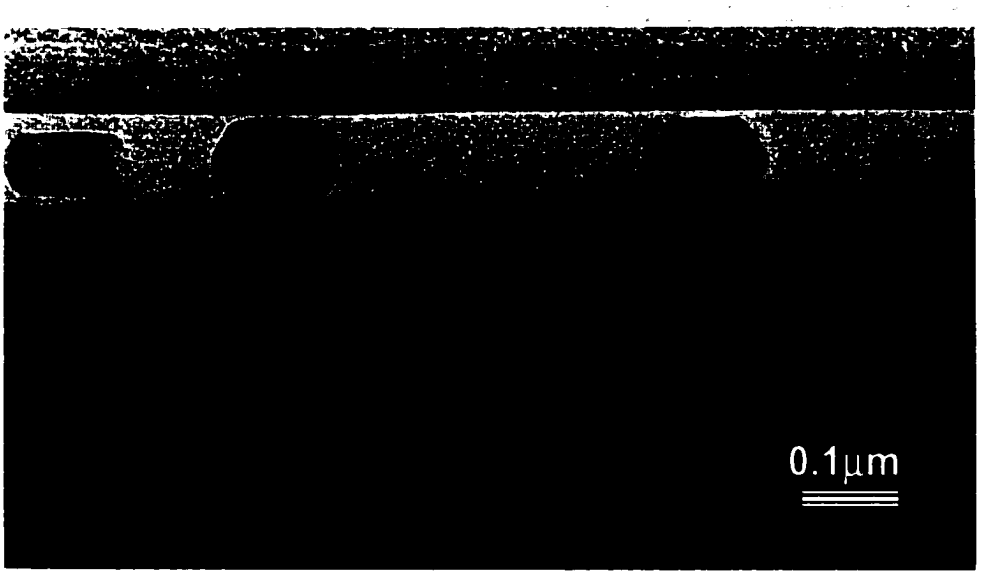

(b) Capped

Figure 6.8 TEM micrographs of SIMOX samples implanted with a dose of $3.5x10^{17}/cm^2$ and annealed at 1350°C (a) without and (b) with protective cap.

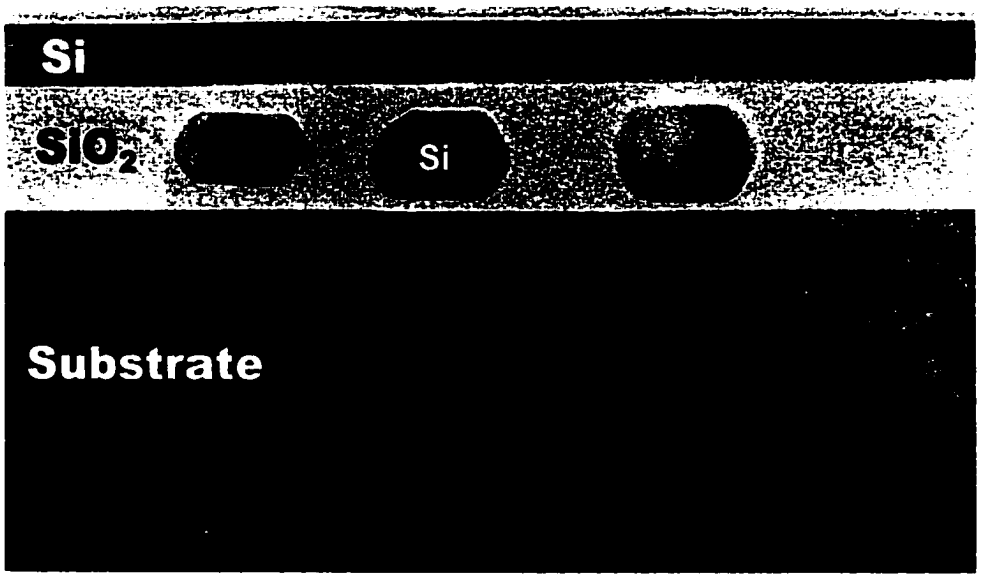

(a) Uncapped

(b) Capped

Figure 6.9 TEM micrographs of SIMOX samples implanted with a dose of $4.0 \times 10^{17}/cm^2$ and annealed at 1350°C (a) without and (b) with protective cap.

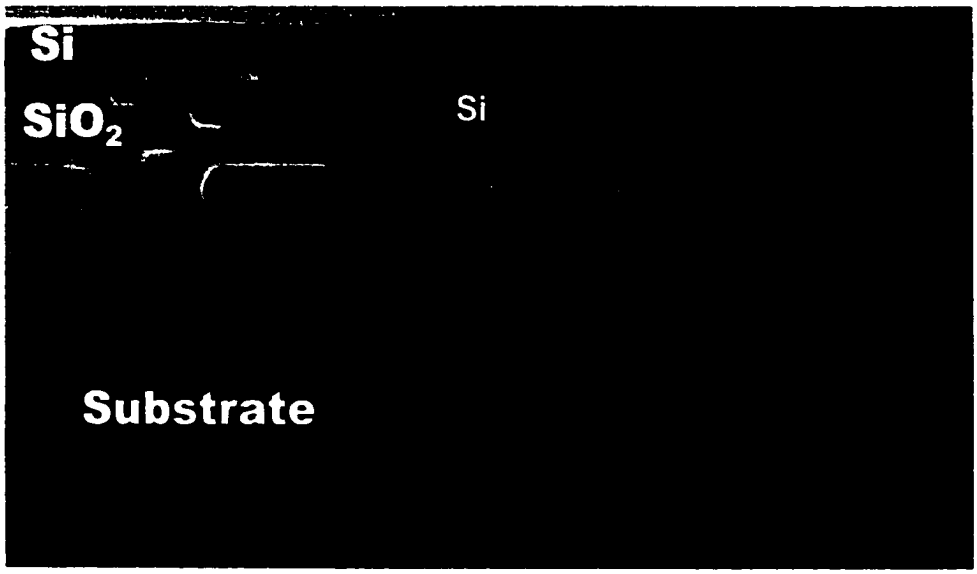

(a) Uncapped

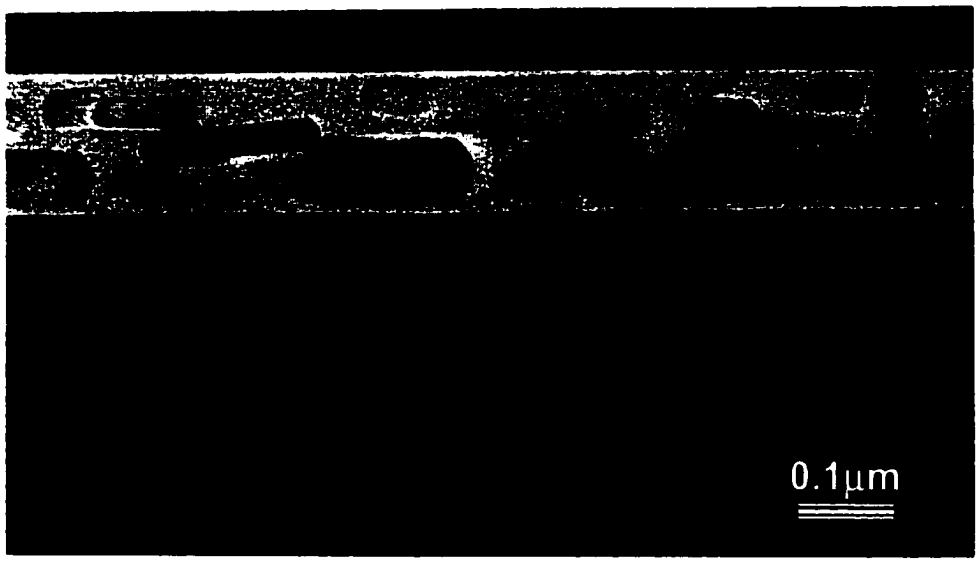

(b) Capped

Figure 6.10 TEM micrographs of SIMOX samples implanted with a dose of $5.0x10^{17}/cm^2$ and annealed at 1350°C (a) without and (b) with protective cap.

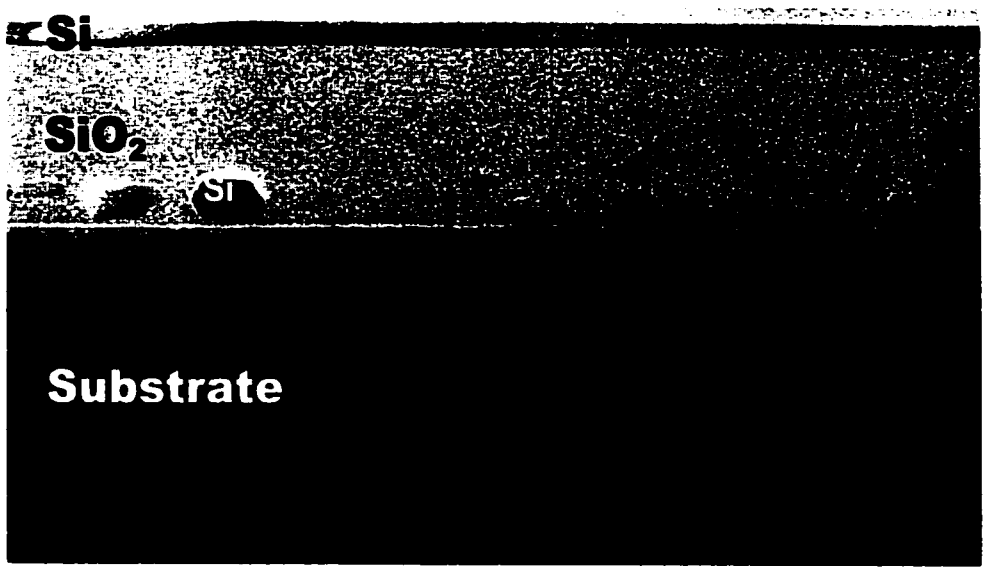

(a) Uncapped

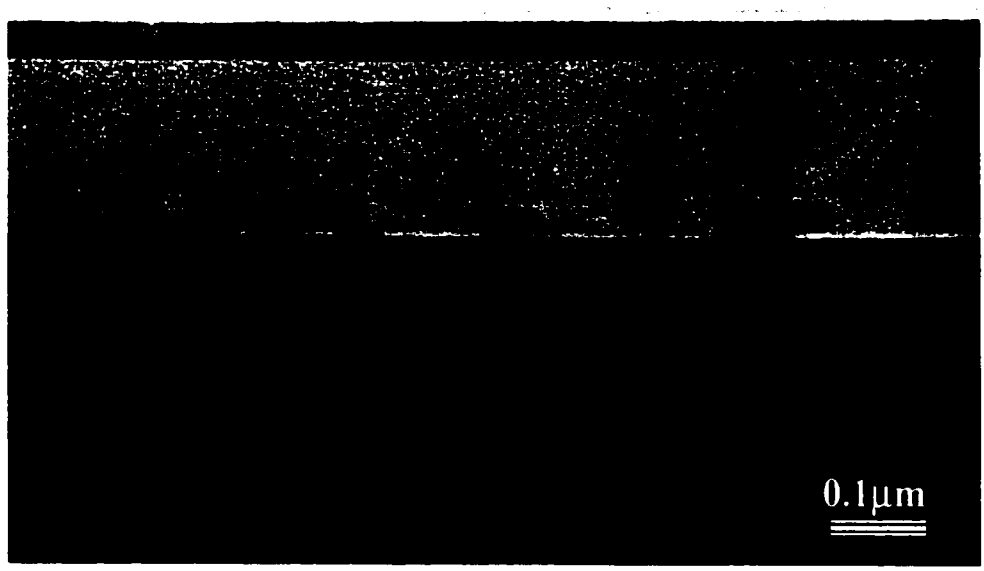

(a) Uncapped

Figure 6.11 TEM micrographs of SIMOX samples implanted with a dose of $7.0 \times 10^{17}/cm^2$ and annealed at 1350°C (a) without and (b) with protective cap.

Table 6.1. Layer thickness of SIMOX samples annealed without and with surface protective cap.

Dose ($x10^{17}/cm^2$)	Uncapped		Capped	
	Top Si Layer (nm)	BOX layer (nm)	BOX layer (nm)	Top Si layer (nm)
1.5	-	-	-	-
2.0	105	48	-	-
2.5	93	57	65	105
3.0	80	73	77	95
3.5	68	87	88	82
4.0	58	115	116	71
5.0	38	149	136	58
7.0	24	177	173	35

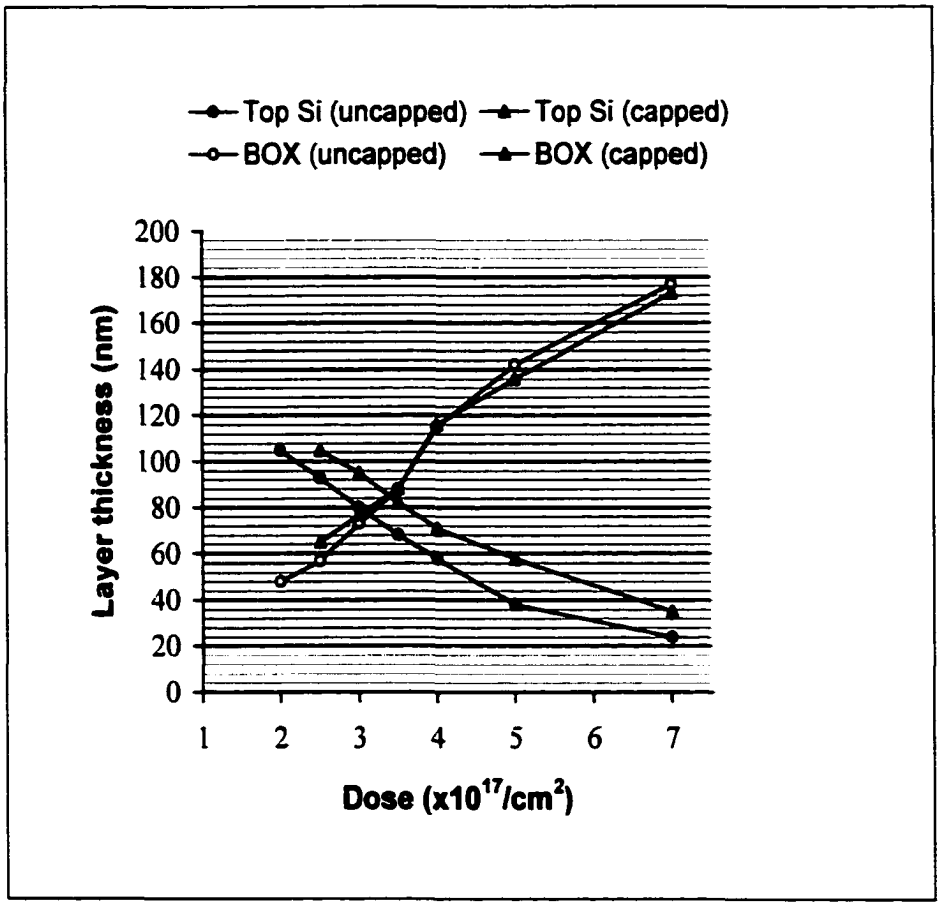

Figure 6.12 Dose dependence of the thickness of the top Si layer and BOX layer for capped and uncapped samples.

The effect of surface capping on the density of crystallographic defects in the top Si layer was evaluated by determining the density of defects in both the capped and uncapped samples using the etch-pit technique and optical microscopy. Quantitative data obtained from the analysis is presented in Table 6.2. The variation of defect density with implantation dose was found to be the same for both capped and uncapped samples. In both sets of samples, there exists a threshold dose of $3.5 \times 10^{17}/cm^2$ at which a low defect density was observed. Above and below this dose, the defect density increases. However, the uncapped samples were found to contain slightly lower defect densities than the capped samples. The trend in the defect density profile for both sets of samples is schematically represented in Figure 6.13. This defect density profile observed for these low-dose low-energy samples is generally similar to that observed in a set of low-dose samples implanted at 200 keV [74]. For this set of samples, the lowest defect density occurred at the dose of $4.5 \times 10^{17}/cm^2$.

Table 6.2. Density of defects in the top Si layers of capped and uncapped SIMOX Samples.

Dose ($x10^{17}/cm^2$)	Defect density ($x10^3/cm^2$)	
	Uncapped	Capped
1.5	100	400
2.5	40	120
3.0	3	6
4.0	1.5	6
5.0	700	5000

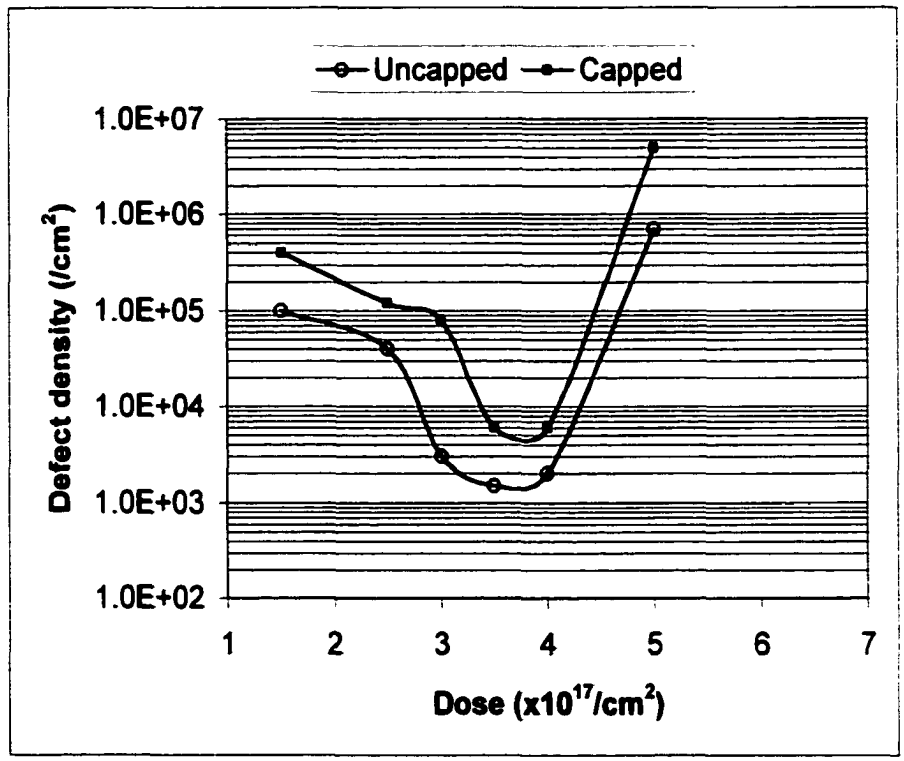

Figure 6.13 Defect density (etch pit) in low-dose low-energy SIMOX annealed with and without a surface protective cap.

CHAPTER 7

DISCUSSION

The results presented in the preceding chapters of this dissertation have shown clearly the strong dependence of microstructural development of the low-dose low-energy SIMOX materials on processing conditions. This work has demonstrated on the basis of experimental observations that an optimum processing scheme can be obtained to produce device-quality ultra-thin SIMOX substrates. The primary objective of this chapter is to discuss the various aspects of the relationships between the processing parameters and the resulting microstructural features. The emphasis will be primarily on the effect of implantation dose, energy, annealing temperatures and surface capping.

7.1 Effect of Implantation Dose

7.1.1 As-implanted samples

The implantation dose generally determines the thickness of the BOX layer. It has a profound effect on the microstructure of both the as-implanted and the annealed materials. From the study of the microstructures of a set of as-implanted samples at 65 keV with doses from $2.0x10^{17}/cm^2$ to $7.0x10^{17}/cm^2$, it was found that a continuous BOX layer was formed only in the highest dose ($7.0x10^{17}/cm^2$) after implantation step. This was confirmed by SIMS depth analysis of oxygen concentration for the samples in Figure 4.3 [68]. The spectra show that a skewed distribution was obtained for doses in the range of $2.0x10^{17}/cm^2$ to $5.0x10^{17}/cm^2$ but the implanted oxygen distribution saturated and became flat-topped at the highest dose. The experimental results indicate that the critical

dose (Q_c^I) required to form a continuous BOX layer after implantation at 65 keV is between $5.0x10^{17}/cm^2$ and $7.0x10^{17}/cm^2$. The value of Q_c^I can be estimated by a semi-empirical model developed by Li and Kilner [69] using the following equation:

$$Q_c^I = 2.5 N_O^{SiO_2} \Delta R_p \qquad 7.1$$

where $N_O^{SiO_2}$ is the number of oxygen atoms per unit volume in the buried SiO_2 layer, and ΔR_p is the straggle of oxygen projected range. This equation was derived from analysis of the physical processes and experimental results. At 65 keV, ΔR_p is 53 nm according to calculation by TRIM-90 program [67] and $N_O^{SiO_2}$ is $4.48x10^{22}/cm^2$. The value of Q_c^I estimated using equation 7.1 is ~ $6.0x10^{17}/cm^2$. This value supports the observation above.

An important feature in the microstructure of the as-implanted samples is the presence of multiply faulted defects (MFDs), in the lower portion of the top Si layer. The defects were studied extensively by Visitserngtrakul et al. [52]. They characterized the defect as consisting of several discontinuous stacking faults separated by two to eight atomic layers. They suggested that the formation of MFDs is related to the stresses generated by the volume change associated with precipitate formation occurring at the upper edge of the implantation range. The stresses, as reported by Tan and Tice [75], can be relieved by forming shear loops which are composed of partial dislocations. Implantation temperature is found to be critical for the formation of MFDs [52]. At high implantation temperatures (550°C-700°C), the sheer loops are sufficiently mobile to move and sheer the silicon crystal [76] resulting in a high density of MFDs. Though the densities of MFDs in the as-implanted samples studied in this dissertation were not

determined, we expect them to be low because they were implanted with low doses and the implantation temperature of 500°C was not high enough to give sufficient mobility to the sheer loops.

The most important result from the study of the as-implanted samples is the existence of a mixed structure of silicon and oxygen precipitates around the oxygen projected range. This structure was observed in the samples with dose ranging from $3.5x10^{17}/cm^2$ to $5.0x10^{17}/cm^2$. This result indicates that the implanted oxygen atoms locally redistribute during implantation which causes some areas to be enriched or deficient in oxygen. This local variation in oxygen content may occur randomly across the implanted zone but on small scale, hence no perceptible change in the SIMS oxygen concentration profiles in Figure 4.3.

RBS analysis was also performed to evaluate the effect of implantation dose on damage accumulated in the top Si layer during implantation. A comparison of the crystal disorder produced at different doses was made by random/channeling RBS. The crystal disorder parameter, χ_{min}, defined as the ratio of the channeled to random backscattering yield, was assessed near the damage peak. The values of χ_{min} for the as-implanted samples increased with increasing implantation dose, from 22% in the lowest dose to 70% in the highest dose. This result is consistent with other observations at different implantation energies [77], where higher doses were found to produce more damage during implantation. This trend can be understood by considering two factors that affect the channeling characteristics of the top Si layer: (i) lattice defects and (ii) oxygen precipitation. First, oxygen implantation into silicon introduces lattice defects due to the

transfer of energy governed mainly by collision with the lattice atoms (nuclear stopping). The exchange of energy through nuclear collisions generates lattice phonons and atomic displacements. A high concentration of lattice point defects is created at the peak of the nuclear energy loss. The concentration of the defects depends on number of collisions which increases with increasing dose. Second, the formation of oxygen precipitates in the top Si layer introduces a disordered phase into the lattice structure. At higher doses, more oxygen atoms become available to form oxygen precipitates especially around the peak of nuclear collisions.

7.1.2 Annealed Samples

A high-temperature annealing is a necessary step in SIMOX production. The microstructures of a set of annealed samples implanted with dose ranging from $1.5x10^{17}/cm^2$ to $7.0x10^{17}/cm^2$ were characterized by TEM. The results show significant differences in microstructures as the dose increases from the lowest to the highest. A continuous BOX layer does not form in the lowest-dose sample of $1.5x10^{17}/cm^2$ since it is lower than the critical dose for forming a continuous BOX layer after annealing. This critical value is denoted Φc^A. Li and Kilner [69] developed a semi-empirical model to determine the critical minimum dose required to form a continuous BOX layer and is given as:

$$\Phi c^A = (\alpha R_p)\, N_O^{SiO_2} \qquad 7.2$$

where R_p is the projected range, αR_p is the distance between the damage peak (R_d) and R_p, $\alpha = (R_p - R_d)/R_p$ and $N_O^{SiO_2}$ is the number of oxygen atoms per unit volume in the

buried SiO_2 layer. Setting R_p = 147 nm at 65 keV according to calculation by TRIM-90 program [67] and α = 0.30 [69], equation 7.2 gives the value of Φc^A to be ~ $1.98x10^{17}/cm^2$. This value is in good agreement with the observed value of $2.0x10^{17}/cm^2$ when a continuous BOX layer was formed after annealing (Figure 4.7). At doses equal or greater than $2.0x10^{17}/cm^2$, the BOX layer forms continuously.

In the dose range of $2.0x10^{17}/cm^2$ and $2.5x10^{17}/cm^2$ the BOX layer forms continuously without the presence of silicon islands. However, above $2.5x10^{17}/cm^2$, a continuous BOX layer forms with the presence of silicon islands. From these results, it can be concluded that for implantation energy of 65 keV, the dose range of $2.0x10^{17}/cm^2$ and $2.5x10^{17}/cm^2$ is the optimum for the BOX layer to form continuously without silicon islands. Several studies have reported the existence of such optimum doses at various implantation energies [15,54,78]. Table 7.1 summarizes the results for comparison. In general, the higher the implantation energy, the higher the oxygen dose required to form an island-free BOX layer because of the larger projected range and deeper penetration distance caused by the higher implantation energy. Note that other parameters such as the implantation temperature, annealing ambient, and implanter discrepancy may also shift the value slightly. At higher doses where the mixed structures formed in the as-implanted state, the BOX layer contained silicon islands after annealing. Therefore, it is reasonable to suggest that the mixed structure of the as-implanted samples is the precursor for forming silicon islands in the BOX layers after annealing.

Table 7.1 Correlation of dose, energy and layer thickness. For all conditions, a continuous BOX layer is formed without silicon islands.

Energy (keV)	Dose ($x10^{17}cm^{-2}$)	Si Layer Thickness (nm)	BOX Thickness (nm)
20 [15]	1.5	12.5	36
30 [54]	2.3	50	50
65 [this result]	2.5	90	60
70 [15]	3.3	115	80
80 [15]	6.0	140	160
160 [78]	7.0	290	160

Variations in the layer thickness of the annealed samples with implantation dose were determined. It was found that the thickness of the BOX layer increases while that of the top Si layer decreases with increasing dose. The decrease in the top Si layer with increasing dose can simply be attributed to the growth of the BOX layer at the expense of the top Si layer. The thickness of the BOX layer and the top Si layer was estimated using semi-empirical models (Equation 4.1 and 4.2, respectively) [69]. The calculated values were compared with the measured values obtained from TEM observations. It can be seen from Table 4.1 that a discrepancy exists between the measured and the calculated values. However, the extent of the discrepancy appears to be dose dependent. First, we look at the thickness values obtained for the BOX layer. A small discrepancy occurs in the dose range between $2.0x10^{7}/cm^{2}$ to $3.5x10^{7}/cm^{2}$. The discrepancy starts to widen at the dose of $4.0x10^{17}/cm^{2}$ (28%), reaching the largest (38%) at the dose of $5.0x10^{17}/cm^{2}$ and then decreases to 13% at the highest dose ($7.0x10^{17}/cm^{2}$). The reason for this trend may be explained by considering the effect of silicon islands on the BOX layer thickness. By examining the island density plot in Figure 4.15, it becomes clear that the trend of the discrepancy described here can be related to the island density profile in which the density rises sharply above the dose of $4.5x10^{17}/cm^{2}$ reaching a peak at the dose of $5.0xI0^{17}/cm^{2}$ and then drops considerably at highest dose ($7.0x10^{17}/cm^{2}$). It is also evident from the TEM micrographs in Figures 4.7 to 4.13 that the islands occupy a significant volume of the BOX. This can lead to increase in the BOX thickness. This effect was probably not taken into account in the formulation of equation 4.1. For the top Si layer, the discrepancy between the measured and the calculated values may be caused

by two factors. First, the loss of portion of the top Si layer during annealing and second, the increase in the BOX layer as result of silicon islands. These factors might account for the observed top Si thickness being lower than the calculated values.

7.1.3 Defect Density in the top Si layer

The dose dependence of the defect densities in the top Si layers of the annealed samples was investigated by the etch-pit technique. The results show that for 65 keV the sample with the dose of $3.5x10^{17}/cm^2$ contains lowest density of defects in the top Si layer. Above and below this dose, the defect density increases. The defect density profile observed for this set of low-dose low-energy samples is generally similar to that observed in a set of low-dose samples implanted at 180 keV [44] and 200keV [74]. This observed defect behavior in low-dose SIMOX is a subject of much discussion in several papers. Krause et al. [79] have suggested that two defect formation mechanisms operate in low-dose SIMOX materials, one operating at doses below the optimum dose and the other above. The defect formation mechanism active at doses below the optimum consists of formation of extrinsic stacking faults (SFs) during thermal ramping at ~ 1000°C, which unfault above 1200°C to form threading dislocations (TDs). Above the optimum dose, the defect mechanism consists of formation of dislocation half loops (DHLs) during implantation, which upon annealing transforms into TDs. At the optimum dose, there is little excess of interstitials to produce SFs or vacancies to produce DHLs, thus minimizing the density of TD precursor defects. In the present study, no DHL was observed in any of the as-implanted samples, which may be attributed to the low

implantation energy used. As a consequence, a different mechanism may account for the defect behavior in the samples, and further studies are required to understand this aspect in detail.

7.2 Microstructural Evolution during Intermediate-Temperature Annealing

Annealing at intermediate temperatures of 900°C to 1200°C shows developments in the microstructure of low-dose low-energy SIMOX. No significant changes occur in the 900°C sample except small shrinkages in the MFDs and {113} defects caused probably by a slight redistribution of silicon and oxygen. In the 1100°C sample shown in Figure 5.3 several changes occur in the microstructure. The surface region appears to be free of oxygen precipitates because those that are smaller than the critical size required for stability at this temperature are dissolved. All the MFDs are eliminated probably by stress relief mechanisms at elevated temperatures. It is likely, as suggested by Visitserngtrakul et al. [80] that at 1100°C the mobility of the trailing partial-dislocations becomes equal to that of the leading partial-dislocations, hence the two match up, and generate perfect dislocations. A considerable portion of the defect-rich zone of the substrate containing mostly {113} defects and small SFs is removed. AES profiles (Figure 5.9) show oxygen redistribution from the wings of the implanted profile towards the growing precipitates in BOX region. The crystallinity of the Si layer is significantly restored following the onset of the damage recovery process and the gradual dissolution of oxygen precipitates in the layer. A significant improvement occurs in the surface roughness due to surface regrowth with the driving force to minimize the surface energy

through reduction in surface area. The system attempts to adopt a flat surface which gives the lowest total surface free energy according to the general thermodynamic consideration of surface morphology. The surface regrowth possibly occurs through two diffusion mechanisms, both of which occur simultaneously. The first is surface diffusion, which involves the transport of silicon atoms from the humps to the dips on the surface. The second is bulk diffusion, which involves migration of silicon interstitials to the surface. The mechanisms outlined above for the surface regrowth commonly take place in sintering of compact particulates [81].

In the 1200°C sample shown in Figure 5.4, the microstructure changes drastically. There is a remarkable improvement in the surface roughness. The surface regrowth is thermally activated and the regrowth rate increases with increasing temperature according to the Arrhenius relation. The crystallinity of the top Si layer of this sample is considerably restored. This can be attributed to the progressive increase in the damage recovery process and dissolution of oxygen precipitates in the layer. The defect-rich zone that extends into the underlying substrate in the as-implanted material is completely recovered to a crystalline Si. Krause et al. [42] have suggested that the disappearance of {113} defects from this region is due to shrinkage and dispersal of excess Si interstitials from which they were formed. A mass transport of oxygen from the top Si layer and from the substrate into the BOX region causes the silicon striations formed during the implantation step to break up into elongated hexagonal shapes.

Evolution of oxygen precipitates in the top Si layer during intermediate temperature annealing was studied through high-resolution TEM imaging. Measurements

were made from TEM images to quantify the oxygen precipitates. The spatial parameters that were of interest were mean size, number density, and volume fraction. The results show that annealing at 900°C for 2 hours does not significantly change the above parameters of the precipitates. This shows once again that the thermal activity at 900°C is not sufficiently high to induce mass redistribution of oxygen. At 1100°C for 2 hours, there is a considerable change in the precipitates compared to the as-implanted sample. While the mean size increases at this temperature, both the number density and volume fraction decrease. The increase in the mean size and decrease in the number density is a proof that the precipitates coarsen at this temperature. Within the measurement error, TEM and SIMS comparisons established that essentially all the implanted oxygen was trapped by precipitates in the as-implanted sample. Based on this, it is reasonable to suggest that growth of precipitates through consumption of oxygen in solution is negligible and that Ostwald ripening is the main growth mechanism. The decrease in volume fraction shows however that the ripening process is non-conservative. In a conservative Ostwald ripening process the total number of solute atoms and volume fractions remain constant overtime. This occurs mostly in closed systems. In these systems, redistribution of solute atoms occurs only through direct exchange between precipitates with the net result that smaller ones dissolve while larger ones grow. In SIMOX, the top Si layer is not isolated but forms part of an oxygen diffusion continuum. When the smaller precipitates dissolve during annealing, all the oxygen is not incorporated into the larger precipitates in the layer. Some can diffuse out of the sample and others can diffuse towards the developing BOX layer. The mechanism that dominates

depends to a large extent on the annealing temperature. Generally, more oxygen diffuses towards the BOX layer as the annealing temperature increases. Based on the quantitative data obtained from TEM images, the growth rate of oxygen precipitates in the top Si layer during annealing was determined. The analysis of precipitate evolution in SIMOX is complicated because of an inhomogeneous distribution of the precipitates and the effect of complex interaction between defects and oxygen. To develop a growth model that describes closely the kinetical behavior of the precipitates requires vigorous formulations using advanced mathematics which is beyond the scope of this study. In deducing a simple growth rate, the study was restricted to special (limiting) case of Ostwald ripening, which is the asymptotic behavior ($t \rightarrow \infty$) of dilute systems (vanishing volume fraction of precipitates) in the limits of pure diffusion or reaction controlled mass exchange between precipitates (Lifshitz, Slyozov and Wagner theory of Ostwald ripening (LSW theory)). Taking the volume fraction of the precipitates prior to annealing to be close to zero as confirmed by the experimental data, an expression for time evolution of the mean radius of the precipitates was derived (Equation 5.8). Comparison of the calculated and measured values for the mean size of the precipitates shows a fair agreement considering the errors in the TEM measurements and the deviations in the measured values.

7.3 Effect of Annealing Conditions

7.3.1 Effect of Annealing Temperature

The effect of final annealing temperature on the microstructure of low-dose low-energy SIMOX was evaluated at two temperatures, 1300°C and 1350°C. The TEM results show no significant difference between the microstructures of the samples annealed for 6 hours at 1300°C and 1350°C. Results from channeling RBS also show that the crystallinity of the top Si layer was completely restored after annealing for 6 hours at either of the two temperatures. This indicates that under these implantation conditions, annealing at 1300°C was adequate to produce a complete SIMOX structure. In our previous study [82], we found that for a comparable dose ($5.0x10^{17}/cm^2$) implanted at 190 keV, the BOX layer did not completely form and some oxygen precipitates still remained in the top Si layer after annealing for 5 hours at 1310°C as shown in Figure 7.1a. The BOX/substrate interface is characterized by incursions in many areas due to connections between the substrate and silicon inclusions. Annealing had to be performed at 1350°C for this low-dose high-energy SIMOX to dissolve all the oxygen precipitates in the top Si layer and to form a well-defined BOX layer as shown in Figure 7.1b. In another sample implanted at 190 keV but at a higher dose of $8.3x10^{17}/cm^2$, a good quality top Si layer was formed after annealing at 1310°C (Figure 7.2a) or 1350°C (Figure 7.2b) for 5 hours. These experimental observations can be explained based on the formation process of the BOX layer which was presented in section 2.1.

As mentioned in section 2.1, in low-dose SIMOX process, the BOX layer does not form after the implantation step. The implanted structure consists of isolated oxygen

precipitates of various sizes in the silicon matrix with the largest occurring in the vicinity of R_p. The coarsening and coalescence of these precipitates to a single BOX layer during annealing is more critical than in the high-dose case because of the smaller thickness involved. The size distribution, density and separation distances of the precipitates depend strongly on implantation conditions, particularly dose and energy. For low doses at high energies, the fewer oxygen implanted are distributed over a wider range due to high-energy multiple collisions from the implantation. Consequently, the precipitates form at lower densities and far from each other. As the dose increases the density and the size of precipitates increase resulting in shorter distances between precipitates.

Several experiments with samples implanted with low doses have suggested that two preferential regions of SiO_2 precipitation appear [83,84]. The first is at the depth of maximum damage (D_p) in the top Si layer. The second occurs at the projected range (R_p), where the BOX layer is formed. The results of this study are in agreement with the previous observations. Figure 7.3 displays two precipitate regions in the samples implanted at 190 keV with a dose of (a) $5.0x10^{17}/cm^2$ and (b) $8.3x10^{17}/cm^2$ and annealed both at 1310°C without holding. In Figure 7.3 (a), the widths of the precipitates around D_p (upper region) and R_p (lower region) are marked h_1 and h_2, respectively. The corresponding regions in the higher dose sample (Figure 7.3b) are marked h'_1 and h'_2, respectively. Larger precipitates occur in the lower region because it contains most of the implanted oxygen. On the other hand, a higher density of smaller precipitates occurs in the upper region because the heavily damaged lattices located there accommodate more oxide nucleation sites. To form a continuous BOX layer, precipitates that exist in the

upper region must be dissolved and incorporated into the larger ones in the lower region during annealing. The driving force for the dissolution of precipitates in the upper region is attributed to the effect of Ostwald ripening. The dissolution process is influenced by the vertical distance separating the two precipitate regions and the annealing temperature. The separation distance is influenced by the implantation energy and dose. For samples implanted at high energy with lower doses such as the $5.0x10^{17}/cm^2$ used in this study, there is an appreciable separation between the two regions, h_1 and h_2. This inhibits the dissolution of the precipitates in the upper region. As a result, as the ramping progresses into the higher temperatures, many of the precipitates in this region grow larger via lateral coarsening and thus becoming stable. This explains why in the sample implanted at 190 keV with a dose of $5.0x10^{17}/cm^2$ some precipitates remained in the top Si layer and the BOX layer was not well formed after annealing for 5 hours at 1310°C. Therefore, to form a continuous BOX layer, it requires a combination of a sufficiently high annealing temperature (~1350°C) and longer holding time to dissolve and incorporate the precipitates in the upper region into the lower region. At a higher dose such as $8.3x10^{17}/cm^2$, the vertical separation between h'_1 and h'_2 decreases (compared to h_1 and h_2) since the width of the lower region grows with increasing dose (see Figure 7.3b). This eases the dissolution process of the precipitates in the upper region. Relatively lower annealing temperatures together with 5 hours holding time is sufficient to complete the precipitation processes.

Implanting at lower energy results in a shorter distance between D_p and R_p. For $^{16}O^+$ implanted at 65 keV the calculated distance according to TRIM [67] is about 44 nm

compared to 122 nm at 190 keV. Thus, in low-energy implanted SIMOX materials, the two precipitation regions become closely spaced or may even merge depending on the dose. The latter case appears to be true for the sample implanted at 65 keV with a dose of $4.5x10^{17}/cm^2$ since only a single precipitate region was observed in the sample annealed at 1200°C for 2 hours (Figure 5.4). Under these conditions, a relatively lower annealing temperature (equal or slightly above 1300°C) can be employed to completely dissolve all the oxygen precipitates in the top Si layer to form a continuous BOX layer at the projected range. We believe this explains why in the sample implanted at 65 keV, a top Si layer contains no oxygen precipitates and a continuous BOX layer was formed after annealing at 1300°C for 6 hours.

Based on results presented in this study and those previously reported, we can reasonably suggest that for the low-dose SIMOX, the implantation energy is an important factor for determining the appropriate annealing temperature between 1300°C and 1350°C for forming a good quality SIMOX wafer.

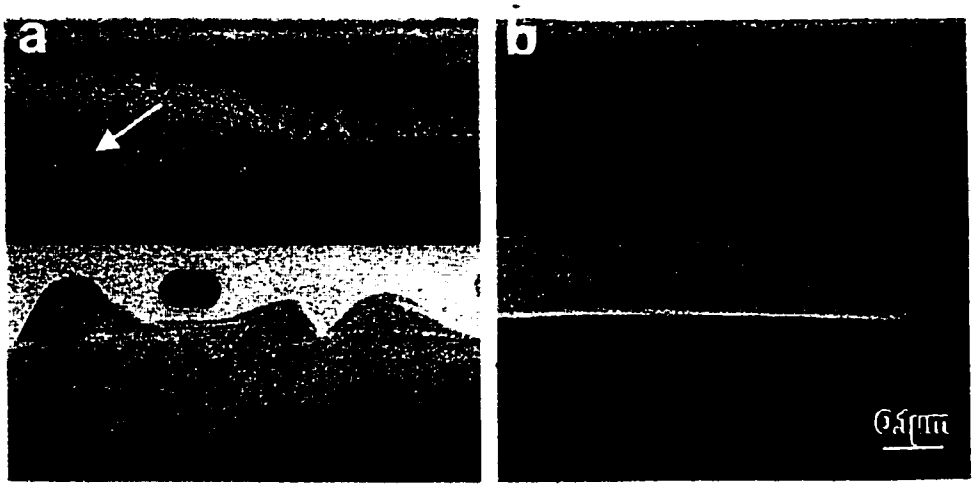

Figure 7.1 Cross-sectional TEM micrographs of SIMOX samples implanted at 190 keV with a dose of $5.0 \times 10^{17}/cm^2$ and annealed for 5 hours at (a) 1310°C and (b) 1350°C. Arrow indicates an oxide precipitate in the top Si layer.

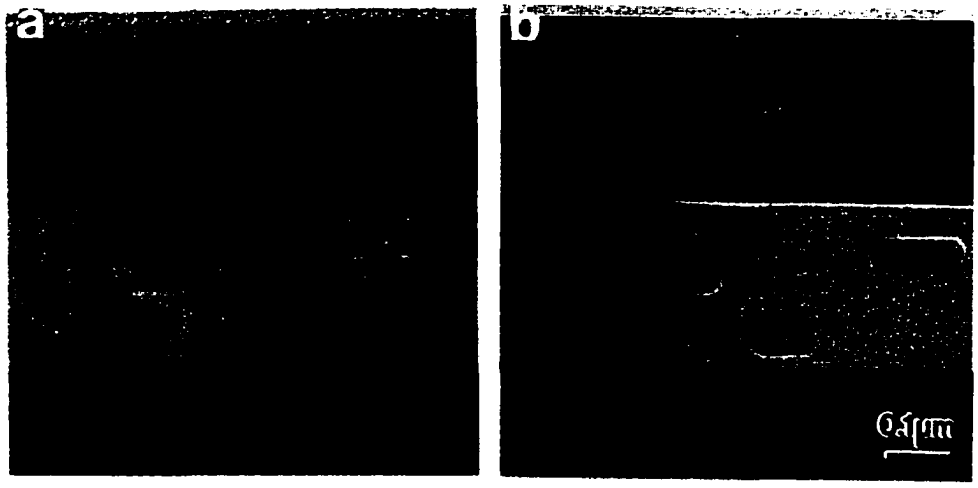

Figure 7.2. Cross-sectional TEM micrographs of SIMOX samples implanted at 190 keV with a dose of $8.3 \times 10^{17}/cm^2$ and annealed for 5 hours at (a) 1310°C and (b) 1350°C.

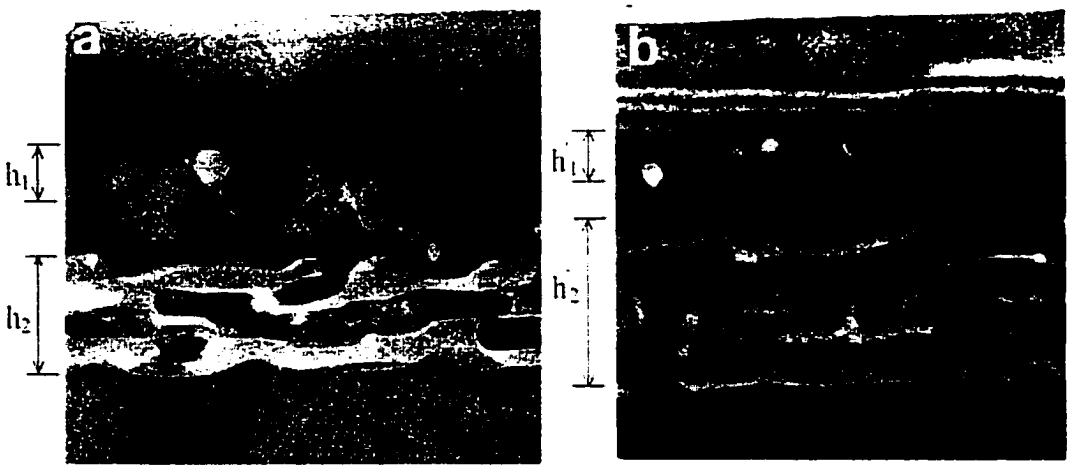

Figure 7.3 Cross-sectional TEM micrographs of SIMOX samples implanted at 190 keV with a dose of (a) $5.0x10^{17}/cm^2$ and (b) $8.3x1017/cm^2$ and annealed at 1310°C, 0 hrs. h_1 and h_2 represent the widths of the upper and lower precipitate regions in the sample (a), respectively. The corresponding regions in the sample of (b) are marked h'_1 and h'_2, respectively.

7.3.2 Effect of Surface Capping

The effect of surface capping during annealing was studied by performing the annealing treatment under two types of conditions. One set of wafers with doses of 1.5, 2.0, 2.5, 3.0, 3.5, 4.0, 5.0, and $7.0x10^{17}/cm^2$ was annealed for 4 hours at 1350°C in Ar + 0.5% O_2 without a protective cap on the sample surface. The second set also with the same doses as the first was annealed for 6 hours at 1350°C in Ar + 5% O_2 covered with a protective layer of SiO_2 (TEOS) on the sample surface. Under annealing without a protective cap, the BOX layer starts to form continuously at the dose of $2.0x10^{17}/cm^2$. Under annealing with protective cap on the other hand, the BOX layer starts to form continuously at the dose of $2.5x10^{17}/cm^2$. This suggests that the implanted oxygen concentration at a dose lower than $2.5x10^{17}/cm^2$ alone is not sufficient to form a continuous BOX layer when annealed with a protective cap. For the uncapped samples, oxygen from the ambient can diffuse through the ultra-thin top Si layer to react with silicon atoms which results in the completion of the BOX layer provided the dose is not too low (such as $1.5x10^{17}/cm^2$). For the capped samples, few oxygen atoms from the ambient can diffuse through the cap despite a ten times higher oxygen concentration in the ambient and a longer annealing time than that of the uncapped samples. At doses greater than $2.5x10^{17}/cm^2$ in both sets of samples, a continuous BOX layer forms but it contains numerous Si islands. The uncapped samples show slightly lower density of silicon islands than the capped samples because the extra oxygen diffused in from the ambient helps to oxidize some of the entrapped Si interstitials reducing the number of islands in the BOX layer.

The thicknesses of the layers in the capped and uncapped samples were measured from the TEM images. The results show that, for both sets of samples the thickness of the top Si layer decreases with increasing implantation dose since the BOX layer grows at the expense of the top Si layer. However, the top Si layer of the uncapped sample is thinner than that of the capped sample because a portion (~17 nm) of the layer is consumed by external thermal oxidation. The measurements performed on the BOX layer show no significant difference in thickness between the capped and uncapped sample. This suggests that the oxygen from the ambient helps the BOX layer in the uncapped to grow in the lateral direction to form a continuous BOX layer, but not high enough to induce growth in the vertical direction. In the so-called internal thermal oxidation (ITOX) process, the ambient oxygen content is usually about 30%, which is high enough to create an additional oxide to thicken the original BOX layer.

The effect of capping and uncapping on the growing BOX layer can be explained based on migration of oxygen into and out of the implanted zone. Under annealing without surface cap, oxygen from the ambient can diffuse into the implanted zone. The mechanism behind this process is the same as in the ITOX process. During the initial stages of annealing a thin thermal oxide forms at the bare wafer surface. As the annealing proceeds, molecular oxygen (O_2) diffuses through the thin thermal oxide and reacts with silicon at the interface between the thermal oxide and the top Si layer. At high temperatures the following two main reactions occur at the interface [85,86]:

$$\text{Si-Si} + O_2 \rightarrow \text{Si-O-Si} + O \qquad 7.3$$

$$\text{Si-Si} + O \rightarrow \text{Si-O-Si} \qquad 7.4$$

Reaction 7.3 generates oxygen atoms. Some of these atoms combine with silicon in reaction 7.4. The others diffuse through the thin top Si layer to the developing BOX layer because the diffusion coefficient of oxygen in silicon is very large at high temperatures and the long period of annealing (at least 4 hours). These oxygen atoms and those dissolved from smaller precipitates migrate to the larger precipitates that exist around the depth corresponding to the projected range of the implanted oxygen, and enlarged precipitates begin to coalesce into a continuous BOX layer. This enables the BOX layer to form continuously in the uncapped sample implanted with a dose as low as $2.0x10^{17}/cm^2$.

When the wafer surface is covered with the capping layer, it not only blocks oxygen from the annealing ambient to diffuse in, but also causes some of the implanted oxygen in the top Si layer to diffuse out. The capping layer, like the BOX layer, at sufficiently high temperatures acts as a precipitate of infinite size and becomes a sink for oxygen from the top silicon layer. As a consequence, the capping layer competes with the BOX layer for the dissolved oxygen in the top Si layer. The loss of implanted oxygen to SiO_2 capping layer during the annealing process for SIMOX formation has been reported by Li et al. [63]. In their experiment involving oxygen isotopes at various implant energies, the researchers found that the flux of implanted oxygen into the capping layer increases with decreasing implant energy (i.e. the shorter the distance between the cap and oxygen projected range, R_p). They also found that for low energy SIMOX, the buried oxygen precipitate layer tends to disappear when the dose is quite low. For our set of samples implanted at 65keV, it is reasonable to expect the capping layer to draw oxygen

from the top Si layer since R_p is close to the capping layer (~147 nm). In effect, the capping layer does not only act as barrier to oxygen from the ambient but also deprives the growing BOX layer of oxygen. Hence, it takes a higher dose of $2.5x10^{17}/cm^2$ to form a BOX layer in a capped sample compared to $2.0x10^{17}/cm^2$ in the uncapped one. At doses greater than $2.5x10^{17}/cm^2$, on the other hand, a continuous BOX layer forms because the amount of oxygen that remains in the implanted zone is still high enough to drive the precipitation process towards the formation of a continuous BOX layer.

The effect of surface capping on the density of defects in the top Si layer of annealed samples was evaluated through etch-pit analysis. The results show that the defect density profile is the same for both sets of samples. At a dose of $3.5x10^{17}/cm^2$, the sample contains the lowest density of defects. The uncapped samples contain slightly lower densities of defects than the capped samples because the capping layer affects the kinetics of oxygen and silicon interstitials in a way that results in a higher defect density. It is reported that the capping layer may even stabilize threading dislocations at high temperatures where under normal circumstances they would be expected to be annealed out [27]. This stability is believed to be provided via migrating oxygen atoms to the capping layer, which pins down the threading dislocations.

CHAPTER 8

SUMMARY AND CONCLUSIONS

The research presented in this study focused on the effect of implantation dose and annealing conditions on the microstructure of low-dose SIMOX samples implanted at 65 keV. The implantation dose was found to have a strong effect on the microstructure in both the as-implanted and annealed samples. The critical dose required to form a continuous BOX layer after implantation was found to exist between $5.0x10^{17}/cm^2$ and $7.0x10^{17}/cm^2$. This was supported by a predictive model which yielded a value of $6.0x10^{17}/cm^2$. In the lowest-dose sample ($2.0x10^{17}/cm^2$), the as-implanted structure consisted of oxygen precipitates of various sizes dispersed in the silicon matrix with the largest occurring at the oxygen projected range (R_p). The most important microstructural features observed in the as-implanted state were the mixed structures of silicon and oxygen precipitates which formed around R_p. These features were observed in the samples with doses ranging from $3.5x10^{17}/cm^2$ to $5.0x10^{17}/cm^2$. The existence of these features shows clearly that during implantation, local oxygen redistribution causes some areas to be enriched and others to be deficient in oxygen. Oxygen precipitates are then formed in the areas with high oxygen concentration. These structures then served as a precursor for silicon island formation during high-temperature annealing. The dominant crystallographic defects observed in the as-implanted state were multiply faulted defects (MFDs) and {113} defects. These defects were present in all the as-implanted samples. The density of MFDs is expected to be low in the samples studied because they were

implanted with low doses and at a temperature (500°) that is not sufficiently high to mobilize the sheer loops responsible for the formation of MFDs.

In the annealed samples, various microstructures occurred as the dose varied between the lowest and the highest. Due to the low oxygen content, the BOX layer was discontinuous at the lowest dose ($1.5x10^{17}/cm^2$). A "dose window" was found between $2.0x10^{17}/cm^2$ and $2.5x10^{17}/cm^2$, in which the BOX layer formed continuously without any observable silicon islands. At doses above $2.5x10^{17}/cm^2$, the BOX layer formed continuously but with the presence of silicon islands. The silicon island density increased with increasing dose until it reached a peak at the dose of $5.0x10^{17}/cm^2$, after which it decreased with increasing dose.

The investigation of the effect of dose on the density of defects in the top Si layers of the annealed samples showed that the lowest defect density occurred at implantation dose of $3.5x10^{17}/cm^2$. Above and below this dose, the defect density increased. Similar defect behavior is reportedly observed in low-dose high-energy SIMOX samples. It is suggested in this report that the defect behavior is caused by two different mechanisms which operate above and below the dose with lowest defect density. Further studies are needed to establish the defect mechanisms which operate in low-dose low-energy SIMOX.

The effect of dose on the layer thickness of the annealed samples was also investigated. Measured values were compared against calculated values. A discrepancy was found between the measured and the calculated values for both the BOX and the top Si layers. We found also that the extent of discrepancy was dose dependent. For the BOX

layer, much of the discrepancy was attributed to the presence of silicon islands in the BOX layer which was probably not accounted for in the model used for the calculation. The discrepancy in the values obtained for the top Si layer was caused by two factors, the growth of the BOX layer due to the presence of silicon islands and loss of thickness through thermal oxidation during high-temperature annealing.

Microstructural evolution during the ramping stage of the annealing process was studied by annealing samples at intermediate temperatures. It was found that the MFDs and {113} defects formed during the implantation step were reduced after annealing at 900°C for 2 hours and were eliminated after annealing at 1100°C and 1200°C, respectively. It was also found that the redistribution process for oxygen and silicon interstitials during annealing is initiated at 1100°C, which also recovered the crystallinity of top Si layer and developed the formation of the BOX layer. HRTEM imaging was performed on the as-implanted and the intermediate-temperature annealed samples to quantify oxygen precipitates in the top Si layer. Based on the data, a simple growth equation was derived to calculate the mean size of precipitates in the top Si layer as a function of temperature. Within the measurement error, there was a fair agreement between the measured and the calculated values.

The effect of annealing conditions, in particular effects of final annealing temperature and surface capping was investigated. It emerged from this investigation that the choice of the final annealing temperature depends on the implantation energy and dose. For low-dose low-energy SIMOX, the final annealing temperature was found not to be critical provided it is between 1300°C and 1350°C. For these materials, annealing at

1300°C for a sufficient amount of time (e.g. 6 hours) is adequate to produce well-defined SIMOX structure with a good quality top Si layer. The most important results from the study of the low-dose low-energy SIMOX samples was that perhaps for the first time, it was possible to understand the effect of surface capping during annealing on the microstructure. For the low-dose low-energy SIMOX with implanted structure close to the surface, the presence of surface cap adversely affected the formation of the BOX layer particularly at relatively lower doses ($< 3.0x10^{17}/cm^2$). The minimum dose required to form a continuous BOX layer after annealing is $2.5x10^{17}/cm^2$ compared to $2.0x10^{17}/cm^2$ for uncapped condition. The protective cap acts as a sink for oxygen in the top Si layer and competes with the growth of the BOX layer. The protective cap contributed also to the formation of a higher density of defects in the top Si layer by suppressing the annihilation of extended defects during the final annealing step.

From this study, it was possible to achieve a better understanding of microstructural developments in ultra-thin SIMOX materials as a function of processing conditions. The correlations between the processing conditions and the microstructure of these SIMOX materials established the major statement of this dissertation, scientifically as well as with respect to the technological significance. The correlations are summarized in Table 8.1 and 8.2.

Table 8.1 Effect of implantation dose on the microstructure of SIMOX materials

Dose ($x10^{17}/cm^2$)	As-implanted	Annealed at 1350°C, 6h, $Ar+O_2$
1.5	Not studied	No continuous BOX layer forms $10^5 cm^{-2}$ defects in the top Si
2.0	MFDs present No continuous BOX layer forms Structure composed of oxygen precipitates of various sizes	BOX layer is continuous No silicon islands observed
2.5	Not studied	BOX layer is continuous No silicon islands observed $4x10^4 cm^{-2}$ defects in the top Si
3.0	Not studied	BOX layer is continuous $1.8x10^9 cm^{-2}$ Si islands $3x10^3 cm^{-2}$ defects in the top Si
3.5	MFDs No continuous BOX layer Mixed structure of silicon and Oxygen precipitates forms around the projected range	BOX layer is continuous $3.3x10^9 cm^{-2}$ Si islands $1.5x10^3 cm^{-2}$ defects in the top Si
4.0	Not studied	BOX layer is continuous $4.4x10^9 cm^{-2}$ Si islands $2.0x10^3 cm^{-2}$ defects in the top Si
4.5	MFDs present No continuous BOX layer forms Mixed structure of silicon and Oxygen precipitates formed around the projected range	Not studied
5.0	MFDs present No continuous BOX layer Mixed structure of silicon and Oxygen precipitates formed around the projected range	BOX layer is continuous $1.1x10^{10} cm^{-2}$ Si islands $7.0x10^5 cm^{-2}$ defects in the top Si
7.0	MFDs present Continuous BOX layer forms	BOX layer is continuous $1.3x10^8 cm^{-2}$ Si islands Defect density not determined

Table 8.2 Effect of annealing conditions on the microstructure of SIMOX materials

Temperature, °C	Observations
900	MFDs and {113}defects were shortened Mean size of precipitates increased slightly
1100	MFDs were eliminated {113}defects considerably shortened Redistribution process for oxygen and silicon interstitials initiated
1200	{113}defects eliminated Surface regrowth and crystal recovery intensified
1300	Crystallinity of the top Si layer completely restored Continuous and uniform BOX layer was formed
1350	Same as at 1300°C
Surface capping	Thickness of top Si layer was preserved Minimum dose to form a continuous BOX layer after annealing was $2.5 \times 10^{17}/cm^2$ Slighly higher densities of defects and silicon islands were generated
No surface capping	A portion of the top Si layer (~17 nm) was consumed through surface oxidation. Minimum dose to form a continuous BOX layer after annealing was $2.0 \times 10^{17}/cm^2$

REFERENCES

1. T.D. Stanley, *IEEE Transactions on Nuclear Science*, 35, 1346 (1988).

2. T. Iwamatsu, Y. Yamaguchi, Y. Inoue, T. Nishimura, and N. Tsubouchi, *IEDM Tech Dig.* 475 (1993).

3. W. Huang, K. Klein, M. Grimaldi, M. Racanelli, S. Ramaswami, J. Tsao, J. Foerstner, and B. Hwang, *IEDM Tech. Dig.* 449 (1993).

4. R. Dekker, W. Einden, and H. Maas, *IEDM Tech. Dig.* 75 (1993).

5. H. Wei and J. Chung, *IEDM Tech. Dig.* 739 (1993).

6. K. Izumi, M. Doken, and H. Ariyoshi, *Electron Lett.* 14/18, 594 (1978).

7. A. Wittkower, *Proc. Electrochem. Soc. Meetings*, Abstract No.440 (2001).

8. J.P. Colinge, *Silicon-on-Insulator Technology: Materials to VLSI* (Kluver Academic Publishers, Norwell, 1991).

9. S. Cristoloveanu and S.S. Li, *Electrical Characterization of Silicon-on-Insulator Materials and Devices* (Kluver Academic Publishers, Boston, 1995).

10. B. Johnson, P. Anderson, Y. Tan, S. Seraphin, and M. Anc, *Proc. Electron Micros. Soc. America*, 6, 1090 (2000).

11. O.W. Holland, D. Fathy, and D.K. Sadana, *Appl. Phys. Lett.* 69 (5), 674 (1996).

12. S. Nakashima and K. Izumi, *J. Mater. Res.* 8, 523 (1993).

13. N. Meyyappan, T. Nakato, J. Blake, and F. Sinclair, *Proc. IEEE SOI Conf.* Palm Springs, October (1993).

14. F. Namavar, E. Cortesi, B. Buchanan, J.M. Manke, and N.M. Kalkhoran, *Mater. Res. Soc. Symp. Proc.* 235, 109 (1992).

15. F. Namavar, B. Buchanan, E. Cortesi, and P. Sioshansi, *Mater. Res. Soc. Symp. Proc. IEEE SOS/SOI Conf.* p 117 (Stateline, Nevada, 1989).

16. J. Jiao, B. Johnson, S. Seraphin, M.J. Anc, and B.F. Cordts III, *Mat. Sci. Eng.* B72, 150 (2000).

17. M.L. Smith, *Electromagnetically Enriched Isotopes and Mass Spectrometry* (Butterworth Science, London, 1956).

18. M. Watanabe and A. Tooi, *Jpn. J. Appl. Phys.* 5, 737 (1966).

19. M.H. Badawi and K.V. Anand, *J. Phys.* D10, 1931 (1977).

20. J.P. Ruffel, D.H. Douglas-Hamilton, R.E. Karim, and K. Izumi, *Nucle. Instru. and Meth. Phys. Res.* B21, 862 (1987).

21. J. Stoemenos, C. Jaussaud, M. Bruel, and J. Margail, *J. Cryst. Growth*, 73, 546 (1985).

22. S. Visitserngtrakul, C.O. Jung, T.S. Ravi, B.F. Cordts III, D.E. Burke, and S.J. Krause, *Microscopy Semiconductor Material, Oxford, Great Britain, Inst. Phys. Ser.* 100, 557 (1989).

23. S. Visitserngtrakul, J. Barry, and S.J. Krause, *Mater. Res. Soc. Proc.* 163, 955 (1990).

24. S. Visitserngtrakul, S.J. Krause, B.F. Cordts III, and P. Roitman, *Vacuum*, 42, 353 (1991).

25. S. Visitserngtrakul, S.J. Krause, P. Roitman, D.S. Simons, and B.F. Cordts III, *Appl. Phys. Lett.* 59, 3004 (1991).

26. G. Ryding, T.H. Smick, M. Farley, B.F. Cordts III, R.P. Dolan, L.P. Allen, B. Mathews, W. Wray, B. Amundsen, and M.J. Anc, *Proc. Ion Implant Tech. Conf.* Austin, TX, 16 (1996).

27. K.J. Reeson, *Nucle. Instru. and Meth. Phys. Res.* B19/20, 269 (1987).

28. R.J. Chater, J.A. Kilner, P.L.F. Hemment, K.J. Reeson, and J.R. Davis, *Nucle. Instru. and Meth. Phys. Res.* B19/20, 290 (1987).

29. P.L.F. Hemment, *Mater. Res. Soc. Proc.* 33 (1984).

30. L. Csepregi, E.F. Kennedy, T.J. Gallagher, J.W. Mayer, and T.W. Sigman, *J. Appl. Phys.* 48, 4234 (1977).

31. C. Jaussaud, J. Stoemenos, J. Margail, M. Dupuy, and M. Bruel, *Appl. Phys. Lett.* 46, 1064 (1985).

32. A.E. White, K.T. Short, J.L. Batstone, D.C. Jacobson, J.M. Poate, and K.W. West, *Appl. Phys. Lett.* 50, 19 (1987).

33. B. Johnson, J. Jiao, S. Seraphin, T. Yan, T. Wilson, M. Anc, and B. F. Cordts III, *Proc. Electron. Micros. Soc. America*, 5, 746 (1999).

34. G.K. Celler, *Electrochem. Soc. Proc.* 90-7, 472 (1990).

35. S. Nakashima, T. Katayama, Y. Miyamura, A. Matsuzaki, M. Imai, K. Izumi, and N. Ohwada, *Proc. IEEE SOI Conf.* 71 (1994).

36. Y. Li, J.A. Kilner, R.J. Chater, P.L.F.Hemment, A. Nejim, A.K. Robinson, K.J. Reeson, C.D. Marsh, and G.R. Booker, *Electrochem. Soc. Proc.* 92-13, 368 (1992).

37. J-P. Colinge, *MRS Bulletin*, 23 (12), 16 (1998).

38. S. Reiss, K.-H. Heining, and W. Skorupa, *Nucle. Instru. and Meth. Phys. Res.* B102, 256 (1995).

39. J.C. Mikkelsen, Jr., *Mater. Res. Soc. Proc.* 59, 19 (1986).

40. S. Maillet, R. Stuck, J.J. Grob, A. Golanski, R. Pantel, and A. Perio, *Nucle. Instru. and Meth. Phys. Res.* B19/20, 294 (1987).

41. A.H. Van Omnen, B.H. Koek, and M.P.A. Viegers, *Inst. Phys. Conf. Ser.* 87, 385 (1987).

42. S.J. Krause, C.O. Jung, S. Wilson, R. Lorigan, and M. Burnham, *Mat. Res. Soc. Proc.* 107, 93 (1988).

43. D.A. Porter and K.H. Easterling, *Phase Transformations in Metals and Alloys*, p.44 (NewYork: Van Nostrand Reinhold, 1981).

44. S. Nakashima and K. Izumi, *J. Mater. Res.* 8, 523 (1993).

45. P.L.F. Hemment, K.J. Reeson, J.A. Kilner, C. Marsh, G.R. Booker, G.K. Celler, and J. Stoemenos, *Vacuum* 36, 11/12, 887 (1986).

46. S.M. Hu, *J. Appl. Phys.* 45, 1567 (1974).

47. Y. Bar-yan and J.D. Joannopoulos, *Phys. Rev. Lett.* 52, 1129 (1984).

48. G.D. Watkins, *Inst. Phys. Conf. Ser.* 23, 1 (1975).

49. C. Jaussaud, J. Stoemenos, J. Margail, A.M. Papon, and M. Bruel, *Vacuum*, 42, 341 (1991).

50. S. Seraphin and B. F. Cordts III, *Proc. Electron Micros. Soc. America*, 49, 862 (1991).

51. G. Brebec, R. Segun, C. Sella, J. Brevenot, and C. Martin, *Acta Met.* 28, 327 (1980).

52. S. Visitserngtrakul, S.J. Krause, and B.F. Cordts III, *J. Appl. Phys.* 69, 1784 (1991).

53. S. Visitserngtrakul, B.F. Cordts III, and S.J. Krause, *Mater. Res. Soc. Proc.* 157, 161 (1990).

54. L.F. Giles, N. Meyyappan, A. Nejim, J. Blake, F. Cristiano, and P.L.F. Hemment, 94-11, *Electrochem. Soc. Proc.* 50 (1994).

55. J. Stoemenos and J. Margail, *Thin Solid Films*, 135, 115 (1986).

56. C. Jaussaud, J. Margail, J. Stoemenos, and M. Bruel, *Mater. Res. Soc. Symp. Proc.* 107, 17 (1988).

57. K.J. Reeson, C.D. Marsh, R.J. Chater, J.A. Kilner, K.N. Christensen, A.K. Robinson, P.L.F. Hemment, G. Harbeke, E.F. Steigmeier, G.R. Booker, and G.K. Celler, *Microelectron. Eng.* 8, 163 (1988).

58. D. Venable and J.S. Krause, *Nucle. Instru. and Meth. Phys. Res.* B74, 65 (1993).

59. J.D. Lee, J.C. Park, D. Venables, S.J. Krause, and P. Roitman, *Materials Synthesis and Processing using Ion Beams*, Ed. R.J. Culbertson, O.W. Holland, S.J. Kevin, and K. Maes, 316, 757 (Pittsburgh, PA: Mater. Res. Soc.1994).

60. A. de Veirman, K. Yallup, J. Van Landuyt, H.E. Maes, and S. Amelickx, *Inst. Phys. Conf.* 87, 403 (1987).

61. J. Park, *PhD Dissertation*, Arizona State University, 1994.

62. J. Lee, *PhD Dissertation*, Arizona State University, 1994.

63. Y. Li, J. A. Kilner, R.J. Chater, A. Nejim, P.L.F. Hemment, C.D. Marsh, and G.R. Booker, *Nucle. Instru. and Meth. Phys. Res.* B85, 236 (1994).

64. G-H. Ma and S. Chevacharoenkul, *Mat. Res. Soc. Proc.* 199, 235 (1990).

65. D.E. Kendal, *Ann. Rev. Mat. Sc.* 9, 373 (1979).

66. L.F. Giles, A. Nejim, and P.L.F. Hemment, *Mat. Chem. Phys.*, 35, 129 (1993).

67. J.F. Ziegler, J.P. Biersack, and Littmark, *in The Stopping and Ranges of Ions in Solids* edited by J.F. Ziegler (Pergamon, New York, vol. 1, 1985).

68. M. Anc, J. Blake, and T. Nakai, *Electrochem. Soc. Proc.*, 99-3, 51 (1999).

69. Y. Li and J.A. Kilner, *Mat. Sci. and Eng.*, B12, 77 (1992).

70. D.M. Maher and B. Zhang, *J. Vac. Sci. and Technol.* B12, 347 (1994).

71. R. Kampman and R. Wagner, *Decomposition of Alloys, The Early Stages*, p.91 (Oxford, 1983).

72. C. Bonafos, B. Garrido. M. Lopez, A. Perez-Rodriguez, J.R. Morante, Y. Kihn, G. Ben Assayag, and A. Claverie, *Mat. Sci. Eng.* B69-70, 380 (2000).

73. J.C. Mikkelsenr, Jr., *Appl. Phys. Lett.* 45, 1187 (1984).

74. S. Bagchi, J.D. Lee, S.J. Krause, and P. Roitman, *J. Electron. Mater.* 25-1, 7 (1996).

75. T.Y. Tan and W.K. Tice, *Phil. Mag.* 30, 615 (1976).

76. P. Pirous, *Scripta Met.* 21, 1463 (1987).

77. A. Yoshino, M. Sugiyama, T. Morikawa, H. Tamegai, N. Nishio, T. Tashiro, and K. Okumura, *J. Appl. Phys.* 75 (8), 3892 (1994).

78. Y. Li, J.A. Kilner, R.J. Chater, P.L.F. Hemment, A. Nejim, A.K. Robinson, K.J. Reeson, C.D. Marsh, and G.R. Booker, *J. Electrochem. Soc.* 140, 1780 (1993).

79. S. Krause, M. Anc, and P. Roitman, *MRS Bulletin*, 23 (12), 25 (1998).

80. S. Visitserngtrakul, *PhD Dissertation*, Arizona State University, 1990.

81. Yet-Ming Chiang, Dunbar Birnie III, and David Kingery, *Physical Ceramics* p.397 (John Wiley & Sons, 1997).

82. Yan Tan, Benedict Johnson, Supapan Seraphin, and Maria J. Anc, *Proc. Electron Micros. Soc. America*, 6, 1086 (2000).

83. S. Bagchi, S.J. Krause, and P. Roitman, *Appl. Phys. Lett.* 71-15, 2136 (1997).

84. A. Ogura, *J. Electrochem. Soc.* 145-5, 1755 (1998).

85. R. Ghez and Y. J. Van der Meulen, *J. Electrochem. Soc.* 119, 1100 (1972).

86. M. Hamasaki, *Solid-State Electron.* 25, 479 (1982).